EXPERIMENTAL AND NUMERICAL TOOLS TO INVESTIGATE RINGING IN IC ENGINES

A DISSERTATION
SUBMITTED TO THE DEPARTMENT OF MECHANICAL
ENGINEERING
AND THE COMMITTEE ON GRADUATE STUDIES
OF STANFORD UNIVERSITY
IN PARTIAL FULFILLMENT OF THE REQUIREMENTS
FOR THE DEGREE OF
DOCTOR OF PHILOSOPHY

Julie Ann Blumreiter
March 2016

This dissertation is online at: http://purl.stanford.edu/ff148xg8169

I certify that I have read this dissertation and that, in my opinion, it is fully adequate in scope and quality as a dissertation for the degree of Doctor of Philosophy.

Chris Edwards, Primary Adviser

I certify that I have read this dissertation and that, in my opinion, it is fully adequate in scope and quality as a dissertation for the degree of Doctor of Philosophy.

Sanjiva Lele

I certify that I have read this dissertation and that, in my opinion, it is fully adequate in scope and quality as a dissertation for the degree of Doctor of Philosophy.

Reginald Mitchell

Approved for the Stanford University Committee on Graduate Studies.

Patricia J. Gumport, Vice Provost for Graduate Education

This signature page was generated electronically upon submission of this dissertation in electronic format. An original signed hard copy of the signature page is on file in University Archives.

Abstract

According to the International Energy Agency, mitigating greenhouse gas emissions to limit global temperature increase to 2°C will require efficient, combustion-based systems for light-duty transportation to take the place of conventional spark-ignited gasoline engines in the next 25 years. One of the barriers to high-efficiency combustion strategies such as homogeneous charge compression ignition (HCCI) is a phenomenon known as ringing, the formation of damaging pressure waves in the engine during the combustion process. Previous experimental results indicate that disruption of ringing is possible, to achieve high efficiency and high power density. Two tools to obtain spatially-resolved information during the ringing combustion process are the primary contributions described in this dissertation. A quasi-1D reacting compressible flow model captures the essential physics of the ringing phenomenon, to target experimental investigation and to interpret experimental results. To obtain spatially-resolved experimental data, an optically accessible engine capable of 250 bar peak pressure and Schlieren imaging was designed, manufactured, and demonstrated.

Acknowledgements

My name might be on the cover of this dissertation, but the contributions described here represent the combined effort and support of so many people, only a fraction of whom I have the space to acknowledge here. First, I have to thank Professor Chris Edwards for giving me the chance to study in his incredible research group. Thank you for always being available for me to pick your brilliant mind, and for having boundless enthusiasm for thermodynamics. Thank you for guiding me through a research project that is any mechanical engineer's wildest dream, and for believing in me even when (usually) I didn't believe in myself. It's been my privilege to be mentored by you.

The second group I have to thank are my colleagues in the Advanced Energy Systems Laboratory. Thank you to Matt Svrcek, J.R. Heberle, Sankaran Ramakrishnan, Paul Mobley, Adelaide Calbry-Muzyka, Rebecca Pass, Greg Roberts, BJ Johnson, Ben Kessel, Natt Oliver, Carol Regalbuto, John Fyffe, Mark Donohue, Burak Cetin, Chris Cameron, and Jacob Alvarez for being co-PhD-journeyers with me, with everything that entails. I could not have dreamed up a more enjoyable group of people to struggle alongside and learn from day in and day out. Thank you to my amazing summer students Juan Jimenez, Sean Duggan, and Brady "Han" Black for your hands-on help and also for reminding me how exciting my work is and how much I love teaching. An extra thank you to Mark Donohue for building the optical engine with me, and for always having a positive attitude and a smile. I'm so grateful for your friendship and I can say with certainty that I (and the engine) wouldn't have made it without you.

a chance and go to a prestigious college out of state, to my undergrad advisor Lester Su planting the seed in my mind that I could do a PhD (and telling me Stanford was the place!).

I have to thank my family - my parents Ann and Steve, my brother Mark, and all of my extended family for their love and support. You all taught me what it looks like to love God, serve others, and always put your best effort into the task at hand. I'm blessed to have never known a day that you weren't supportive and proud of me. To my godmother Barb Dresdow for always answering the phone when I called needing encouragement (and always making me laugh), to my brother for calling "just to nerd out" about engineering and physics. Thank you also to Phil Gray and my sister-in-law Jamie for adding so much joy to our family. I think I've said this before, but the highest compliment that I can get is when someone tells me "you remind me of your mom." Thank you mom for such an incredible example of character for me to aspire to.

The final and most important gratitude I have is to God, the giver of life and breath, the creator of all things. It has been a humbling journey, endeavoring to discover just a fraction more about the laws and processes at work in the created order.

x

Contents

List of Tables

List of Figures

xx

Chapter 1

Introduction

1.1 Why Energy?

Energy is considered one of the most important areas for scientists, engineers, and policy-makers to focus on. For example, everyone wants to know what the President's stance on energy policy will be. What will he/she do "about energy"? There are a myriad of reasons given for the importance of energy, including global climate change, national security, and energy access for development in emerging economies.

A very real concern on the global scale is energy poverty. In sub-Saharan Africa alone there are approximately 620 million people without electricity access, while 730 million people rely on solid biomass (such as wood or dung) for cooking. This not only impacts economic prospects, but carries significant implications for the health of this population. The particulate emissions from solid biomass cookstoves account for approximately 600,000 premature deaths each year in sub-Saharan Africa, according to the World Energy Outlook 2014 [1]. For comparison, AIDS-related deaths in that same region were only slightly higher, approximately 790,000, according to 2014 UNAIDS data [2]. These numbers reflect a segment of the global population that hasn't yet had access to the global energy supply—in other words—alleviating energy poverty necessitates an increase in global energy demand. Electric power demand in

sub-Saharan Africa is projected to quadruple by 2040 [1]. This, coupled with ever-increasing energy demand resulting from both economic development and population growth worldwide, poses a daunting challenge to meeting energy needs in the future.

At a very basic level, energy is essential for quality of life for people around the globe. Speaking realistically, our favorite energy resources such as oil are limited. Furthermore, as time goes on we continue to realize the negative impact their use poses on the environment and human health. The challenge then is to steward our energy resources and the environment in the best way we can, while continuing to provide for human needs such as transportation of people and goods, heat for cooking, and light for extending productive hours every day.

1.2   Why   Transportation   and   Internal Combustion Engines?

A portion of this goal of stewarding energy resources and the environment can be met with deployment of renewable resources for electricity generation such as wind, solar, and hydro-electric power. However, the big contributors to meeting human needs at present are still fossil-fuel-derived systems for transportation, electricity generation, and industrial processes. Currently, about 95% of transportation energy worldwide is derived from fossil fuels [3]. The transportation sector already leads in end-use-sector CO_2 emissions, accounting for approximately 20% of global energy- and process-related CO_2 [3]. Furthermore, in 2012 there were 75 million new light-duty vehicles added to the world's roads [4]. The rapid rate of industrialization in developing countries, and the increase in number of cars and drivers on the globe, means that any efficiency improvement in these systems that can be attained in the near term has the potential for a significant impact.

The transportation sector stands out in the boxed portion of Figure 1.1 since its

---

[1] IEA graphic from the Energy Technology Perspectives © OECD/IEA 2015, IEA Publishing. Licence: $http://www.iea.org/t\&c/termsandconditions/$ [4]
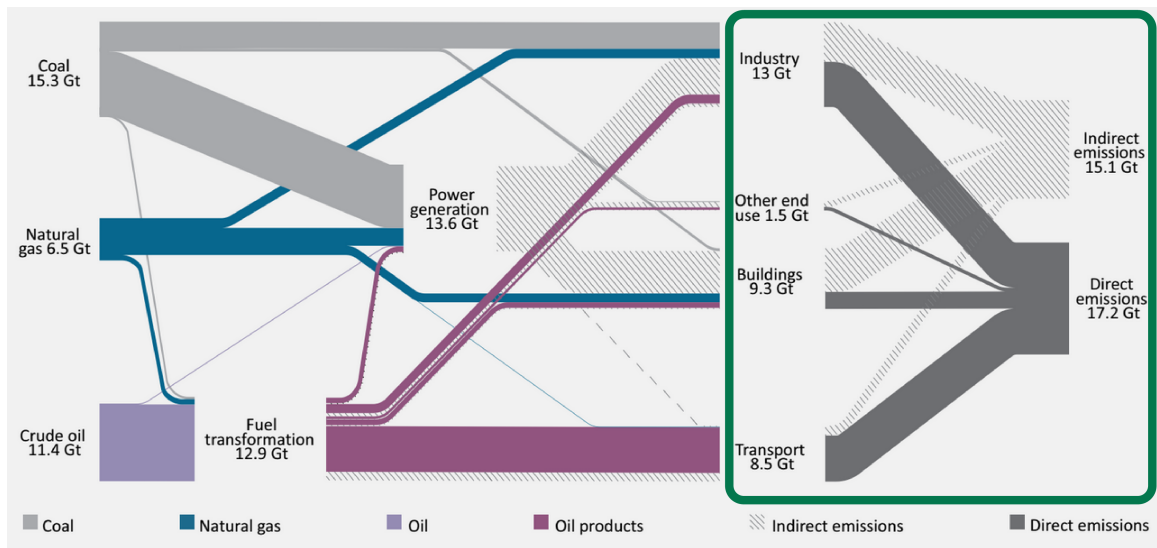
Figure 1.1: Global direct and indirect CO_2 emissions sorted by fossil fuel source and end-use sectors.[1]

CO_2 emissions are primarily classified as direct emissions rather than indirect emissions. Direct emissions are classified as those arising from end-use while indirect emissions are classified as those arising from energy transfers or transformations upstream of end-use. The emissions from transportation systems primarily occur at the point of the moving vehicle. Emissions attributed to buildings and industry, on the other hand, consist in large part of indirect CO_2 emissions. An example of this is the electricity generated to keep lights on in a building. Emissions associated with this energy usage are released into the atmosphere at the power plant location and not at the light bulb itself. The direct nature of CO_2 emissions from transportation carries interesting implications for development of new technology and deployment of that technology into the marketplace. Consumer decision making has a greater influence on transportation emissions (especially for light-duty passenger vehicle emissions) while local, state, and federal governments have a greater influence on things like electricity generation. While fuel economy standards like the CAFE standards have pushed

automakers to offer more fuel-efficient vehicles to customers, and some electricity consumers have opted to pay for renewable electricity, in general the average consumer has much more influence on vehicle choice than electricity source.

Capturing emissions and increasing efficiency on a moving vehicle, where space and weight constraints are very stringent, poses additional challenges compared to a stationary power plant. Part of the solution to that challenge could be to deploy technology to shift the breakdown of emissions from direct to indirect for vehicles – electric vehicles being a prime example of this type of shift. This concept of a "zero-emission vehicle" refers to a vehicle which produces no direct emissions, but its use still causes indirect emissions at the point where the electricity was produced. Electric vehicles for light-duty transportation are a very promising development, but they are not yet being adopted in the fastest-growing markets due to their cost. In only four countries do electric vehicle sales account for more than 1% of annual new vehicle sales [4]. Furthermore, in many rapidly expanding markets, the electrical grid is often primarily fueled by coal, which would result in electric vehicles inflicting more harm to the environment and local air quality than liquid hydrocarbon-fueled vehicles. Another solution to the emissions problem, besides shifting emissions from the vehicle to the power plant, is to increase the efficiency of the processes in transportation that lead to direct emissions.

Light-duty piston engines for passenger transportation are some of the least efficient engines, since they are constrained by both size and cost. They accounted for 42.7 percent of U.S. greenhouse gas emissions from transportation in 2013, approximately twice as much as the next biggest transportation category (freight trucks) [3]. There is a practical tradeoff between imposing strict emissions and efficiency regulations to spare the air and public health, and the potential to stifle economic growth, especially in developing countries, with such regulations. Providing efficiency improvements that are effective and achievable in the short term can inspire compliance with stricter emissions regulations while allowing for economic growth and empowerment for populations in developing nations.

The International Energy Agency's 2015 Energy Technology Perspectives report details the most likely technology and policy pathways to limit global temperature increase to 2 degrees Celsius above pre-industrialization levels. In their so-called 2DS scenario, half of the CO_2 reduction coming from the transportation sector is from energy efficiency, while another 20% comes from switching to hydrocarbon fuels of lower carbon intensity [4].
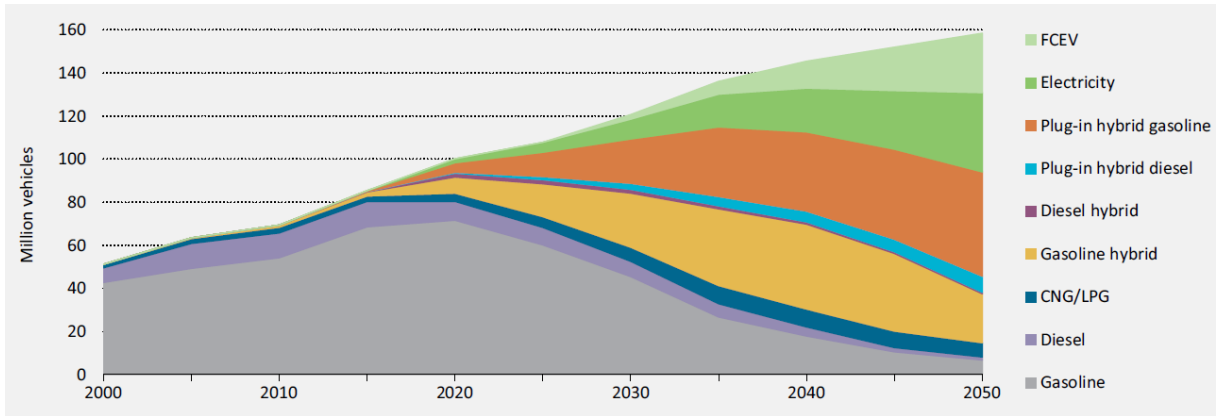
Figure 1.2: Projected global passenger light duty vehicle portfolio for 2DS [4].

In Figure 1.2 the International Energy Agency's projected passenger light duty vehicle global breakdown for the 2DS can be seen. It should be noted that the 2DS is considered very ambitious and optimistic, representing a realistic but best-case scenario for curbing global emissions. In the projection we see a shift away from purely gasoline-powered passenger vehicles toward a mix of other more efficient technologies. Note that the majority of the breakdown even in 2050 still relies on hydrocarbon fuels and combustion in piston engines – in the form of hybrid and plug-in hybrid vehicles. In the figure, all of the wedges except for the two at the top of the graph (FCEV - fuel cell electric vehicle and Electricity) represent combustion-engine-based transportation modes. As such, light-duty passenger transportation will continue to rely on combustion-driven systems in the near future. There are still significant efficiency gains that can be made, as current combustion engines fall far short of extracting the full work potential of the fuel resource. This means that it

is critical to continue researching, and bringing to market, technologies that more
effectively convert hydrocarbon fuel resources into useful work for transportation.

1.3   Motivation for Current Research

The topic of this dissertation is a detailed look at one of the major barriers to
increasing the efficiency and power density of light-duty passenger vehicle engines:
the problem of strong pressure waves forming when these engines operate at their
most efficient and power-dense operating points. The pressure waves formed during
the combustion process cause damage to the engine, making these operating points
impractical to implement. However, promising previous research has indicated that
an effective mitigation strategy for these pressure waves may exist [5].

Svrcek et al. used an extreme compression free-piston engine to autoignite
premixed, non-dilute methane and air at 60:1 compression ratio to achieve very
high engine efficiency [5]. The engine conditions in this experiment would be
expected to produce some of the most violent and damaging pressure waves, but
Svrcek wasn't concerned with pressure waves – just overall efficiency of the engine.
To operate at such a high compression ratio, it is necessary to find a way to delay
the combustion so that it doesn't occur during the compression stroke, but instead
occurs at the point of minimum volume (which yields the highest efficiency). He
used two different methods to delay the combustion until the point of minimum
volume during the experiment. The first method is charge cooling: The charge is
uniformly cooled prior to compression such that the combustion takes place at the
minimum volume. The second method he explored is water injection. Water
injection plays a dual role in affecting the combustion timing: The evaporating
water is effective at charge cooling, and the additional mass serves to moderate the
combustion process. The water injection also had the unforeseen benefit of
smoothing the pressure trace and eliminating pressure waves that are seen in the
charge cooled case. The contrast between the two cases, shown in Figure 1.3, is
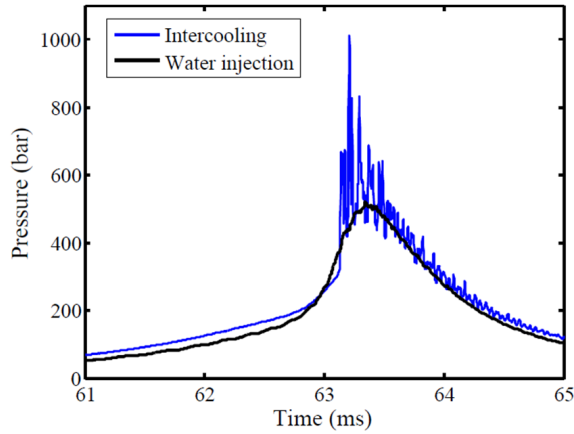
Figure 1.3: Two pressure traces from an extreme compression free-piston engine.[2]

striking.

These data suggest that it is possible to overcome the problem of pressure waves in engines, given that stoichiometric methane and air have been successfully autoignited without pressure waves, by introducing only a small amount of water (8% by mass). Clearly, certain methods of mixture preparation can create just the right conditions leading to well-behaved smooth combustion at full load. There is much still to understand about the combustion process in the water-injected case to determine what makes it so different from the charge-cooled case. Understanding this difference would require more information about how the combustion process evolved than can be gleaned from the pressure transducer data plotted above. The path to implementing this mitigation strategy takes us through the process of understanding these waves in detail: how they form and how to potentially disrupt them.

A combination of both modeling and experimental tools to probe this phenomenon have been developed and are the primary contributions described in this dissertation. A spatially-resolved combustion simulation was developed to understand and explore the effect of various mixture preparation methods on the

---

[2]Data re-plotted with permission from Svrcek and Edwards [5]

combustion process. Additionally, a high-pressure optical access engine was designed and constructed to allow this type of combustion event to be studied using high-speed video. Beyond the specific problem of pressure waves, the experimental tools described in this dissertation hold significant potential for future investigation of advanced combustion strategies. The ability to bring optical diagnostics to a high-pressure engine environment holds promise for previously-impossible optical studies of Diesel combustion, direct injection combustion of oxygenated fuels, and other promising advanced combustion strategies.

The improvement of fuel economy standards and emissions regulations will continue to further development of cleaner and more efficient engines for the world's transportation systems. Additionally, concepts such as HCCI (Homogeneous Charge Compression Ignition) are even more suited to enter the marketplace due to the recent adoption of hybrid-electric vehicles. Hybrid vehicles accounted for 1.3 million new vehicle sales in 2012 (52% of that from Japan and 39% in the U.S) [1]. A hybrid vehicle has the ability to store extra power produced by the engine in small batteries (smaller than in a fully electric vehicle or plug-in hybrid vehicle) to be discharged later, when the driver demands more power than the engine is producing. This allows the engine to operate in an overall narrower range while the vehicle as a whole still performs over the full load range. This enables engines to be more finely optimized for efficiency once the requirement of an extended operating range is lifted. This advantage of hybrid-electric vehicles sets the stage for advanced combustion strategies to move into commercially-available vehicles.

Using the 2DS as a road-map toward curbing emissions while meeting the world's energy needs and stewarding the environment, it is clear that the near future of transportation lies in high-efficiency hydrocarbon-based systems. Even small efficiency gains that can be incorporated now will have a significant and lasting impact considering the lifetime of the vehicle and the sheer number of vehicles being added to the world's roads every year. Nobody said it was going to be easy, but

"I would hope that getting a PhD in anything would be difficult."
-Bernard H. Johnson, *Post-swimming interview*

Amen.

Chapter 2

Background of Pressure Waves in Engines

This chapter describes one of the key barriers to high load premixed charge combustion in piston engines. First, there will be a background of piston engines followed by discussion of current limitations of promising combustion strategies such as homogeneous charge compression ignition (HCCI). There will follow a description of the problem of pressure waves in high-load premixed combustion, and a framing of that problem in the larger context of reacting wave propagation.

This chapter will then describe how the understanding of pressure waves in engines has evolved over time and the current relevant theory and modeling efforts. Finally, it will describe previous experimental results that reveal there are still practical questions to be answered. Developing the numerical and experimental tools to answer those practical questions is the main focus of this thesis.

2.1   Piston Engines Background

Piston engines at their core are intended to convert the chemical bond energy of a fuel into work, in the form of a turning shaft (or a vehicle and passengers moving down

11
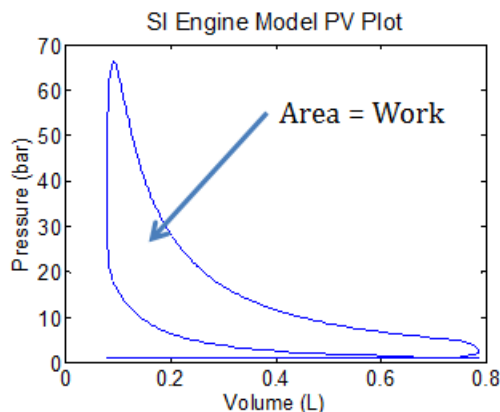
Figure 2.1:   Pressure-Volume plot demonstrating engine cycle; compression, combustion, expansion. The area of the loop is the net work.

the road). This is accomplished by combining the fuel with air from the environment, at a state of elevated internal energy (typically accomplished by compressing the air and fuel), and expanding the combustion products in a cylinder to extract work [6, 7]. This process can be seen on a pressure-volume plot in Figure 2.1. The plot was produced using a crank-angle-resolved, zero-dimensional engine model code. The area enclosed by the loop is the work produced by the cycle as computed by:

$$W = \int P dV \qquad (2.1)$$

Piston engines used in transportation applications, unlike power plants, must be able to operate under a transient load demand imposed by the driver of a vehicle. The range of operating points traversed by an engine can most easily be visualized by creating a speed-load plot, or *engine map*. A sample engine map can be seen on the left side of Figure 2.2. The load, in units of work divided by the swept volume of the engine (often called MEP[1]), is on the y-axis while the engine speed in revolutions per minute is on the x-axis. In the figure, contours of BSFC

---

[1]MEP stands for mean effective pressure and has units of work per displacement volume. Load is reported by dividing the work output by the swept volume of the engine cylinder to make it easier to compare engines of differing size.
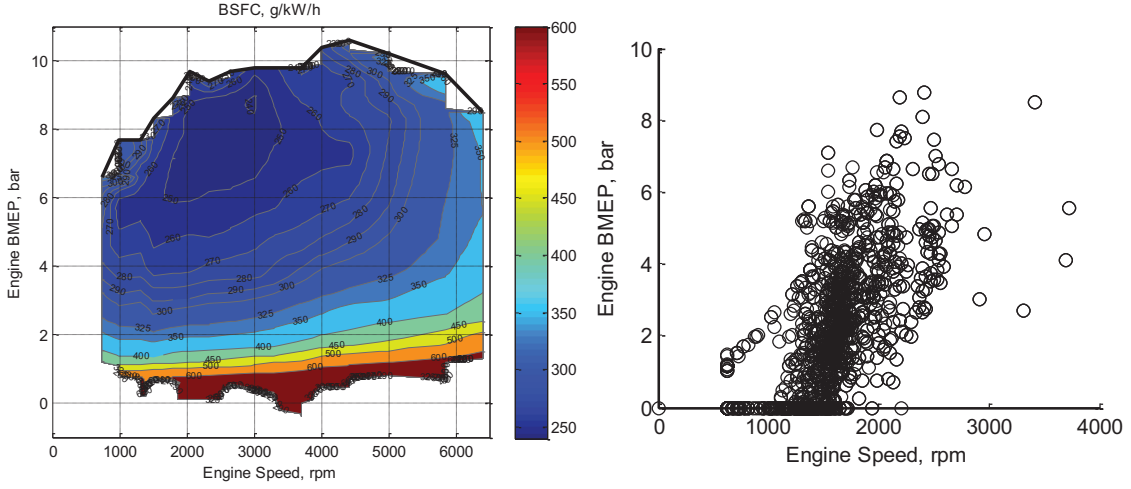
Figure 2.2: (Left) Speed-Load map of a typical SI engine. Contours of BSFC[2] are shown. On the y-axis, break mean effective pressure (BMEP) refers to actual engine work out, after friction and other losses are accounted for. (Right) Representative engine speed/load points for the EPA drive cycle. Graphics adapted from [8].

(brake-specific fuel consumption) are plotted, a measure of fuel consumption per work produced. The BSFC can be thought of as an inverse efficiency number. On the right side of Figure 2.2 a sample driving cycle, the EPA Federal Test Procedure drive cycle, is presented. These points represent a set of typical operating points for an engine, intended to simulate driving a vehicle around a city, and is one of several driving cycles that are used to calculate fuel economy and emissions for passenger vehicles. The range of points from the drive cycle represents the minimum dynamic range over which a vehicle must be capable of operating.

It is worth noting that hybrid vehicles enable engine performance with a significantly smaller operating range on the speed-load map to still meet the load demanded by the driver. This de-coupling of driver-demand from engine-supply may enable high-efficiency engine concepts that limited load range to be implemented. High-load capability and high power density are still desirable,

---

[2]BSFC stands for brake-specific fuel consumption and can be thought of as an inverse efficiency metric.
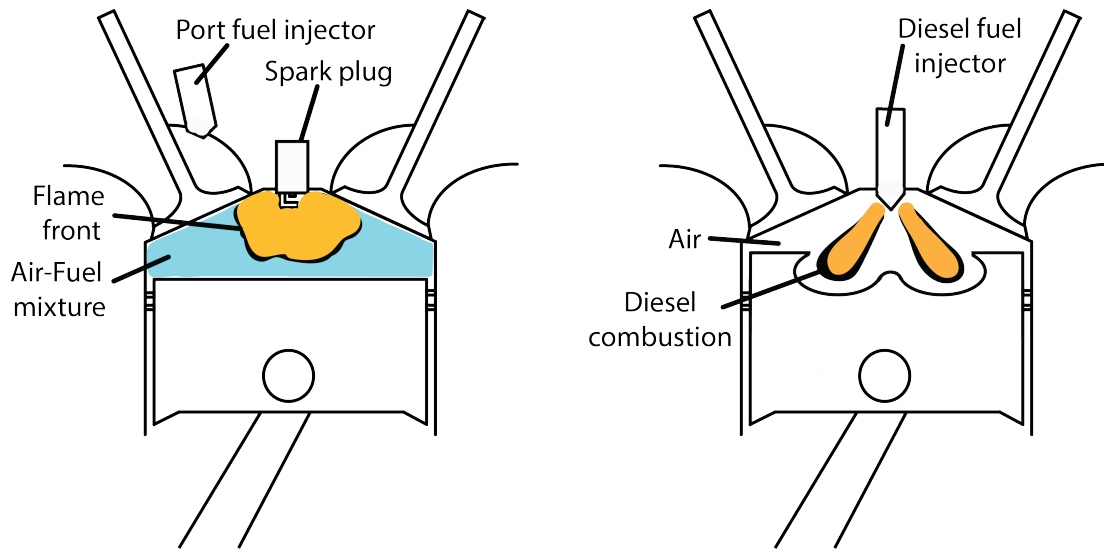
Figure 2.3: Schematics of SI Gasoline and CI Diesel engine combustion.

however, since these points are often most efficient and can reduce overall size, weight, and cost of the engine.

2.1.1   Types of Piston Engines

Almost all piston engines fall into one of two categories: spark-ignited (SI) or compression-ignited (CI), depicted in Figure 2.3. Spark-ignited engines typically operate on fuels such as gasoline (a blend of C4 - C12 hydrocarbon molecules, averaging approximately C_7H_{14} by molar mass) or ethanol (C_2H_5OH), or a blend of the two. In an SI engine, air and vaporized fuel are mixed together before compression, and a spark is used to ignite the mixture near the point of minimum volume, termed top-dead-center (TDC). Spark-ignited engines typically have a geometric compression ratio of between 9:1 and 11:1. These engines are limited in compression ratio by the propensity of the fuel-air mixture to autoignite prior to complete burning of the mixture by the flame front.

Compression-ignition engines typically operate on more ignitable fuels consisting of longer hydrocarbon chains than SI engines, such as Number 2 Diesel

fuel ($C_{12}H_{23}$ on average). During CI engine operation, air is compressed through a typical compression ratio of 16-18 and a high-pressure injection of fuel takes place near TDC [6]. The air is sufficiently hot and the fuel sufficiently ignitable that combustion begins to take place when air and fuel mix, resulting in burning plumes of fuel emanating from the fuel injector. Fuel-rich and fuel-lean regions in this type of combustion lead to the formation of soot and oxides of nitrogen (NO_x), and impose a typical limit of fuel-air-equivalence ratio of 0.7 (that is, only 70% of the fuel which could be injected to have neither excess air nor excess fuel). This requirement for excess air represents a loss of power density, since that 30% of air is compressed and expanded without participating in the chemical reaction. Conversely, many spark-ignited engines operate at a stoichiometric equivalence ratio, having neither excess air nor excess fuel.

A major advantage of operating at a stoichiometric equivalence ratio is the simple and affordable exhaust aftertreatment afforded by the use of a three-way catalyst to prevent atmospheric emissions of NO_x, CO, and unburned hydrocarbons. A three-way catalyst is able to both oxidize the CO and unburned hydrocarbons and reduce the NO_x only when the exhaust is composed of products at stoichiometric proportions. Engines operated under lean conditions (with excess air) must either seek to avoid high temperatures to avoid forming NO_x, or have a lean NO_x trap, or SCR system (selective catalytic reduction). Many engines also employ exhaust gas recirculation (EGR), in which exhaust gas is re-introduced into the combustion chamber to serve as a temperature moderator to help avoid NO_x emissions.

2.2 Premixed, Autoignited Combustion / HCCI

The goal of this area of research is to determine a combustion strategy that is both efficient and suitable for engine operation over a sufficiently wide load range to be commercially viable either in a hybrid or non-hybrid architecture. Special emphasis is placed on enabling high-load operation to achieve efficiency and power density. A

premixed approach is considered in this work, rather than pursuing traditional CI combustion, because of the challenges associated with soot formation and a desire to operate the engine at a stoichiometric equivalence ratio.

2.2.1   What is HCCI Combustion?

Homogeneous Charge Compression Ignition, or HCCI, is a combustion strategy that attempts to capture the best aspects of both SI and CI engines. Air and fuel are premixed, as in gasoline engines, but rather than being ignited by a spark, the mixture is compressed further such that the mixture autoignites. In order to achieve sufficiently high temperatures to autoignite the mixture and to moderate the reactions, exhaust gas is either reintroduced or trapped from the previous engine cycle using negative valve overlap (NVO), and mixed with the fresh air and fuel in the following cycle. HCCI engines typically operate at a higher compression ratio than SI engines because of the elevated thermodynamic state required to autoignite the air-fuel-exhaust-gas mixture (as compared to SI combustion where this autoignition is undesirable). In piston engines, a higher compression ratio ideally corresponds to higher efficiency, in the absence of heat transfer effects.

During the HCCI combustion process the chemical reactions occur throughout the cylinder simultaneously, as illustrated in Figure 2.4. This autoignited combustion process occurs more rapidly than SI flame propagation or CI fuel plume mixing, affording HCCI advantages in terms of work extraction (increasing the area of the work loop on a P-V diagram).

The progress of autoignition during HCCI combustion is determined by the chemical kinetics of the combustion reactions. There are no actuators to directly control when the combustion process begins or what its duration is, the way a spark and flame speed does in an SI engine, and the way fuel injection does in a CI engine. The chemical-kinetic rates which determine combustion timing in an HCCI engine are a function of many different variables, such as local mixture temperature as well as air and fuel concentration.
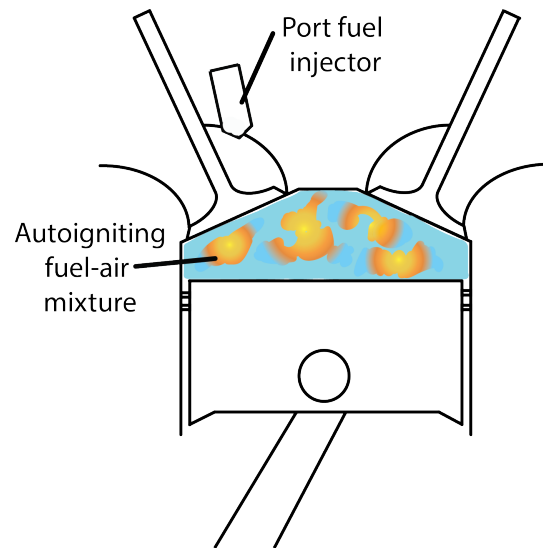
Figure 2.4: HCCI combustion occurs throughout the cylinder based on chemical kinetics. This is in contrast to flame propagation in an SI engine or fuel injection in a Diesel engine.

Thus, initial mixture preparation is extremely important for determining the timing and duration of HCCI combustion. In other words, this type of combustion is very sensitive to initial conditions. Due largely to the stochastic nature of turbulence, the control inputs do not automatically determine the combustion behavior in a completely deterministic manner—rather it's a statistical outcome. This provides an inherent challenge in controlling the combustion process. As will be discussed in the coming sections, operating an engine at high-load, efficient, autoignited operating points tends to increase the likelihood of damaging combustion events such as strong pressure waves in the engine. Despite this tendancy toward engine damage, there are numerous benefits of HCCI combustion that make it attractive.

2.2.2 Benefits of HCCI Combustion

HCCI derives efficiency improvement over conventional SI combustion through dethrottling, a higher compression ratio, lower heat transfer losses, and a more
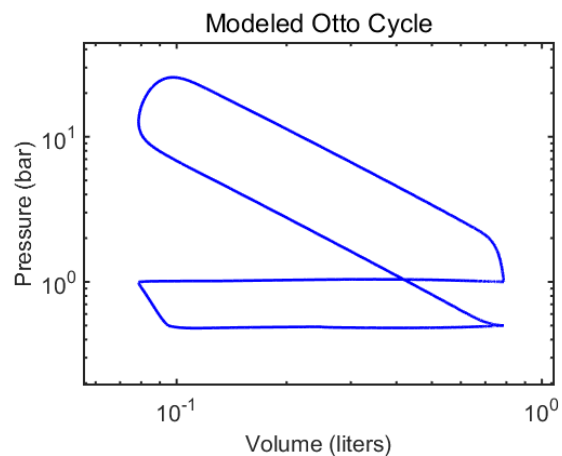
Figure 2.5: Log(P)-Log(V) plot depicting the work loop (upper) and pumping loop (lower).

rapid combustion process. Furthermore, HCCI engines tend to derive emissions benefits over SI engines resulting from lower-temperature combustion.

The typical way to vary load in SI engines is by throttling, or lowering the pressure in the intake manifold by creating a restriction to the flow. By reducing the amount of air that enters the chamber, less fuel can be added while maintaining the desired equivalence ratio, which for many SI engines is stoichiometric (neither excess air nor excess fuel). Varying the load in this way requires the engine to expend work to draw air from the low pressure intake manifold through the intake valve, resulting in lower efficiency. This can be visualized by the lower loop on a P-V plot, termed the "pumping loop" and this work loss is termed "pumping loss." Figure 2.5 depicts a log(P) vs. log(V) plot (which makes the pumping loop easier to see) of a modeled, motored cycle having an intake manifold pressure of 0.5 bar. The area enclosed by this loop is subtracted from the area of the upper work loop to determine the net work. In an HCCI engine, on the other hand, load is varied by either retaining, reinducting, or recirculating an increased amount of exhaust gas from the previous engine cycle. The exhaust gas displaces air in the cylinder, allowing the engine to take in less air without throttling and thus without generating a larger area in the

Effect of Burn Duration in SI Model
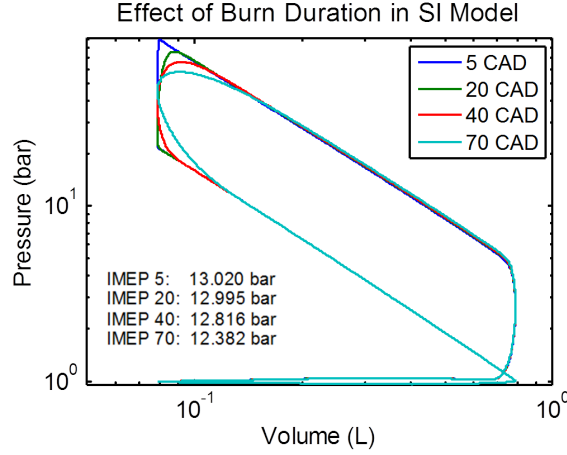
Figure 2.6: Log(P)-Log(V) plot demonstrating effect of burn duration on indicated MEP.

pumping loop. The result is a higher net work output.

HCCI further derives benefits over SI by having reduced heat transfer losses. Heat transfer losses are one of the largest sources of inefficiency in modern piston engines [9]. HCCI engines have a lower peak temperature than SI engines because of dilution with exhaust gas, and thus have lower heat transfer losses through the whole cycle.[3] The low-peak-temperature and premixed-nature of HCCI combustion further contribute to a combustion strategy that produces almost no soot, and very low NO_x emissions compared with SI combustion. Soot and gaseous emissions are so low, in fact, that engine-out levels for many engine operating points meet emissions requirements, even in the absence of an exhaust aftertreatment system.

A final efficiency benefit that HCCI combustion derives over SI is a more rapid combustion process. A primary focus of this thesis is on the details of a rapid combustion process. The work loop on a P-V plot is larger when combustion is rapid and well-phased (slightly after TDC). Figure 2.6 demonstrates the concept using a simple SI two-zone, zero-dimensional model. The combustion duration, as imposed

---

[3]Even though the pre-ignition temperature is higher in HCCI engines, the majority of heat transfer occurs around TDC, where SI temperatures exceed HCCI temperatures, resulting in a net higher cycle heat transfer loss for SI engines.
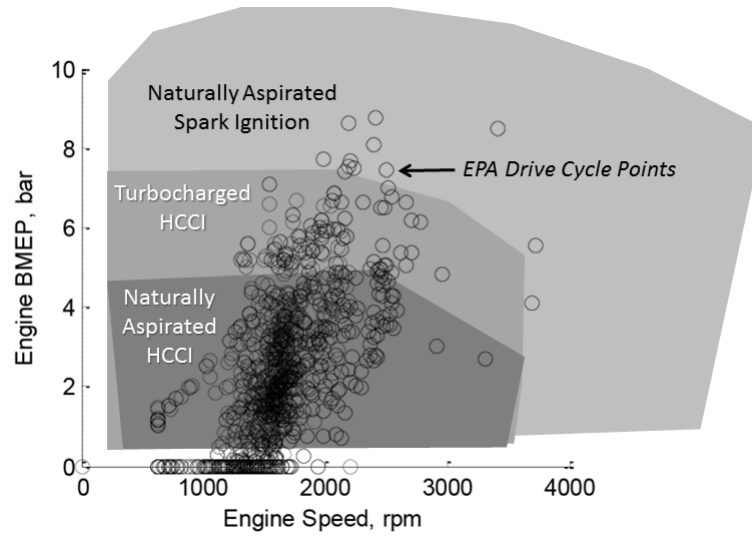
Figure 2.7: Speed-load map of premixed engine operation depicting the operating range of naturally aspirated spark ignited engines, turbocharged HCCI engines, and naturally aspirated HCCI engines, as well as EPA drive cycle points [8].

by a Wiebe function in the model, is different in each case, ranging from 70 crank angle degrees down to five crank angle degrees. All else being equal, (amounts of air and fuel, compression ratio, heat transfer) the more rapid the combustion process the greater the work out of the engine.

2.2.3   Challenges of HCCI Combustion

The primary drawback of HCCI is its limited operating range, which for a naturally-aspirated engine peaks near 5 bar IMEP [10, 11, 12]. The typically dilute nature of HCCI inherently limits the load range available, as a portion of the cylinder volume contains exhaust gas which has been trapped, re-breathed, or recirculated. Figure 2.7 depicts the relative operating ranges of three combustion strategies: naturally aspirated HCCI, turbocharged HCCI, and naturally aspirated SI. Superimposed is the EPA drive cycle previously seen in Figure 2.2. Turbocharging is an excellent way to improve both power density and efficiency of

an engine. The use of turbocharging can extend the upper boundary of HCCI, but there remain points in the driving cycle that are inaccessible. Ideally, turbocharging would be reserved for enhancing the load range of a combustion strategy beyond what can be accomplished in a naturally aspirated engine, rather than compensating for low power density.

Mode-switching is a way to allow for functional engine combustion over the entire drive cycle region while deriving benefits from HCCI when possible [13]. Under a mode-switch strategy, the engine operates in HCCI mode within the HCCI range on a speed-load plot, and a switch to SI combustion is made to operate the engine outside of that range. The switch itself is a sharp transition that must be made transparent to the driver, making this load variation strategy challenging from both a combustion and controls perspective. For these reasons it is still desirable to span the full load range with just a single combustion strategy. Extending the high load capability of an efficient combustion strategy, such as HCCI, would obviate the need for a mode-switch and could simplify the adoption of HCCI as a viable commercial combustion strategy even outside of hybrid vehicle architectures.[4]

2.2.4 High Load Limit of HCCI Combustion

The high-load boundary for acceptable HCCI engine operation is often defined using peak in-cylinder pressure and maximum pressure rise rate (often abbreviated MPRR). Typical limiting values for these quantities are approximately 100 bar, and approximately 5-10 bar/CAD,[5] respectively. These limits are in place to avoid two undesirable outcomes: excessive engine noise and engine damage. Engine noise is a less restrictive limitation since it can be somewhat mitigated apart from the combustion process, but engine damage must be avoided. A more important but

---

[4]Integrating advanced combustion concepts such as HCCI in a hybrid vehicle architecture has the potential to somewhat alleviate the load range requirement, though for emerging economies the added complexity of a hybrid vehicle might prove economically prohibitive.

[5]CAD refers to the crank angle degree of the crank shaft during the engine cycle. In a two-stroke engine, each engine cycle has a duration of 720 crank angle degrees

perhaps less quantifiable high-load limit for HCCI is imposed by *ringing:* the formation of damaging pressure waves in the engine.

Figure 2.8: Damaged piston from thermal pitting [14].

The pressure waves formed by ringing inflict engine damage by interacting with the thermal boundary layers on the cylinder walls and piston face, rapidly sweeping hot gases against the metal surfaces and effectively scrubbing off the protective gaseous thermal boundary layer. This boundary layer disruption causes much higher heat transfer rates than is typical, and can quickly erode material from the metal surfaces [15]. An example of a damaged piston is seen in Figure 2.8. This mode of engine damage is the same type that results from knock in SI engines, and can cause significant damage in a relatively short amount of time. For this reason, ringing pressure waves must be mitigated, or the operating points which produce them avoided, in production engines.

Besides engine damage, Noise, Vibration, and Harshness (NVH) requirements impose limitations on engine operation. While a high MPRR is not damaging in the same way that ringing can be, it is responsible for undesirable engine noise as well as potential structural damage to piston rings if the engine was not designed for such a high pressure. Audible noise can result from the combustion process when the in-cylinder pressure causes excitation in the engine block in the range of audible frequency [16]. Andreae et al. concluded that peak rate of pressure rise

correlated with audible engine noise, while pressure oscillations in the engine did not contribute to audible noise [17]. They determined a pressure rise rate threshold of 50 bar/ms above which audible engine noise could be detected. This would translate to approximately 5 bar/CAD (a typical rule-of-thumb pressure rise rate limit) at 1600 RPM.

An additional limitation on the HCCI operating range is imposed by the coefficient of variation—a measure of the cyclic variability among a set of engine cycles at a certain operating point. Too high a value of cyclic variability can result in some cycles that are excessively strong and some cycles that misfire. Since each HCCI cycle depends on the exhaust of a previous cycle, a misfire has the potential to stop the engine from combusting altogether.

2.2.5   Current Load Extension Strategies for HCCI

Current strategies to mitigate ringing are often focused on reducing the pressure rise rate (by reducing the overall reaction rate), or by uniformly diluting the air-fuel mixture. These include the use of cooled EGR, increased thermal stratification, and delayed combustion phasing [10, 18]. Cooled EGR can effectively prevent early combustion phasing as well as moderate the overall rate of the combustion process [19]. However, increasing charge dilution, even with cooled exhaust gas, reduces the maximum load at which the engine can operate. To state it another way, engines are usually sized according to the power requirement of the intended application. Any increase in dilution for a combustion strategy necessitates using a physically larger engine to produce the same amount of work as an engine running a non-dilute combustion strategy.

Thermal stratification to slow the rate of combustion can be achieved by using a lower coolant temperature or with delayed combustion phasing (giving more time for wall heat transfer to produce thermal stratification prior to the combustion event) [20]. Low coolant temperatures, however, increase heat transfer—one of the largest sources of inefficiency in engines [21, 9]. Late combustion phasing, either for the
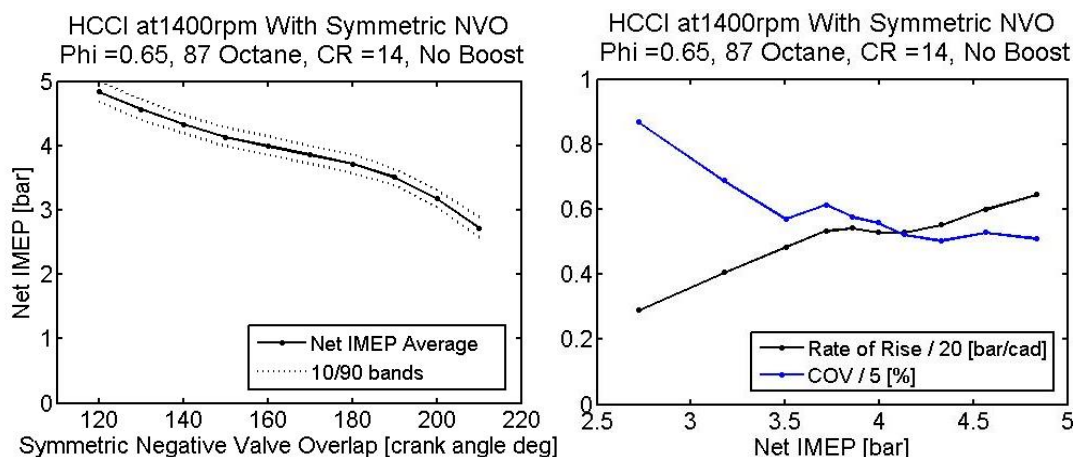
Figure 2.9: (Left) HCCI load variation as a function of negative valve overlap. (Right) Max pressure rise rate and coefficient of variation of IMEP as a function of load.

purpose of increased thermal stratification or to mitigate ringing, fundamentally derates engine performance by changing the shape of the pressure-volume loop to one with a smaller area, resulting in less work. In pursuit of efficient high-load operation, increasing loss mechanisms such as heat transfer or reducing work extraction by delayed combustion phasing, are not ideal ways to improve performance. While these methods can be successful in increasing the load range, they counteract some of the efficiency benefits that make HCCI an attractive strategy.

A high rate of pressure rise, which is typically targeted as something to avoid in piston engines by using one of the aforementioned strategies, is actually one of the benefits of HCCI over SI. As was discussed previously and shown in Figure 2.6, with all other factors being equal, the more rapid the combustion process, and thus the higher the pressure rise rate, the greater the work out of the engine. Many autoignited low-temperature combustion (LTC) strategies seek to slow the combustion process down, thereby limiting performance [10].

2.2.6   Basic HCCI Engine Data

A single-cylinder research engine was used to map basic HCCI data points. The plot
on the left in Figure 2.9 demonstrates that as the engine's valve timing is varied to
trap more exhaust gas, the load (IMEP) is decreased. Negative valve overlap (NVO)
refers to the number of engine crank angle degrees that elapse between exhaust valve
closing and intake valve opening. A typical spark-ignited engine will have a small
amount of positive valve overlap, since it is usually desirable to clear out all of the
exhaust gas. The strategy for HCCI combustion is to trap exhaust gas and bring
in less air to achieve lower engine operating loads, thus higher amounts of NVO are
used for lower loads.

The plot on the right in Figure 2.9 reveals how the maximum pressure rise rate
and coefficient of variation of IMEP change as a function of increasing engine load.
These are two important quantities which, as discussed previously, limit the load
range and affect implementation of HCCI combustion in production vehicles. It is
often seen as desirable to maintain a pressure rise rate below a certain threshold and
it is necessary that combustion be robust enough to continue—too high a coefficient
of variation at a certain operating point can be a sign of potential misfire. In the
case of HCCI, misfire can lead to complete loss of combustion, as each cycle depends
on exhaust from the previous to continue.
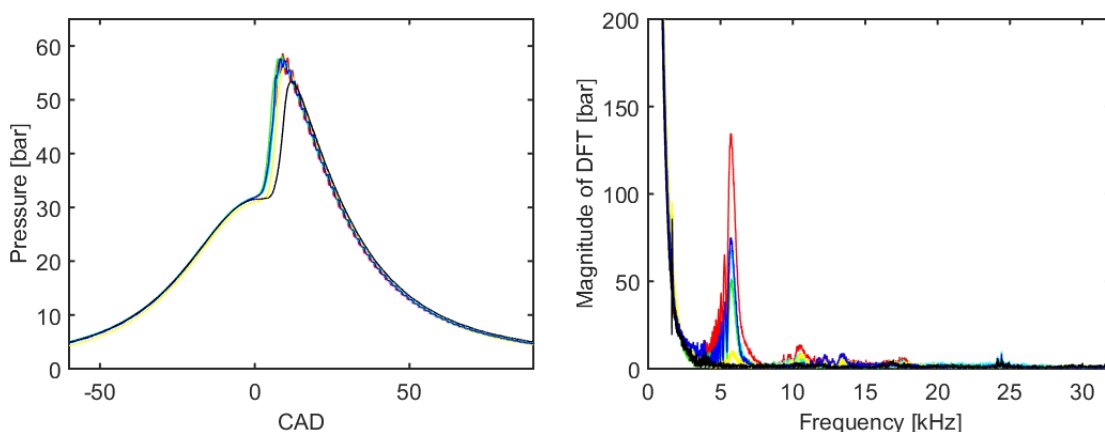
Figure 2.10: (Left) Plot demonstrating six different HCCI combustion cycles in a single cylinder research engine. (Right) Plot of single-sided amplitude of frequency spectrum of the same six pressure traces taken in a single-cylinder research engine.

At the high-load limit, ringing pressure traces like the ones on the left of Figure 2.10 exhibit high peak pressure, a steep pressure rise rate, and rapid pressure oscillations right around TDC. Pressure data from the engine can be analyzed for frequency content using a Fourier transform. On the right of Figure 2.10 the discrete Fourier transform of the pressure signal from Figure 2.10 can be seen. The frequency spectrum shows peaks in frequency content centered at the natural acoustic modes of the cylinder. These can be estimated by calculating the natural modes of oscillation of a gas contained in a cylindrical volume with rigid walls. For an 80 mm bore the first mode has a frequency of approximately 5 kHz, as can be seen in the figure. The cycle plotted in red has the most visible oscillations in the pressure trace, and the highest magnitude of frequency around 5 kHz. The cycle plotted in black has the smoothest pressure trace and has a low DFT magnitude around 5 kHz.
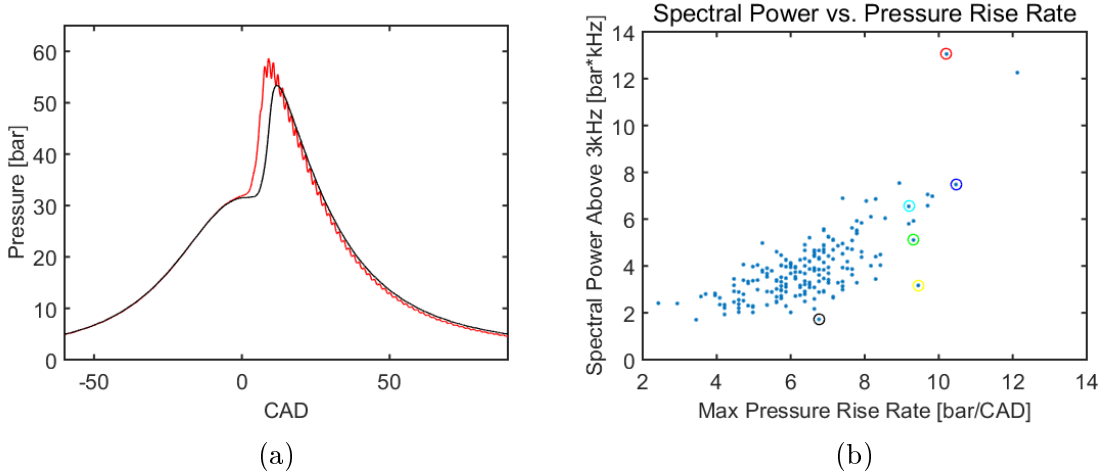
Figure 2.11: (Left) Comparison of ringing pressure trace and non-ringing pressure trace. (Right) A scatter plot showing 200 cycles from the single-cylinder engine.

2.2.7 Ringing vs. Pressure Rise Rate

The reason that pressure rise rate is usually targeted as something to be limited in HCCI engines is that it is difficult to differentiate it from ringing. In fact, the two phenomena are quite distinct, though they are very often correlated. The maximum pressure rise rate is a function of the overall rate of exothermicity of the combustion reactions in the engine cylinder, combined with the effects of the piston motion. Ringing occurs when the spatial and temporal evolution of autoignited combustion proceed in such a way as to produce pressure waves that reverberate in the engine. These pressure waves appear as high-frequency oscillations on an in-cylinder pressure trace (as shown in Figure 2.11(a)), and are often accompanied by high peak pressures.

High pressure rise rates have been observed to occur with pressure traces that are both smooth or oscillatory. This can be most easily visualized in the format of a scatter plot, seen in Figure 2.11(b). For two hundred consecutive cycles from a single-cylinder engine, the integral in the range of 3-15 kHz of the DFT of each cycle is plotted versus the MPRR of each cycle. The color of the circle around five points in Figure 2.11 corresponds to the color of the pressure traces on the left of

Figure 2.10 and the frequency spectra displayed in the right plot of Figure 2.10.

Several observations can be made from this data. First, it can be seen that a single set of operating inputs produces a wide range of outputs in terms of ringing and pressure rise rate. Second, a high MPRR may occur without ringing, or they may occur together. There is a definite tendency for ringing to increase along with pressure rise rate and vice versa, but it's not always the case. Cycles with higher spectral power correspond to those with a greater peak on the frequency spectrum, and also have more visible oscillations on the pressure traces. This data implies that there is more to ringing than pressure rise rate alone, and reinforces the idea that HCCI is not easily controllable, since all of these points were taken on successive cycles using the same engine control inputs.

2.2.8   Origins of Pressure Inequality During Combustion

The key question to answer when it comes to ringing is where do the pressure waves come from? For a wave to form, the pressure in one region of the cylinder must be higher than that in another region.

As a thought experiment, if combustion proceeded uniformly and simultaneously everywhere in the cylinder, there would be no pressure inequality. The pressure rise rate could be infinitely high but no oscillations would be produced in this imaginary scenario because the pressure would rise at the same rate throughout the cylinder. We know from experiments that HCCI combustion is not a perfectly uniform and simultaneous process. Based on inhomogeneity in the cylinder of the variables in the kinetic rate equation, some areas of air and fuel react ahead of others and pressure inequality arises. It is important to note that this idea of inhomogeneity and pressure inequality introduces additional dimensions to our thought experiment concerning the ringing problem: The variation and progression of combustion in *space* becomes equally important as the progress of combustion in *time*.

How does the combustion proceed in both space and time such that these waves form? To begin to answer this question it is necessary to take a closer look at the

autoignition process and various modes of autoigniting wave propagation in combustion of premixed, gaseous air-fuel mixtures.

2.3   Autoignition Combustion Context

The goal of this section is to provide context by placing the current work in the larger body of literature concerning autoignited combustion phenomena.

Engine knock has long been a topic of interest for combustion scientists. The undesirable noise and engine damage make avoiding knock a crucial element of engine design. In spark ignited engines, knock occurs when the last bit of unburned air and fuel in the cylinder, termed the *end gas*, autoignites. This happens as a result of the end gas being compressed by expanding combustion products behind the advancing flame front. The autoignition of end gas creates a rapid dilatation, i.e. explosion, launching a pressure wave back through the burned gas. The end gas is usually very dense and comprises only a small fraction of the cylinder volume. By contrast, in the case of so-called *super knock*, the autoignition of the majority or entirety of charge takes place, and pressure waves emanating from initial autoigniting pockets travel through *reactive* gases (as opposed to burned gas, as in knock). Strong pressure waves from knock or super knock produce *ringing*, the pressure oscillations seen in pressure traces. Strong pressure waves can cause engine damage by disrupting thermal boundary layers and by producing high local pressures in the end gas, which damage piston rings [17, 22].

As SI engines progress toward downsized, highly turbocharged architectures, the problem of super knock has come to the forefront. The tendency toward autoignition increases as the charge becomes increasingly hot and dense as a result of turbocharging, and delaying autoignition until a flame can propagate through the entire charge becomes increasingly difficult [23]. The mechanism for super knock in turbocharged engines is described by Peters et al., building on the work of Bradley [24, 25]. Peters explains that the length scales of turbulence and the

inhomogeneities in the charge result in *reactivity gradients* that are ripe to form *developing detonations*. The terms developing detonation and reactivity gradient will be expounded upon further in the next section.

It is important to note that in the work of Peters et al., and as for highly turbocharged SI engines in general, the goal is to avoid autoignition and knock. In contrast, autoignition is the fundamental combustion mechanism in HCCI engines; avoiding it would not be useful. However, avoiding ringing and the high overpressures associated with it is necessary to prevent engine damage. Therefore, this work aims to understand the various modes of autoignition (and relevant gas dynamics) such that they can be used in a controlled and predictable manner for HCCI engines.

2.3.1   Modes of Reaction Wave Propagation

Temperature inhomogeneity in an engine is virtually unavoidable. Snyder found that temperature variations in the charge of an HCCI engine have a standard deviation of 25 K [26]. Some sources claim variations of up to 100 K [20]. These naturally-occurring temperature fluctuations, with length scales on the order of the turbulent integral scale, produce spatial gradients in ignition delay time, due to the strong temperature-dependence of reaction rate kinetics.

Following the work and classification originally described by Zeldovich (which was done for so-called *reactivity gradients*[6]), Sheppard describes three modes of autoignition propagation in HCCI engines based on initial local temperature gradients near the site of first autoignition, in a reactive mixture of uniform chemical composition [27, 28, 29]. The modes are:

(1) Thermal explosion
(2) Developing detonation
(3) Deflagration

---

[6]Reactivity gradients, as spoken of in work by Zeldovich and other authors, refers to gradients in ignition delay time, brought about by temperature gradients or inhomogeneities in chemical species.

In the *thermal explosion* mode, there are very small (or no) temperature gradients. Nearly the entire charge autoignites simultaneously, creating near-uniform pressure rise throughout, like our earlier thought experiment. Any apparent wave that appears is a function of slight differences in ignition delay time, but there is no coupling in the wave. The ignition of one parcel of gas does not affect the ignition of its neighbor. In the context of high-load HCCI, an extremely homogeneous premixed charge would autoignite simultaneously and uniformly in the thermal explosion mode. A high rate of pressure rise resulting from a strong mixture igniting uniformly would excite modes of vibration within the metal structure of the engine block, producing audible noise. This would affect NVH considerations but pressure waves would not form because of the uniformity of combustion among regions in the cylinder.

The *deflagration* mode is even more benign. Steep temperature gradients around the local inception of ignition dictate that neighboring parcels of gas are not close to achieving autoignition. They must wait for diffusive transport as a flame propagates out from the ignition center. Pressure waves produced from the dilatation of initial autoignition travel outward but are insufficiently strong to trigger additional autoignition.

The *developing detonation* mode bears the most relevance to this work. Gradients in temperature in the mixture that are between those of thermal explosion and deflagration conditions allow the gas surrounding a particular autoignition region to be compressed just enough, to induce autoignition. The energetics of autoignition–a large amount of chemical bond energy being converted rapidly into sensible energy– cause the temperature and therefore pressure of the combusting gas to increase. In an attempt to equilibrate pressure, the gas dilates. In non-dilute mixtures, the rate and energy density in the mixture require a very rapid expansion–one that is limited by the local speed of sound. This *gasdynamic impedance* creates an inequality of pressure at the boundary of the autoigniting gas which drives a strong compression wave. This wave travels outward, increasing the temperature and density of the unburned mixture as it passes. If the initial temperature gradient was such that the

increase in temperature brought about by the pressure wave is sufficient to incite further autoignition, the process continues, with the pressure wave being reinforced by additional autoignition and dilatation. These pressure waves can rapidly grow to be very large and steep (a shock), approaching the wave structure of a steady detonation. This gasdynamic coupling between pressure wave and reaction front lies at the heart of super knock and ringing in HCCI.

2.3.2   Detonation Physics

Even though the gasdynamic coupling observed in piston engines might not be classified as a detonation in the strictest sense, a great deal of prior work and understanding of the detonation phenomenon can be drawn upon for understanding pressure wave formation in engines. A steady-state detonation is defined as a coupled pressure wave and reaction front that are mutually reinforcing. Detonation physics can be simplified to one dimension, as in the case of planar or spherical detonations.   Detonations are governed by the Rankine-Hugoniot conditions: conservation of mass, momentum, and energy across an interface:

$$\rho_1 u_1' = \rho_2 u_2' \tag{2.2}$$

$$p_1 + \rho_1 u_1'^2 = p_2 + \rho_2 u_2'^2 \tag{2.3}$$

$$e_1 + \frac{p_1}{\rho_1} + \frac{1}{2} u_1'^2 = e_2 + \frac{p_2}{\rho_2} + \frac{1}{2} u_2'^2 \tag{2.4}$$

The velocities u_1' and u_2' are measured in the steady frame of reference of the detonation. It has been observed that stable, propagating detonations only exist as so-called Chapman-Jouguet detonations. In this case, the burned gas velocity in the frame of the shock is equal to the local sound speed. It can be shown by manipulating the Rankine-Hugoniot conditions that the Mach number of the unburned gas must

be greater than one. In other words, in a stationary reference frame the detonation wave travels at supersonic speed.

It is interesting that although a fully developed detonation in a uniform medium might be statistically stationary, it is not actually a steady phenonemon. The detonation front is composed of cells, with *wavelets* emanating out from exothermic reacting packets at the front. These wavelets form a diamond pattern, as can be seen in smoked foil images and other experimental images of detonations. The points where the wavelets intersect are nudged, or induced, by the wavelets to react, resulting in new reacting cells which in turn create more wavelets. The key to keeping the detonation wave propagating forward is that each reaction produces wavelets strong enough to re-initiate autoignition in a new cell. In this way, the steadily propagating detonation is made up of smaller, transient autoigniting units, continually initializing new units, which keep the overall wave propagating forward, in a statistically steady state.

Oppenheim was the first to obtain clear, time-resolved images of the detonation-to-deflagration transition (DDT) phenomenon [30]. In his images, we see the "explosion within the explosion" that leads to a coupled pressure wave and reaction front, generated from an initial turbulent flame front with pressure waves out in front of it. In the HCCI combustion and ringing being considered in this work, there won't be turbulent flames transitioning to detonations in the manner of DDT as imaged by Oppenheim. However, the transient occurrence of a dilatation producing a coupled pressure wave and reaction front (or developing detonation), is likely to take on a similar structure to the initial coupling observed in a DDT.

Authors such as Lee have described the distinction between "blast-ignited" detonations, where an external ignition source provides input energy to trigger a detonation in a reactive mixture, and "self-ignited" detonations, often studied as DDTs [31]. Both of these categories are typically used to distinguish between detonation formation modes in homogeneous mixtures. Developing detonations of interest in the present work take place in the absence of a deflagration, and in a

non-homogeneous mixture. It is possible, as will be seen in model results of Chapter 4, for combustion events in one part of the cylinder to produce pressure waves which trigger autoignition in another region by arriving just as that region is about to autoignite. For this reason, previous research on the topic of blast-ignited detonations may aid in understanding ringing in IC engines.

2.3.3   Detonations in Non-Uniform Mixtures

Some insightful work has been done on the topics of the onset of detonation, as well as the propagation of detonations, in gases of non-uniform temperature or composition. Both of these areas will help shed light on the formation of developing detonations in engines.

Zeldovich was the first to explore the topic of detonation onset in non-uniformly preheated reactive gas mixtures [32, 28]. He derived equations describing the autoignition gasdynamics of a gas with the initial conditions of uniform pressure and composition, zero velocity, and a temperature gradient that varied linearly in space. Chemical reactions were modeled as one-step chemistry with a fixed heat energy release, pre-exponential factor, and activation energy. An initial temperature of 2000 K was chosen and temperature gradients of -7360, -220, -118, and -11 Kelvin per centimeter were presented. He used these to demonstrate how autoigniting reaction fronts propagated differently with initial conditions of steep, medium, and shallow temperature gradients, and used these to support the three previously-defined categories of *thermal explosion*, *developing detonation*, and *deflagration*. In the case of the steepest temperature gradient, an initial pressure wave went out ahead of the reaction zone. The third temperature gradient, -118 K/cm, produced a developing detonation, and the fourth, -11 K/cm, produced a thermal explosion. He also included the second temperature gradient, -220 K/cm, to show that these categories may be slightly blurred. In this case there is initial gasdynamic coupling followed by separation where the pressure wave travels out ahead of the reaction wave. This categorization of autoigniting waves built on

much of Zeldovich's own earlier work on detonation theory [33].

2.3.4   Time-Scale Analysis of Developing Detonations

Another very important body of work relevant to the problem of pressure waves in piston engines analyzes the various time scales in play during autoigniting combustion events. This type of analysis allows relationships to be established that are independent of a specific fuel or fuel-air mixture. The relative time scales associated with wave travel, ignition delay, and reaction rate, provide useful ways to think about which autoignition mode will arise in a given fuel-air mixture.

As engine load is increased, the air-fuel-exhaust mixture becomes increasingly reactive and the likelihood of favorable temperature gradients for the formation of developing detonations becomes high. Upon inception of autoignition in the most reactive regions, the initial dilatation is stronger because of the energy dense mixture. Thus, it is more likely to encounter gasdynamic impedance imposed by the sound speed, leading to coupling and the formation of a developing detonation. This reinforces the understanding that lean engine operation or dilution with an inert moderator makes super knock less likely than in an otherwise-identical non-dilute, stoichiometric mixture, and also explains why downsized, turbocharged architectures are more susceptible to pre-ignition.

The work of Bradley and Morley combines time scales relevant to both ignition delay time and mixture strength in an attempt to capture this effect. They identified non-dimensional groups in an attempt to quantify the critical temperature gradient for developing detonations to form, suggesting that at such a gradient, the propagation speed of the reaction wave would approximately match the local sound speed [34]. An autoigniting wave will travel at a speed based on ignition delay time in a non-homogeneous reactive mixture, and the local sound speed is the speed at which acoustic waves resulting from combustion will travel outwards from the originating hot spot. Bradley et. al. describe "resonance" in the reacting mixture as the perfect match between autoignition wave speed and

acoustic wave speed. First, the speed of the autoigniting front is described by:

$$u_a = \left(\frac{\partial \tau_i}{\partial r}\right)^{-1} \tag{2.5}$$

In the above equation, u_a is the speed of the reaction wave, τ_i is ignition delay time, and r is the radial dimension outwards from the center of the autoigniting gas. This can be re-written in terms of temperature gradient in space:

$$u_a = \left(\frac{\partial \tau_i}{\partial T} \frac{\partial T}{\partial r}\right)^{-1} \tag{2.6}$$

where $\frac{\partial \tau_i}{\partial T}$ represents the variation of ignition delay time with temperature, and $\frac{\partial T}{\partial r}$ describes the variation of mixture temperature in space. Finally, by equating the reaction wave speed u_a with the local sound speed a, a "critical temperature gradient" in space can be expressed in terms of ignition delay time and acoustic speed:

$$\left(\frac{\partial T}{\partial r}\right)_c = \frac{1}{a\left(\frac{\partial \tau_i}{\partial T}\right)} \tag{2.7}$$

A quantity, ξ can then be defined to quantify how close any mixture is to its "resonant" condition by calculating the ratio of wave speed to sound speed.

$$\xi = a/u_a \tag{2.8}$$

This *wave speed ratio* ξ can be used as a proxy for how likely a developing detonation is to form.

In theory, gradients much larger or smaller than the critical one would not exhibit coupling. However, using a numerical model of developing detonations, Bradley found that for strong, dense mixtures close to stoichiometric, temperature gradients up to 30 times the critical value could support coupled pressure waves and reaction fronts. This means that coupling can occur over a very large range of potential temperature gradients, not just a narrow range considered "resonant."

To capture this effect, Bradley and Morley introduced a second relationship,
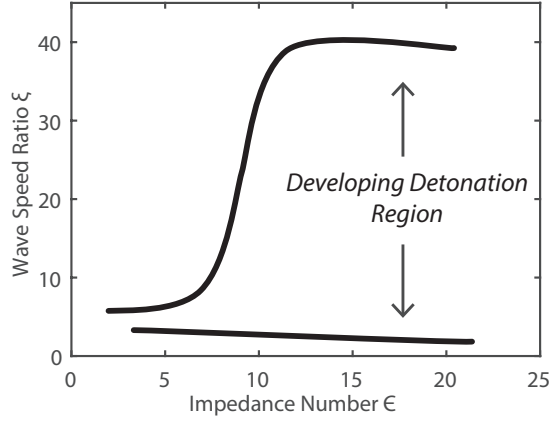
Figure 2.12: Developing detonation region as a function of non-dimensional groups, *wave speed ratio* ξ and *impedance number* ϵ. Based on the analysis of Bradley [25].

using the property characteristic of a reactive mixture's "excitation time." Excitation time is defined as the elapsed time between the points of 5% and 90% of the total exothermicity of the reaction. A non-dimensional group ϵ is formed by

$$\epsilon = (r_o/a)/\tau_e \tag{2.9}$$

where r_o is the radius of the initial reacting region, τ_e is its excitation time, and a is the local sound speed. This can be thought of as an *impedance number*, as it represents a ratio of the rate the reacting parcel *can* dilate compared to the rate of exothermicity of the reactions causing it to dilate.

Excitation times are much shorter for oxygen-fuel mixtures than for air-fuel mixtures, and this affects flammability limits and detonability limits. Not only must a mixture be sufficiently flammable, but the chemical reactions must provide enough energy and at the right time-scale to produce a self-reinforcing, propagating wave. For larger values of impedance number ϵ, the range of values of wave speed ratio ξ which give rise to developing detonation increases. This can be seen in Figure 2.12.

2.3.5   Fuel Chemistry Effects

Some fuels exhibit more complex autoignition behavior than others which can affect the propensity to produce developing detonations. For example, iso-octane and gasoline exhibit *single-stage ignition* behavior, whereas a fuel such as PRF80 (80% isooctane and 20% n-heptane by volume) exhibits two-stage ignition behavior [35]. Two-stage ignition refers to a combustion process that first exhibits a period of low-temperature reaction with little exothermicity followed by a period of rapid reaction and high exothermicity. Single-stage ignition on the other hand exhibits only a rapid, exothermic reaction sequence. In experiments, Dec and Sjöberg, Dahl, and others, have noticed that single-stage ignition fuels tend to have a much weaker dependence on local equivalence ratio ϕ than two-stage ignition fuels, which have been shown to be very "phi-sensitive." This has implications for certain high-load strategies such as charge stratification. Only for fuels which exhibit a phi-sensitive autoignition behavior will charge stratification be a useful method to moderate the overall exothermicity rate during the combustion process [36, 37, 38]. Further, a consideration of reactivity gradients imposed by equivalence ratio variation will have differing results depending on the ignition characteristics of the fuel.

For many hydrocarbon fuels, the relationship between temperature gradients and gradients in ignition delay time is fairly straightforward. A higher temperature yields a shorter ignition delay time. However, a number of fuels prevalent in transportation applications exhibit a behavior termed *negative temperature coefficient*, meaning the relationship between temperature and ignition delay time is not monotonic. For fuels that exhibit this behavior, there is a temperature range in which a higher temperature produces a longer ignition delay time. This means that temperature gradients do not automatically lead to similarly-sloped gradients in ignition delay time.

The observations of Dahl et al. of autoignition in non-uniform mixtures revealed that most often the slightly fuel-lean regions ignite first, before the stoichiometric or fuel-rich regions [39]. They observed that temperatures were slightly lower in rich regions of the combustion chamber and higher in lean ones. The tendency for

leaner, hotter regions to ignite first implies that the chemical kinetics of combustion reactions are *more* sensitive to the temperature difference than fuel concentration in these cases.

The effects of fuel chemistry serve as additional motivation to undertake experimental investigation of ringing. Complicated fuel chemistry effects such as "phi-sensitivity" and NTC are difficult to capture in analytical expressions or even a computational model.

2.4   Revisiting Svrcek's Water Injection Result

The theory of pressure wave formation is quite well-developed and modeled in simplified laboratory settings. However there are very interesting engineering questions that have not yet been adequately answered concerning pressure waves in piston engines. How can these waves be stopped? We return to the data presented in Section 1.3, where water injection unexpectedly disrupted ringing pressure waves in premixed combustion of stoichiometric methane/air at 60:1 compression ratio [5].

The water injection not only suppressed ringing but also lowered the maximum pressure rise rate by a factor of 30. However, the amount of water injected was relatively small, only about 8 percent of the total mass, not a significant enough amount to moderate the overall reaction (and far less than the amounts of EGR required to moderate the combustion process in much less-extreme engine environments).

A very important observation that can be made in Figure 2.13 is that for the ringing case, the peak pressure is higher than it would be even for an infinitely rapid (homogeneous, constant volume, adiabatic) combustion process. The pre-combustion thermal state indicated by the arrow corresponds to an equilibrium pressure of 640 bar, as indicated by the dashed line. Even if an infinite rate of pressure rise were imposed, and all of the fuel reacted at once, the combustion gases would not reach the peak pressure seen in the ringing case. This suggests that a portion of the
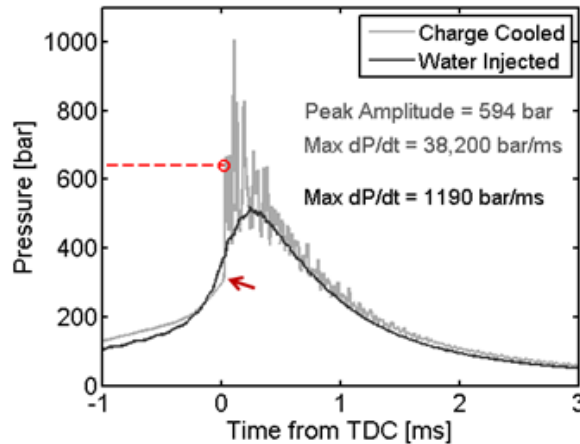
Figure 2.13: Two pressure traces from an extreme compression free-piston engine. The charge is stoichiometric, premixed, non-dilute methane and air at 60:1 compression ratio. Comparison is made between combustion phased by charge cooling and water injection [5]. The red arrow indicates the pre-combustion state for the charge-cooled case and the red circle indicates the constant-volume pressure.

reactants were pre-compressed beyond the compression resulting from piston motion before igniting, indicating pressure inequality in the cylinder and a definite spatial component to the ringing phenomenon.

One theory is that the water injected down the centerline of the cylinder created an inverted temperature profile, where typically the hottest gases would be found in the center. The areas of the mixture with shortest ignition delay would have then been located in a ring-shape, between the watery core and the surrounding thermal boundary layer at the cylinder wall. This could have resulted in steeper than expected temperature gradients, or some sort of destructive interference between waves. Since the mixture was very energy-dense, it would be located far to the right of the $\xi - \epsilon$ plot in Figure 2.12, and would permit a wide range of temperature gradients to produce developing detonations. Perhaps developing detonations did form and were disrupted by encountering water-rich pockets of cold gases. A more general, over-arching question that can be formulated based on these data is how might developing detonations interact with a similarly deliberate and atypical inhomogeneity in a real

engine? And could these lead to a method to engineer the suppression of these waves?

2.5 The Path Forward

We would like to know how the autoignited combustion process proceeds within an engine in both space and time, but our current tool for measuring pressure, the pressure transducer, only gathers data at a single point in space, located on the wall of the combustion chamber. Knowing that there will be pressure inequality in the cylinder causes a pressure transducer to be an incomplete source of information about the state of gases in the cylinder at a given time. Previous experiments have been performed using multiple pressure transducers to get data at multiple locations in the cylinder wall, but it would be best to have information throughout the combustion chamber, not just at walls [40].

This problem can be tackled in two ways:

1) *Modeling:* Identify and model the essential physics involved in formation of pressure waves. Develop a model that is useful in understanding which conditions give rise to pressure waves and which do not. Use this to interpret and understand engine data in terms of the essential physics of the coupled chemistry and gasdynamics.

2) *Optical access engine experiment:* Build an experiment to permit imaging of the waves forming during combustion in a piston engine. Use appropriate imaging techniques to gather relevant information such as the location of exothermic reactions and the waves in the engine. Do this at conditions typical of high-load combustion engines—meaning high pressure and energy-dense mixtures.

In the following chapters, the details of both of these approaches are described, and results from both model and experiment are presented.

Chapter 3

Numerical Model

A 1D spatially-resolved numerical model of the gases during the combustion process was developed to aid in understanding the gasdynamic impedance and coupling which underly the ringing phenomenon. The model is used to provide insight into the numerous processes and properties involved, and to understand which aspects of the combustion process are most important to the onset and propagation of developing detonations.

The numerical model is intended to be a tool for use in interpreting experimental results, and also provide direction and focus for future experimental investigation. Modeling decisions reflect the goal of building a computational compliment to experimentation, rather than a comprehensive, predictive combustion model. The model is first used to illustrate and understand the coupling, and then to explore conditions that either reinforce or disrupt the formation of damaging pressure waves.

3.1 Essential Physics

The reacting compressible flow model developed in this work is intended to effectively demonstrate the ringing phenomenon. It must encompass the essential underlying

physical processes inherent to the combustion regimes at work in HCCI and other premixed, autoignited, combustion engines. Referring to the regime classification of Zeldovich described in section 2.3.1, the two modes of interest are the *thermal explosion* and *developing detonation* modes.

Several models in the literature already exist to capture the gasdynamic coupling of developing detonations [25, 27, 28, 34, 41]. Gases are well-modeled using the fluid mechanics equations for inviscid, compressible flow. The parent equations of fluid mechanics, the Navier-Stokes Equations, are simplified into the Euler Equations when viscous terms are neglected. In the flow and reaction regime of interest to gaseous detonation waves, viscous terms are dwarfed by pressure and momentum terms. Further, molecular diffusion and heat conduction act on a significantly slower time scale than pressure wave speeds, and as a result may also be neglected. By neglecting molecular diffusion, the deflagration mode is not modeled and model results are interpreted accordingly.

It is also desirable for this model to capture the chemical reactions in detail, with sufficiently simplified fluid mechanics to make the problem tractable and useful for asking a wide range of questions. Such questions include the interaction of developing detonations with spatial inhomogeneity in fuel concentration, or with varying amount of an inert moderator. Many similar models have reduced the chemical reactions to a one-step heat addition model, where fuel energy is simply added to the cell when it is determined it is time for the fuel to combust [27, 28, 32, 42]. Detailed chemical kinetics are implemented in this work to explore chemical effects in greater detail. These include moderator participation in development and suppression of the gasdynamic coupling, and significant variation of chemical composition throughout the domain, either in the form of stratified fuel or spatially segregated moderators. For additional motivation, Liberman et al.[43] determined that detailed kinetics significantly impacted modeling of the initiation of detonation, as compared to a one-step chemistry approximation. They note especially that a significantly longer spatial temperature gradient is required to

initiate a detonation when using detailed chemistry than with using one-step heat addition [43].

In spatial coordinates the model is reduced to a single dimension, as are most other similar models. Even though in reality the combustion process occurs in three dimensions, this is still a valid way to answer the questions of interest to this work because the fluid-mechanic-and-chemically-reacting structures that comprise developing detonations can all be simplified to one dimension. Detonations are often described using one dimension, such as in the case of planar or spherical detonations. Unlike turbulence, which inherently must be expressed in three dimensions, a reduced number of spatial dimensions is generally thought to be sufficient to capture the essential physics of the developing detonation process.

The most difficult requirement to meet in modeling developing detonations is that the model cannot be limited to sub-sonic flow regimes, as many of the most widely-used computational fluid dynamics (CFD) models are. Many codes which are used to study ringing combustion in HCCI engines and to predict the limits of the operating range, state up front that they are unable to resolve acoustic waves in the engine, assuming a uniform cylinder pressure in calculations [23] [44] [45] [46]. These models are not suited to answering questions about the developing detonation process itself. The need to resolve flow structures such as shock waves and thin, autoigniting reaction zones eliminates the possibility of using many of the readily available commercial and educational CFD packages.

After choosing the desired abilities and acceptable limitations of the model which suited the application and types of questions to be answered, the best path forward was to develop a 1D reacting compressible flow model similar to many in the literature, that included the capability for detailed chemical kinetics.

3.2   Reactive Euler Equations

The relevant equations for the reacting compressible flow model are the Euler Equations in one dimension, including conservation of mass, momentum, energy, and species [47].

$$\frac{\partial \rho}{\partial t} + \frac{\partial (\rho u)}{\partial x} = 0 \tag{3.1}$$

$$\frac{\partial (\rho u)}{\partial t} + \frac{\partial (\rho u^2 + P)}{\partial x} = 0 \tag{3.2}$$

$$\frac{\partial}{\partial t}(-P + \frac{\rho u^2}{2} + \rho h) + \frac{\partial}{\partial x}(\frac{\rho u^3}{2} + \rho u h) = 0 \tag{3.3}$$

$$\frac{\partial (Y_i \rho)}{\partial t} + \frac{\partial (Y_i \rho u)}{\partial x} = \dot{\omega} \tag{3.4}$$

In the above equations, Y_i refers to the mass fraction of each chemical species. As a system, the Euler equations in the absence of chemical reaction take the following form. The vector $\vec{U}$ is the vector of unknowns that will be advanced in time to observe how the combustion process proceeds.

$$\vec{U}_t + [\vec{F}(\vec{U})]_x = 0 \tag{3.5}$$

where

$$\vec{U} = \begin{pmatrix} \rho \\ \rho u \\ E \end{pmatrix}, \quad \vec{F}(\vec{U}) = \begin{pmatrix} \rho u \\ \rho u^2 + P \\ (E + P)u \end{pmatrix}$$

and

$$E = -P + \frac{\rho u^2}{2} + \rho h \tag{3.6}$$

In cases of multi-species, chemically reacting flows, additional species conservation equations are added to the above system. Each species conservation equation takes a similar form to that of the mass conservation equation, with the difference being that the left hand side is in terms of mass fractions, while the right hand side consists of a source term $\dot{\omega}$ to account for creation and destruction of species through reactions. In this way we can write an expanded system of conservation equations, adding one equation for each species.

$$\vec{U}_t + [\vec{F}(\vec{U})]_x = \vec{S} \tag{3.7}$$

where

$$\vec{U} = \begin{pmatrix} \rho \\ \rho u \\ E \\ \rho Y_1 \\ \vdots \\ \rho Y_{NS-1} \end{pmatrix}, \quad \vec{F}(\vec{U}) = \begin{pmatrix} \rho u \\ \rho u^2 + P \\ (E+P)u \\ \rho u Y_1 \\ \vdots \\ \rho u Y_{NS-1} \end{pmatrix}$$

and

$$E = -p + \frac{\rho u^2}{2} + \rho h \tag{3.8}$$

In the above equations NS refers to the number of chemical species in the reacting system. There are $NS - 1$ species conservation equations because the $NSth$ mass fraction is given by $1 - \sum_{i=1}^{NS-1} Y_i$.

The chemical reacting source term $\vec{S}$ on the right can be expressed in terms of

the mass production rates $\dot{\omega}$.

$$\vec{S} = \begin{pmatrix} 0 \\ 0 \\ 0 \\ \dot{\omega}_1(T, P, Y_1, Y_2, ..., Y_{NS-1}) \\ \vdots \\ \dot{\omega}_{NS-1}(T, P, Y_1, Y_2, ..., Y_{NS-1}) \end{pmatrix} \tag{3.9}$$

3.3   Thermodynamic Properties

In choosing both a property method and numerical methods to solve the above equations, it is important to consider a method that is amenable to implementing realistic fluid properties. To provide a counterexample, a method that considered values of specific heats to be constant despite chemical reactions and wide temperature ranges would be unrealistic.

The experimental conditions are well modeled as a mixture of ideal gases. Intermolecular forces between gas molecules are neglected, and the values of specific heat are only a function of temperature. Thus thermodynamic properties such as enthalpy can be expressed as an integral over temperature (using the placeholder variable τ):

$$h(T) = h(T_{ref}) + \int_{T_{ref}}^{T} c_p(\tau)d\tau \tag{3.10}$$

The enthalpy at $T_{ref} = 298.15$ Kelvin is also called the heat of formation h^f. The values of heats of formation for various chemical species are known constants for a specified reference temperature and can be found in the JANAF Thermochemical Tables [48]. For a multi-species mixture the enthalpy of the mixture can be described

as

$$h = \sum_{i=1}^{NS} Y_i h_i^f + \int_{T_{ref}}^{T} \sum_{i=1}^{NS} Y_i c_{p,i}(\tau) d\tau \tag{3.11}$$

And the equation of state is the ideal gas law for the partial pressure of each component.

$$P_i = \rho Y_i R_i T \tag{3.12}$$

For the implementation of the above property definitions, thermodynamic ideal gas properties with temperature-dependent specific heats are evaluated for the gas mixture using Cantera [49].

3.4 Numerical Methods

3.4.1 Spatial Derivatives

In order to solve for $\vec{U}$ and march forward in time, the other terms in the system must be evaluated. The term $[\vec{F}(\vec{U})]_x$ is a partial derivative in space of the F vector. Calculating this derivative requires a spatial discretization of the model domain. The spatial partial derivatives are calculated using a third-order Essentially Non-Oscillating (ENO) scheme, following the method of Fedkiw [50]. A third order ENO scheme is chosen over something simpler, such as a first-order Godunov method, because it is sufficiently resolved to capture the steepness of shocks to a reasonable extent, and also robust enough to handle regions with rapidly-changing properties such as narrow reaction zones. An ENO scheme works by evaluating a number of different *stencils* (essentially the set of property values of the cell of interest and its neighbors) for calculating spatial fluxes at each location along the model grid and chooses the one that produces the least oscillations. Numerical problems with steep, traveling fronts are especially vulnerable to numerical oscillations because of the high values of derivatives at the location of the front. These oscillations can be avoided by

choosing stencils just behind the shock as it travels, a technique called *up-winding*. However, the ENO scheme is preferable to this approach since it inherently chooses the least-oscillating stencil at every point and does not require knowledge of which direction the waves will be traveling so as to assign stencils behind them.

Fedkiw formulated the reacting compressible flow problem in a way that is especially easy to solve using an ENO scheme because of the way he addressed thermodynamic properties. The Jacobian matrix describing the system can be written analytically in terms of thermodynamic and fluid properties without the assumption of constant specific heat. Thus analytical derivatives required for numerics can be evaluated quickly using Cantera for properties without taking numerical derivatives of these quantities, as might otherwise be necessary when implementing variable specific heats of a changing gas mixture in a numerical problem.

The spatial fluxes are computed by the ENO scheme and then integrated in time using a forward Euler scheme. The time step is determined from the Courant number, $C = \frac{\bar{v}\Delta t}{\Delta L} \leq 1$. The term $\bar{v}$ refers to the maximum speed that information could travel, and is calculated from the absolute value of the highest value of sound speed in the domain added to the highest velocity in the domain. The term ΔL refers to the grid spacing of the discretized domain. This relationship ensures that time steps are chosen to be small enough that information cannot traverse an entire cell within that time [47].

The model has been formulated such that 1D reaction waves can be modeled in either Cartesian, Cylindrical, or Spherical coordinate systems, and the desired coordinate system for each case can be set as an input to the model. This is useful for comparing the model to various validation cases which may be in different coordinate systems, and also valuable for thinking about gasdynamic coupling in one spherical dimension compared to one Cartesian dimension, for example.

The Euler equations in cylindrical and spherical coordinates have an additional term compared to the Cartesian equations because of the product rule derivatives

such as $\frac{1}{r}\frac{\partial}{\partial r}(rF_r)$ for cylindrical and $\frac{1}{r^2}\frac{\partial}{\partial r}(r^2 F_r)$ in spherical coordinates. In the radial dimension the two equations, cylindrical and spherical respectively, are as follows:

$$\frac{\partial U}{\partial t} + \nabla \cdot F(U) - \frac{1}{r}F(r) = 0 \tag{3.13}$$

$$\frac{\partial U}{\partial t} + \nabla \cdot F(U) - \frac{2}{r}F(r) = 0 \tag{3.14}$$

3.4.2 Chemical Kinetics

Chemical kinetic equations require special consideration in numerical problems. The $\dot{\omega}$ source terms cause the system of equations to be numerically stiff. The reaction rates for methane-air combustion are determined from the thermodynamic state in each cell using the GRI30-MECH [51], and then integrated separately from the fluid mechanics terms using the CVODE stiff solver [52]. This is an adaptive solver that chooses time steps small enough to handle the stiffness of the kinetics equations. The solver is able to re-evaluate the thermodynamic state as the chemical composition updates for each of its time-steps, querying for updated reaction rates from GRI30-MECH as it marches along. The chemical kinetics sub-routine runs anew for each model time step, Δt, and in each cell.

The sheer number of independent kinetic computations required to evolve reactions in different cells each time step lends itself naturally to a parallel computing approach. Additionally, the spatial derivative calculations of ENO scheme itself are also well-suited for parallel computations. To take advantage of this, the code was written to enable multi-threading. The code takes as an input the number of cores it can run on and for each time step it executes the calculation of both spatial derivatives and chemical kinetic reactions of different cells in a parallel manner.

3.5   Model Validation

The purpose of the model is to capture the gasdynamics of a reacting compressible flow, and the model test cases reflect that goal. Three sets of validation results are presented here, in order of increasing complexity: (1) the Sod shock tube problem, (2) a comparison to a Chapman-Jouguet detonation, and (3) developing detonation calculations available in the literature.

3.5.1   Validation Using Sod Shock Tube

First, the Sod shock tube problem is attempted, to ensure that the dynamics of waves in non-reacting compressible flow, as captured by the model, are accurate [53]. The problem is set up with two halves of a shock tube separated by a diaphragm, such that inequality of pressure and density exist at the start. Following the diaphragm burst, three features form: a left-traveling rarefaction, contact discontinuity, and a right-traveling shock. An analytical solution exists for this problem, which is plotted in Figure 3.1 along with the model results. This is a canonical first test problem for compressible flow models, and the ENO scheme shows good agreement with the analytical solution.

3.5.2   Comparison to Steady Chapman-Jouguet Detonation

In order to validate the model's ability to capture coupled chemical reactions and compressible flow behavior, the Chapman-Jouguet detonation was considered. Given the initial pressure, density, and composition of a fuel-air mixture, the resulting pressure, density, sound speed, and wave speed of a C-J detonation can be determined from the equations describing the C-J conditions, which enforce conservation of mass, momentum, and energy across the detonation interface:

$$\rho_1 u_1' = \rho_2 u_2' \tag{3.15}$$
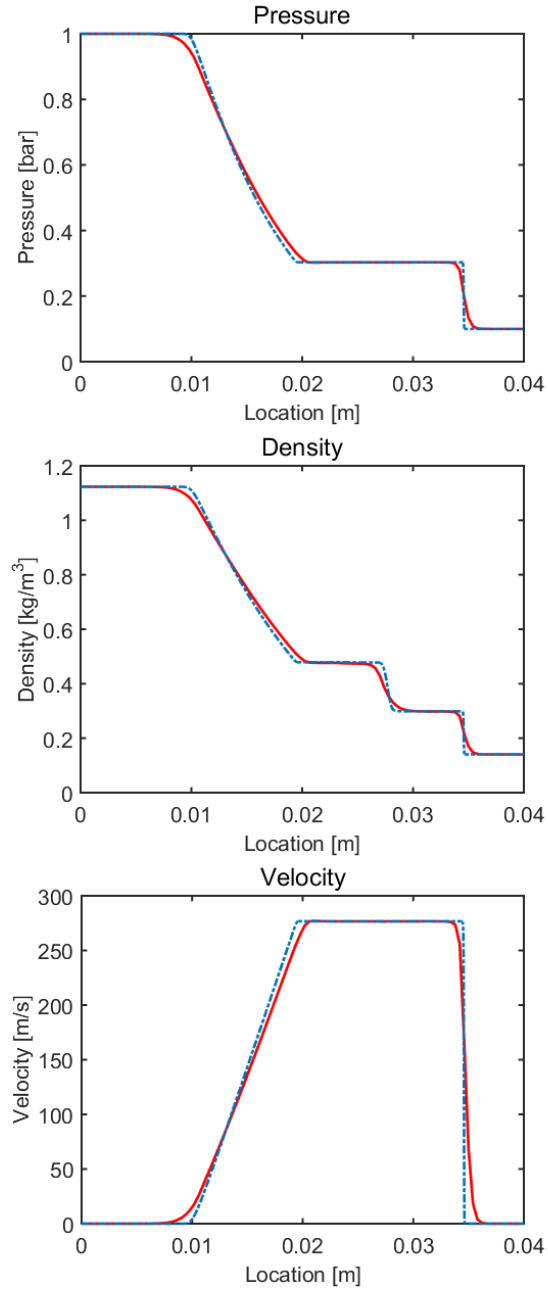
Figure 3.1: The results of the reacting compressible flow model presented in this work are plotted in a solid red line. The solution to the non-reacting Sod shock tube problem is plotted for comparison in a dot-dashed blue line.
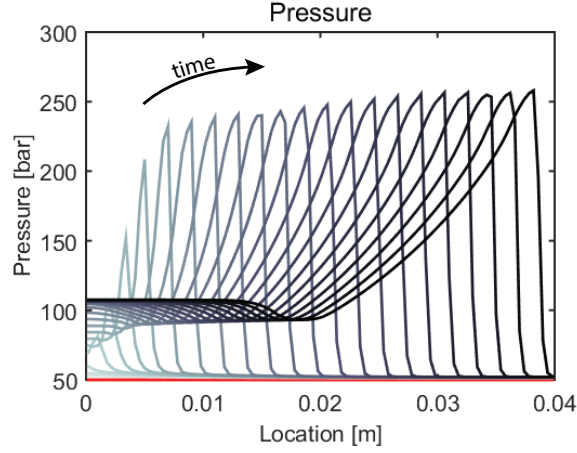
Figure 3.2: Spatial development of developing detonation plotted at multiple instants in time during its formation.

$$p_1 + \rho_1 u_1'^2 = p_2 + \rho_2 u_2'^2 \tag{3.16}$$

$$e_1 + \frac{p_1}{\rho_1} + \frac{1}{2}u_1'^2 = e_1 + \frac{p_2}{\rho_2} + \frac{1}{2}u_2'^2 \tag{3.17}$$

Table 3.1: Comparison of the C-J condition prediction and model results for a methane/air mixture at 0.95 equivalence ratio and initial pressure of 50 bar.

	C-J Calculation	Numerical Model	Percent Difference
Pressure	217 bar	228 bar	5.07%
Density	19.5 kg/m^3	21.7 kg/m^3	11.3%
Wave Speed	1930 m/s	1980 m/s	2.59%
Velocity	693 m/s	701 m/s	1.15%

The u' in the above equations are velocities in the frame of the shock. The C-J conditions corresponding to a mixture of 0.95 equivalence ratio methane-air initially at 50 bar were computed iteratively, based on the lower heating value (LHV) of methane and using the assumption of constant specific heat ratio behind the shock
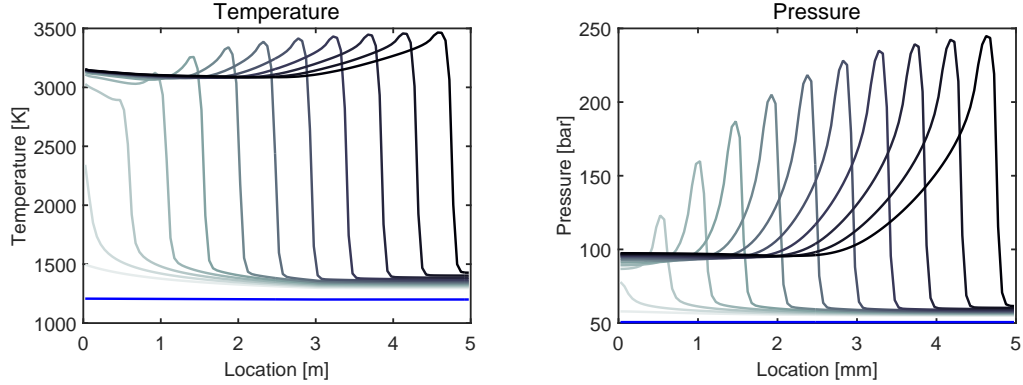
Figure 3.3: Stoichiometric 0.5 H$_2$ – 0.5 CO – air mixture initially at 50 atm. An initial hot spot 3 mm in size at the left of the domain has a temperature elevated approximately 7.5 K above the rest of the domain, which is initially at 1200 K. The calculation was carried out in spherical coordinates for comparison with the results of Bradley and Morley [34]. Profiles are plotted at the following times: $t = 0.00\,\mu s, t = 54.1\,\mu s, t = 54.7\,\mu s, t = 55.1\,\mu s, t = 55.4\,\mu s, t = 55.7\,\mu s, t = 56.0\,\mu s, t = 56.3\,\mu s, t = 56.6\,\mu s, t = 56.9\,\mu s, t = 57.1\,\mu s, t = 57.4\,\mu s, t = 57.6\,\mu s$.

of 1.37.[1] The numerical model was then used to compute the case of a developing detonation with the same initial pressure, temperature, and composition as the C-J calculations. A plot of pressure as a function of space can be seen in Figure 3.2, in which each profile represents the pressure wave shape at a different instant in time. At the far right side of the domain, the wave is approaching a fully-developed detonation. Conditions for this point can be compared with calculations of the corresponding C-J point in Table 3.1 and show good agreement. The peak pressure is within 6% of the theoretical pressure, and the wave speed within 2%.

3.5.3   Comparison to Results of Bradley and Morley

The calculations of Bradley and Morley were repeated to ensure that the numerical model could reproduce the results of similar models in the literature which are used

---

[1]Recall that the assumption of constant specific heat is *not* made in the reacting compressible flow model
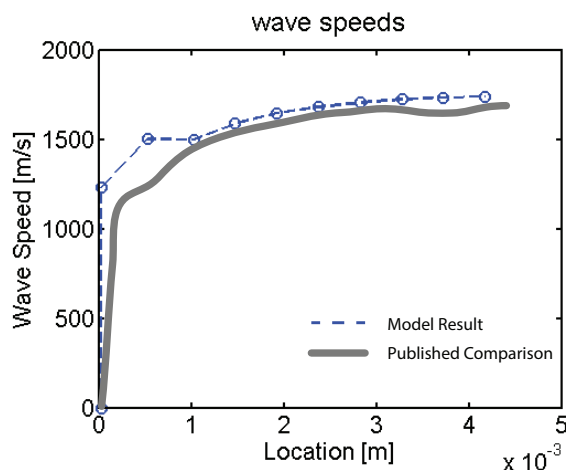
Figure 3.4: Wave speeds as calculated in the present work alongside re-plotted wave speeds published by Bradley and Morley [34]. Stoichiometric $0.5 - H_2 - 0.5$ CO – air mixture initially at 50 atm. An initial hot spot 3 mm in size at the left edge of the domain has a temperature elevated approximately 7.5 K above the rest of the domain, which is initially at 1200 K. The calculation was carried out in spherical coordinates.

to investigate the developing detonation phenomenon in IC engines [34]. The case of a stoichiometric $0.5\,H_2 - 0.5\,CO$ – air mixture which autoignites to form a developing detonation is modeled in spherical coordinates. The initial temperature of the bulk gas is 1200 K and a temperature elevation of approximately 7.5 K, representing a hot spot in the engine, is found at the left end of the domain. From the hot spot, the temperature linearly decreases back to 1200 K over the course of the first 3 mm of the domain. The initial pressure is 50 atm. The results for temperature and pressure profiles are shown in Figure 3.3. Values of wave speed, extracted from the model results, are plotted in Figure 3.4 alongside the published wave speeds [34]. The results show good agreement with published results.

There is a difference in induction time between the results published by Bradley and those computed here, but the induction time is very sensitive to initial conditions. Once the autoignition develops and waves become important, the results are in very good agreement, including the wave speeds shown in Figure 3.4.

The wave speeds differ, on average, by 4-5% from those published by Bradley. This is especially promising since this demonstrates the model's ability to reproduce the *developing* part of the developing detonation, in addition to the steady detonation wave computed in the previous validation case.

3.6 Illustrative Results

3.6.1 Developing Detonation

First a demonstration of the developing detonation mode is made using the numerical model. The plots in Figure 3.5 reveal how a mixture with an initial temperature gradient evolves to produce a steep propagating pressure spike rather rapidly after an initial ignition delay time. The origin of autoignition takes place at an initial temperature of 1300 K, on the left side of the domain. A temperature gradient of -1 K per mm is initially present in the mixture, starting at the left side at 1300 K and sloping downward. The initial pressure in the mixture is 50 bar, and the mixture has uniform composition throughout the domain, consisting of methane and air with an equivalence ratio of one.

On each figure, each profile represents an instant in time, as the wave progresses through space from left to right. Profiles of the same color correspond across plots of pressure, temperature, etc., so that the coupling and time evolution of variables may be observed.

The gasdynamic coupling is evidenced by the co-location of the pressure peak and the sharp drop in methane mole fraction. The expansion of combustion products is impeded by the local sound speed, resulting in a steep pressure front. The pressure peak increases in amplitude as it travels in space, indicating that the exothermicity of subsequent adjacent chemical reactions is reinforcing and strengthening the peak. In this way, spatial gradients in temperature and/or reactivity can lead to conditions which produce pressures higher than would be seen with constant volume combustion, since reactants are pre-compressed by a pressure wave before reacting. In this case,
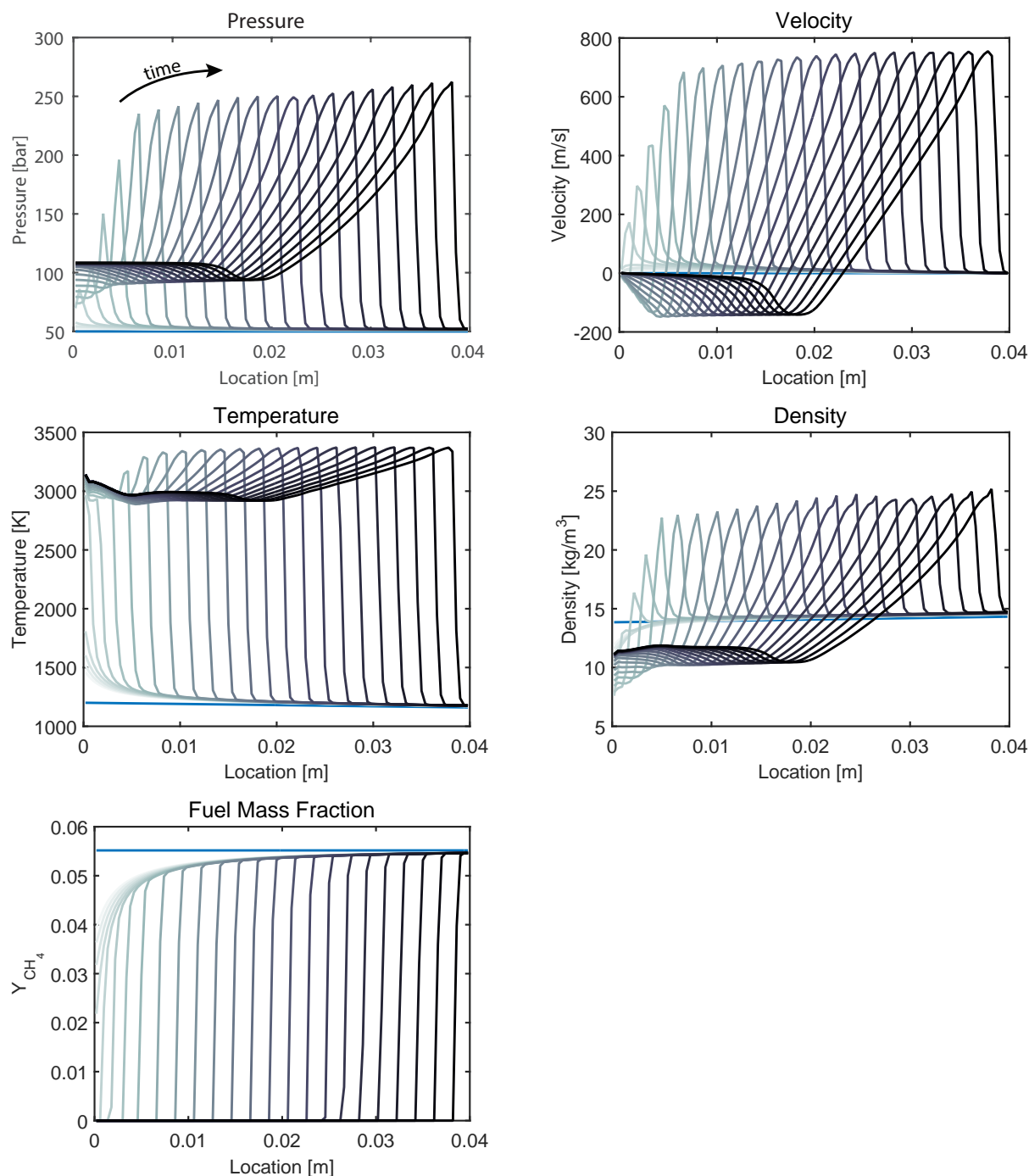
Figure 3.5: Developing detonation mode demonstrated with initial temperature gradient of 1 K/mm and initial pressure of 50 bar. Methane/air mixture at unity equivalence ratio. Times ranging up to 272 μs. Successive plotted profiles are spaced 1 μs apart toward the end of the simulation.

the constant volume-combustion pressure[2] is 124 bar, while the pressure peak in the model develops a local pressure of over 200 bar. In the plot of density profiles, the peak values, which occur right before reaction, are approximately 60% higher than the initial density. This is similar to having a 60% increase in local compression ratio compared to the base compression ratio of the engine. The large amount of chemical energy converted to sensible energy in such a dense reaction zone causes the gas to expand, but the gasdynamic impedance imposed by the sound speed prevents spatial pressure equilibration, thus strengthening the traveling pressure peak. If the profiles were plotted at further time steps, the pressure wave would reach the wall—with all of the fuel consumed—and reflect off the wall to travel back and forth in an oscillating manner. An imagingary pressure transducer situated in the right side wall of the domain would register a sharp increase in pressure upon arrival of the wave, followed by oscillations as the wave traveled back and forth, dissipating during the expansion stroke of the engine.

3.6.2   Ignition Delay Time Wave

The model is now used to show how certain temperature gradients do not result in coupled reaction fronts and pressure waves. A very shallow temperature gradient of -0.01 K/mm is initially present in a mixture of methane and air at 50 bar. In this case the left-hand side is at 1200 K. After an initial ignition delay time, the reaction proceeds very rapidly, producing profiles as seen in Figure 3.6. In this case, the wave progresses from left to right, but the pressure does not exceed the constant volume pressure of 132 bar by more than a few percent. This is an example of a wave that is part of the thermal explosion mode of combustion waves. There is an *apparent* wave, but the difference in ignition delay time between adjacent parcels is *so small* that there is neither time nor necessity for a pressure wave to couple and prompt further reaction. In this way, the wave is not "causal" in a sense, but just a result of the slight variation in initial temperature producing a slight variation in

---

[2]The constant-volume combustion is discussed further in Section 4.1.1
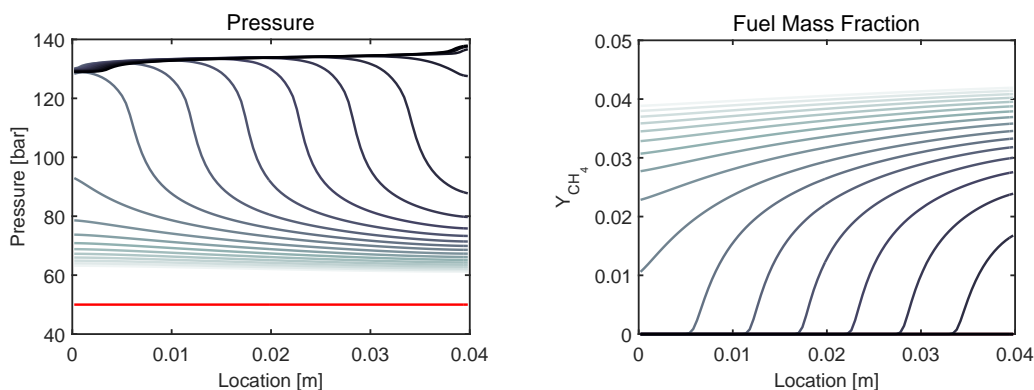
Figure 3.6: Stoichiometric methane/air at an initial pressure of 50 bar. Initial temperature of 1200 at the left with linear gradient decreasing by 0.01K/mm toward the right. Initial conditions plotted in red. All of the other plotted profiles take place between 762 μs and 770 μs at a spacing of about 0.4 μs between successive profiles.

ignition delay time. The adjacent fluid parcels happened to be arranged in order of increasing ignition delay time from left to right, which is why a wave appears. The autoignition "wave" progresses faster than the local sound speed, escaping from the gasdynamic coupling produced in the previous example. If the temperature inhomogeneity was not such that parcels of adjacent gas were ordered left-to-right from shortest-to-longest ignition delay times—as is the case in this example—the autoignition sequence would not take on the appearance of a wave.

This is further evidence that high rate of pressure rise in the cylinder is not equivalent to ringing. The lack of over-pressure or subsequent pressure oscillations in the domain in this case, despite the very rapid progression of combustion, demonstrates that it is the gasdynamic coupling thatproduces over-pressure (or pressure inequality in the cylinder), causing pressure waves which result in engine damage. High overall reaction rate is not necessarily linked to the production of pressure waves or higher-than-expected cylinder pressures which could cause structural damage. This test case is an example of very well-mixed, homogeneous combustion, and HCCI in its ideal case might be something like this.

3.6.3 Deflagration

The deflagration mode is not captured by the reacting compressible flow model, since the means of wave propagation in a deflagration is due to molecular diffusion which is not included in the model. This mode is reflected by the model in the sense that certain cases demonstrate the absence of gasdynamic coupling when temperature gradients are too steep. In this case, the pressure wave produced by the initial exothermicity gets out ahead of the reaction zone rather than coupling into the autoigniting mode, and we surmise that a deflagration would be taking place and traveling at the local flame speed for the mixture.

Depending on the temperatures and pressures of the calculation, very steep temperature gradients around 10 K/mm would not exhibit coupling because the initial dilatation is not sufficiently strong to produce coupling. The pressure wave advances ahead of the reaction wave does not exhibit the same steepness as the pressure profile of a developing detonation as it is not reinforced by a coupled chemical reaction. Some examples of this mode will be explored later in Chapter 4.

3.7 Conclusions and Future Work

The numerical model for reacting compressible flow described in this chapter has shown to be a useful tool for understanding the coupled physics of developing detonations, and will enable investigation into strategies for disrupting coupling, such as dilution or large spatial inhomogeneity. Results from the model under those conditions can be found in Chapter 4.

The agreement of the numerical model with validation cases, both analytical and with published models intended for the same type of investigation, suggests that the model presented here is capturing the important aspects of this physical phenomenon.

The model captures the effect of temperature gradients on the propagation mode of the combustion wave. A range of temperature gradients can be chosen to produce the developing detonation mode, where the gradient of ignition delay times

of adjacent packets of reactive mixture is situated such that the pressure wave arriving at a location is well-timed with combustion occurring in that packet. Further, the "ignition delay time" wave demonstrating nearly-homogeneous combustion provides insight into the previously-discussed (in Chapter 2) question of ringing versus rate of pressure rise in the cylinder. This is an excellent example of combustion which has a *very* high overall rate of pressure rise but exhibits very little pressure inequality. In the absence of pressure inequality, oscillations do not occur and the measured pressure trace is smooth. Finally, there are cases in which the temperature gradient is too steep, and it is encouraging that the model is able to capture the fact that a developing detonation does not form in this case.

For the calculations presented in this dissertation, the computations were carried out on a 4-core Intel processor. For future calculations, the model can be extended to run on computer clusters by directly implementing MPI (Message Passing Interface) into the structure of the code. This would provide gains in the speed of calculations, as in its current state most test cases require several hours to complete, using four cores. The increase in computational speed afforded by MPI would also open up the possibility to extend the code to two or three dimensions to investigate scenarios in which the problem cannot be simplified into one dimension. Further, more complicated chemical mechanisms for higher hydrocarbon fuels could be incorporated beyond the combustion of methane calculated in this work.

Finally, even beyond the extension of the code, the types of questions the model can answer cannot be fully exhausted within the scope of this dissertation. Questions relevant to the ringing phenomenon in IC engines are explored in Chapter 4 but there remain many unexplored in-cylinder conditions and possible strategies for mitigating ringing that are left to future users of this code or other similar models.

Chapter 4

Modeling Results and Discussion

This chapter presents and describes selected results from the numerical model. The model was used to demonstrate the coupling and gasdynamic impedance of developing detonations, as well as to explore cases of ringing disruption through dilution and macroscopic inhomogeneity in temperature and/or chemical species. Finally, motivation for experimental investigation is given based on model results.

The purpose of the numerical model is to compliment experimental investigation by both informing possible experimental approaches and by interpreting experimental results. Thus, some of the results selected seek to interpret previous experimentation by other researchers, while other cases seek to provide a path forward in understanding.

4.1   Baseline Case: Developing Detonation

The representative categories of autoigniting combustion modes given in Chapter 3 demonstrated how an initial temperature gradient could affect the ensuing behavior of the combustion. Too steep a gradient produces a deflagration while too shallow a gradient produces a nearly homogeneous thermal explosion. Both of these modes do not produce pressure waves, making them more benign than the developing
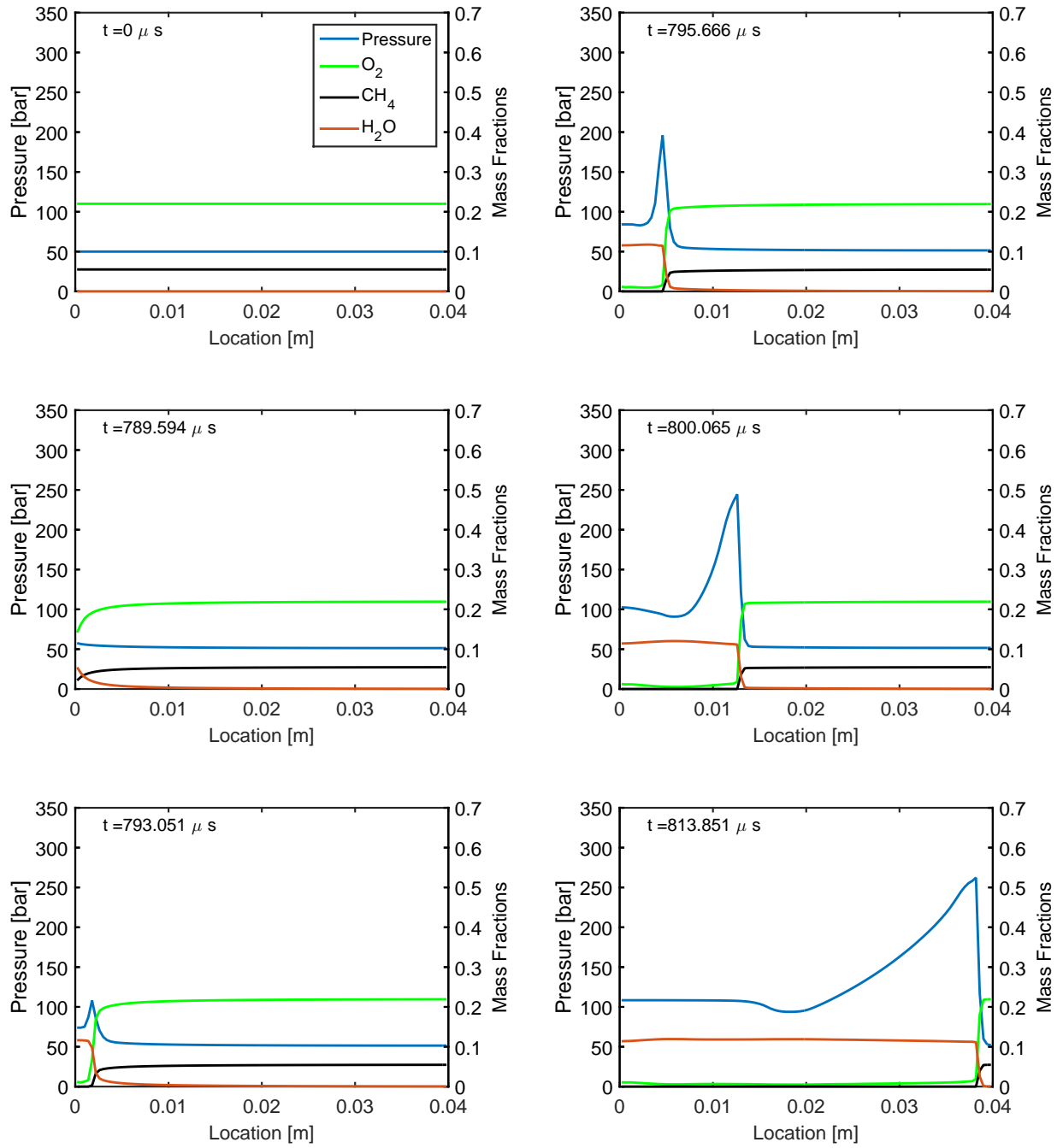
Figure 4.1: Developing detonation mode demonstrated in a methane/air mixture at unity equivalence ratio, with an initial temperature of 1200 K at the origin and a temperature gradient of -1 K/mm. The initial pressure is 50 bar.

detonation mode. The baseline case for modeling investigation into ringing disruption is the case of a developing detonation. The plots in Figure 4.1 echo the plots from Section 3.6.1, in which a methane/air mixture with an initial linear temperature gradient reacts rapidly, after its ignition delay time, to form a steep propagating pressure spike coupled with a reaction wave. The autoignition originates on the left side of the domain, at an initial temperature of 1200 K. A temperature gradient of 1 K per mm is initially present in the mixture, decreasing toward the right of the figure.

Each panel contains properties of interest plotted at a snapshot in time (displayed in the upper-left of each plot). This format, having pressure and composition variables on the same axes, makes it easy to see when a pressure wave and reaction front are co-located, and when they are not. The plots in this chapter are in Cartesian coordinates, but they can be thought of as though the left side of each plot was the centerline of the combustion chamber and the right side was the cylinder wall. The x-axis can be thought of as a line along the radius of the cylinder[1].

4.1.1 Constant-Volume Pressure

Both the deflagration and thermal explosion modes have peak pressures approximately equal to the *constant-volume pressure*. The constant-volume pressure is the pressure that a reacting mixture reaches when the reactions are taken to equilibrium in an adiabatic, isochoric environment. In the model test cases of this chapter, this represents the maximum pressure that could be reached in the absence of gasdynamic coupling or pressure waves.

In actual engine experiments, the combustion chamber is neither at constant volume nor adiabatic, but because the time scales of piston motion and heat transfer are significantly longer than the time scale of the combustion events, the

---

[1]The model is equipped to calculate results in Cartesian, cylindrical, or spherical coordinates, but the plots here are in Cartesian coordinates to facilitate ease of interpretation.

constant-volume pressure is still a relevant metric. For the duration of the autoignition sequences studied here, the piston is essentially stationary, and heat transfer processes are slow, meaning that the combustion chamber can be thought of as a constant volume, adiabatic vessel.

The constant-volume pressure gives a sense of how excessive the pressures in developing detonations often are. For example, in the developing detonation in Figure 4.1, the constant-volume pressure is 132 bar, while the maximum pressure in the plots is 262 bar and the pressure reached when the wave reflects off the wall is 511 bar. Only once the wave encounters the wall would it register on a pressure transducer in an engine experiment. The wave will oscillate back and forth until it dissipates during the expansion stroke, as can be seen in measured pressure traces. This example further demonstrates how the pressure transducers in engine experiments are not sufficient as tools to understand the gasdynamic coupling leading to ringing and engine damage. Further, the maximum rate of pressure rise metric calculated from the time derivative of a pressure signal does not shed much light onto this type of combustion.

4.2 Effects of Temperature Variation on Developing Detonation

A starting point for modeling investigation is to look beyond the linearly varying temperature profiles used to demonstrate the three combustion modes. In an actual engine, temperature gradients are unlikely to be linear. As mentioned previously, the water injection in Svrcek's experiment may have introduced a macroscopic[2] inhomogeneity that suppressed ringing. The evaporation of liquid water could have depressed the temperature in the center of the cylinder, and heat transfer to the walls would lower the temperature along the outer edges of the cylinder. Various

---

[2]Macroscopic meaning larger in length scale than the size of typical inhomogeneities in IC engines, which are on the order of the turbulent integral length scale.

temperature profiles were tested that might be more representative of the temperature gradients arising in an IC engine with centralized water injection.

Figure 4.2 shows results from one of the model cases exploring the effect of a macroscopic inhomogeneity in temperature. In this case the temperature profile is created using a beta-function, so that the width and horizontal position of the peak can be adjusted to approximate a temperature depression at the cylinder's center and walls.

In Figure 4.2, there is definite coupling between the pressure inequality produced by the initial exothermic reactions at the temperature peak location, and the subsequent reactions of the adjacent gas. The pressure spike builds in a similar manner to the developing detonation baseline case. The constant-volume combustion pressure in this case is 130 bar. Again we see that it is possible, through coupling of pressure waves and reaction fronts, to create pressures higher than the constant-volume combustion pressure.

A number of other beta-distribution and sinusoidal temperature profiles were evaluated with the numerical model, but they all exhibited similar results. None provided much insight into practical temperature profiles that could disrupt the coupling. One reason that the temperature profiles tested did not disrupt the coupling under these conditions is the broad range of temperature gradients that lead to coupling in strong mixtures, such as stoichiometric methane and air. Referring back to Figure 2.12, the conditions explored here would fall far to the right on the ϵ axis, where the developing detonation region is very broad.

Temperature profiles are an important indicator of whether coupling will occur during combustion, but the model shows that temperature variation alone is likely not sufficient to prevent developing detonations in actual engines. The range of temperature gradients leading to coupling is very broad for stoichiometric air/fuel mixtures, so that only unrealistically steep gradients or unrealistically homogeneous mixtures (like those discussed in Section 3.6.2 and Section 3.6.3) would resist coupling. Thus, temperature variation was not the major reason that water
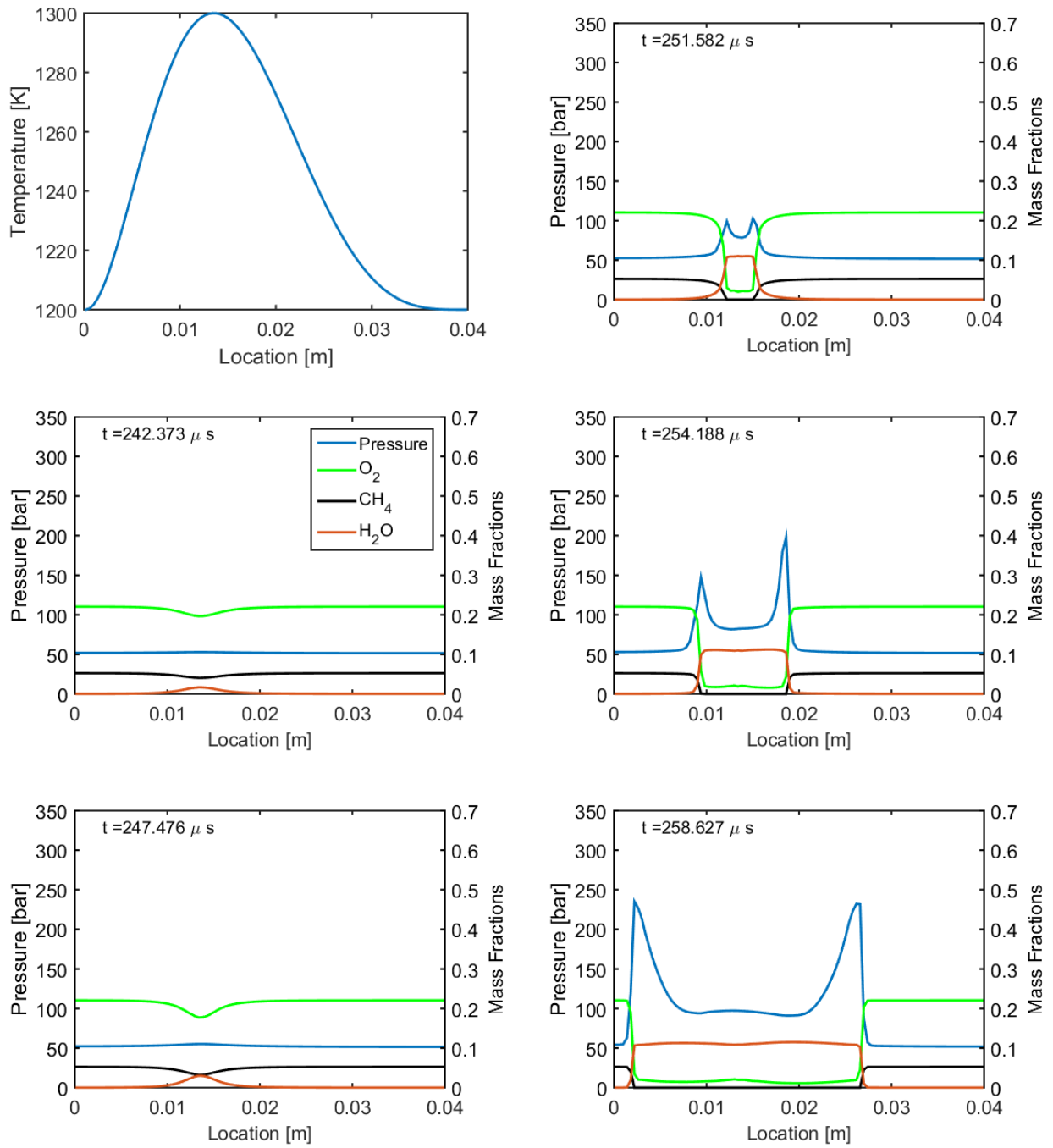
Figure 4.2: A methane/air mixture at 0.95 equivalence ratio having an initial macroscopic temperature inhomogeneity, as plotted in the first panel. The initial mixture pressure is 50 bar.

injection was successful at disrupting ringing. Beyond temperature effects, variations in composition might also have arisen during the water injection, so the next set of conditions to consider is the effect of chemical composition on the formation of developing detonations.

4.3 Effects of Chemical Composition on Developing Detonation

The numerical modeling results to this point have examined the role of an initial temperature gradient in gasdynamic coupling. Linear gradients and curved gradients were explored, but the composition remained uniform throughout the domain, stoichiometric[3] methane and air.

Before considering spatial inhomogeneities in composition, such as would likely arise during water injection in an engine, it is useful to understand the effects of homogeneous dilution with a moderator. Comparison of the amount of moderator introduced into the mixture, whether the moderator is monatomic or diatomic, and whether it participates in the chemical reaction are considered. For the following cases to remain consistent, the initial pressure and initial temperature gradient were the same in each case. It is important to remember that in a real engine charge dilution would decrease engine load, but for the sake of understanding gasdynamic coupling and ringing, the initial temperature and pressure are kept constant.

4.3.1 Equivalence Ratio Variation

An easily-implemented dilution strategy in an engine is to operate the engine at a fuel-lean equivalence ratio, diluting with excess air. Air is primarily composed of nitrogen and oxygen. The following examples illustrate different trends in the

---

[3]Or 0.95 equivalence ratio in a few cases, for reasons of convergence with chemical kinetic computations.

way autoignition begins and progresses as a result of increasing the excess air while maintaining otherwise-identical initial conditions.

The first illustrative case is diluting the methane and air mixture with 20 percent excess air. The mixture is equivalence ratio 0.8 methane and air at an initial pressure of 50 bar and an initial temperature of 1200 K at the left side, decreasing by 1 Kelvin per millimeter towards the right.

The equivalence ratio 0.8 case looks similar to the stoichiometric case. The mixture exhibits coupling almost immediately after the reactions begin, and the developing detonation grows as it travels through the air/fuel mixture. Twenty percent excess air is not enough to disrupt the gasdynamic coupling at the onset of autoignition at the left.

Figure 4.4 contains modeling results of methane/air at an equivalence ratio of 0.7. The beginning of the autoignition process here differs from the equivalence ratio 0.8 case in that the pressure wave initially leads the reaction front by a slight amount. After briefly lagging, the reaction front catches up to the pressure wave, producing a strong pressure peak and commencing coupling between the reaction front and pressure wave that continues through the rest of the air/fuel mixture as a developing detonation. The additional ten percent air dilution caused a slightly delayed coupling compared to the equivalence ratio 0.8 case, but in the end a developing detonation still formed.

In the case of methane and air at 0.5 equivalence ratio, shown in Figure 4.5, the pressure wave and reaction front do not initially couple. Instead, the pressure wave moves out ahead of the reaction front. However, after the pressure wave reflects off the wall it passes through the reaction front. Just to the right of the reaction front is a region of air and fuel which is very close to the point of autoignition. This region has a temperature gradient suitable for gasdynamic coupling, but the negative temperature gradient is toward the right, while the reflected wave is traveling to the left. As seen in the plots, the reflected wave provides enough compression to cause this region to ignite, couple, and launch a wave back at the wall to the right.
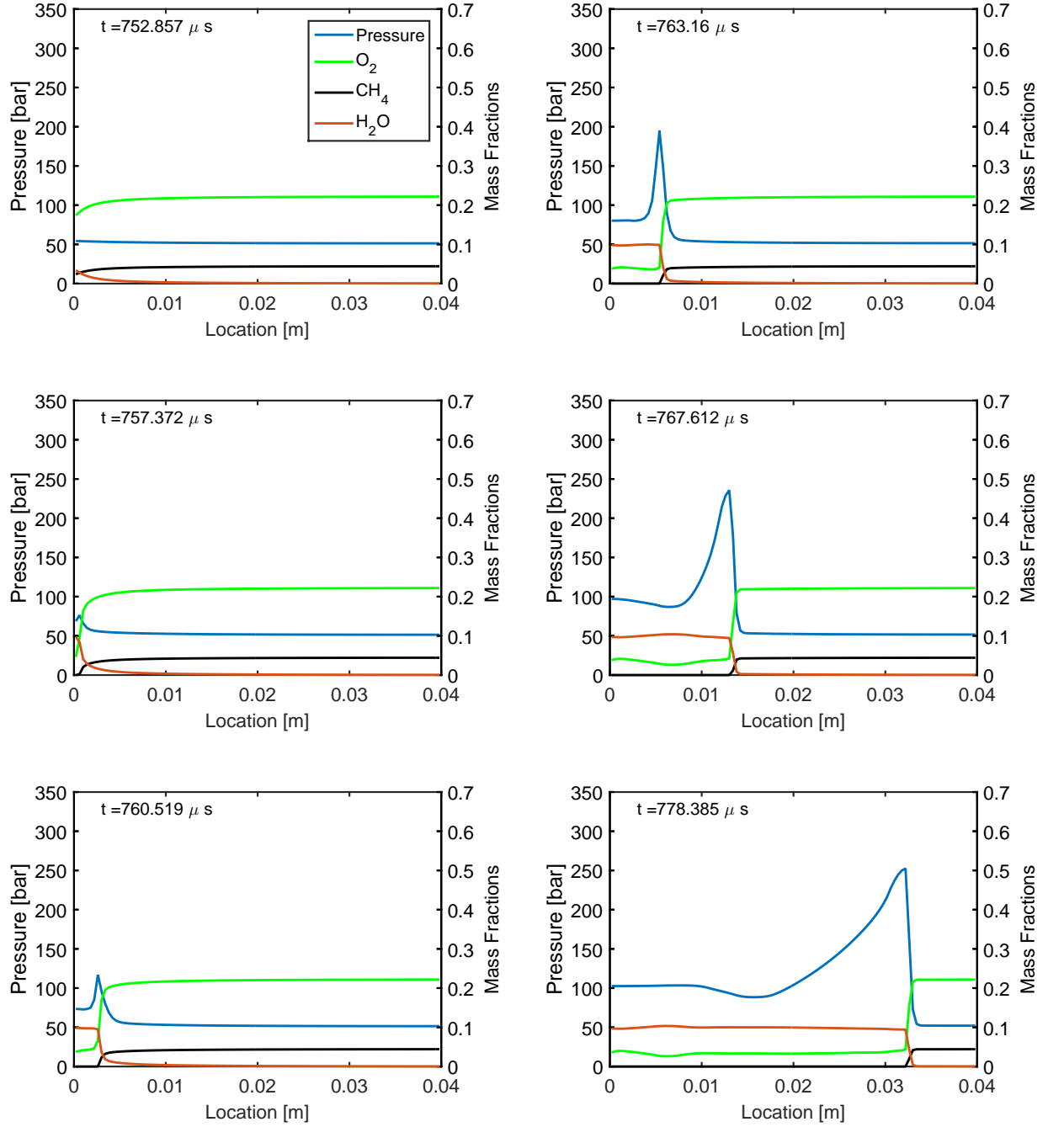
Figure 4.3: Methane/air mixture at an equivalence ratio of 0.8 with an initial temperature of 1200K at the origin and a temperature gradient of -1K/mm. The initial pressure is 50 bar.
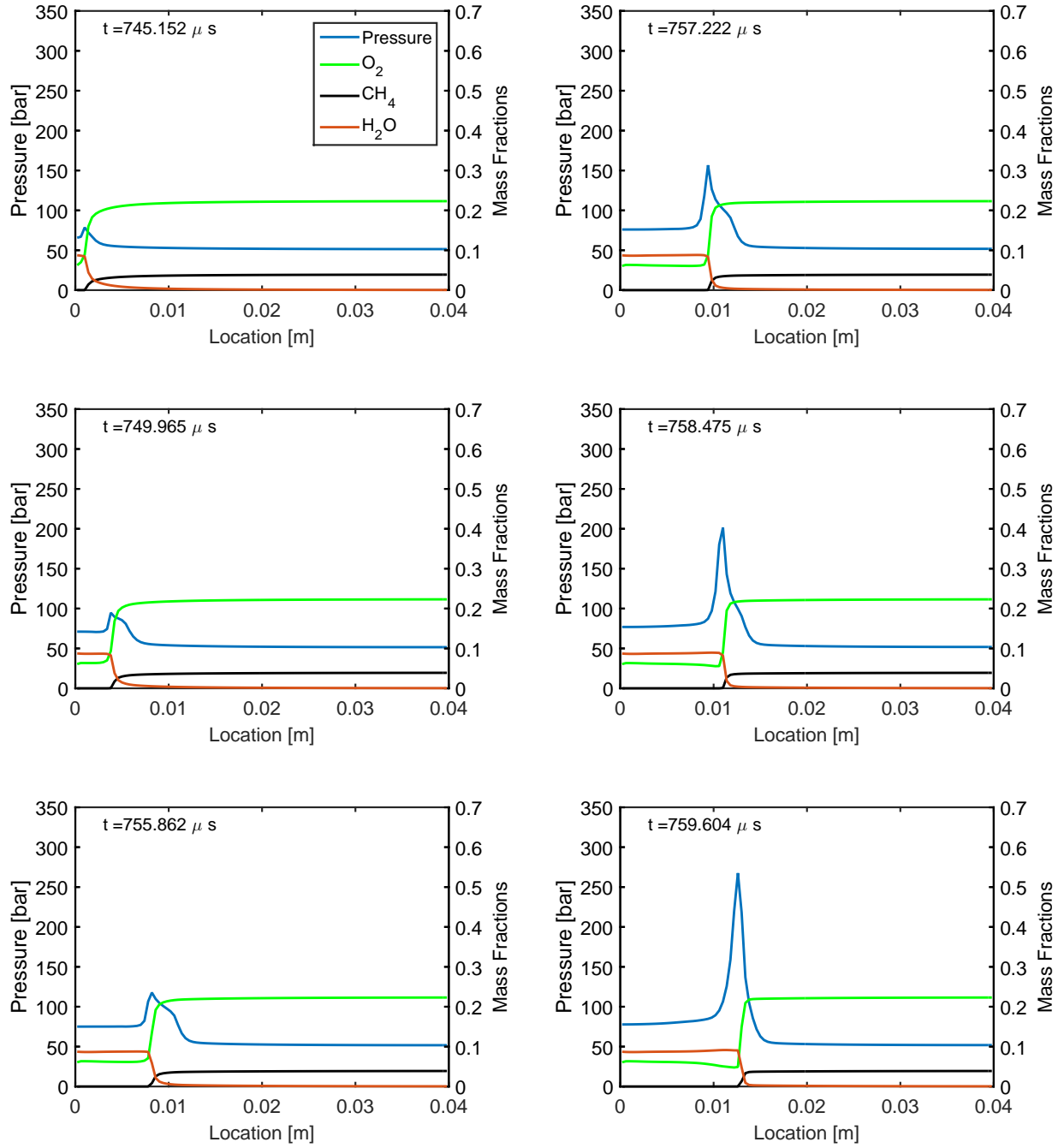
Figure 4.4: Methane/air mixture at an equivalence ratio of 0.7 with an initial temperature of 1200K at the origin and a temperature gradient of -1K/mm. The initial pressure is 50 bar.
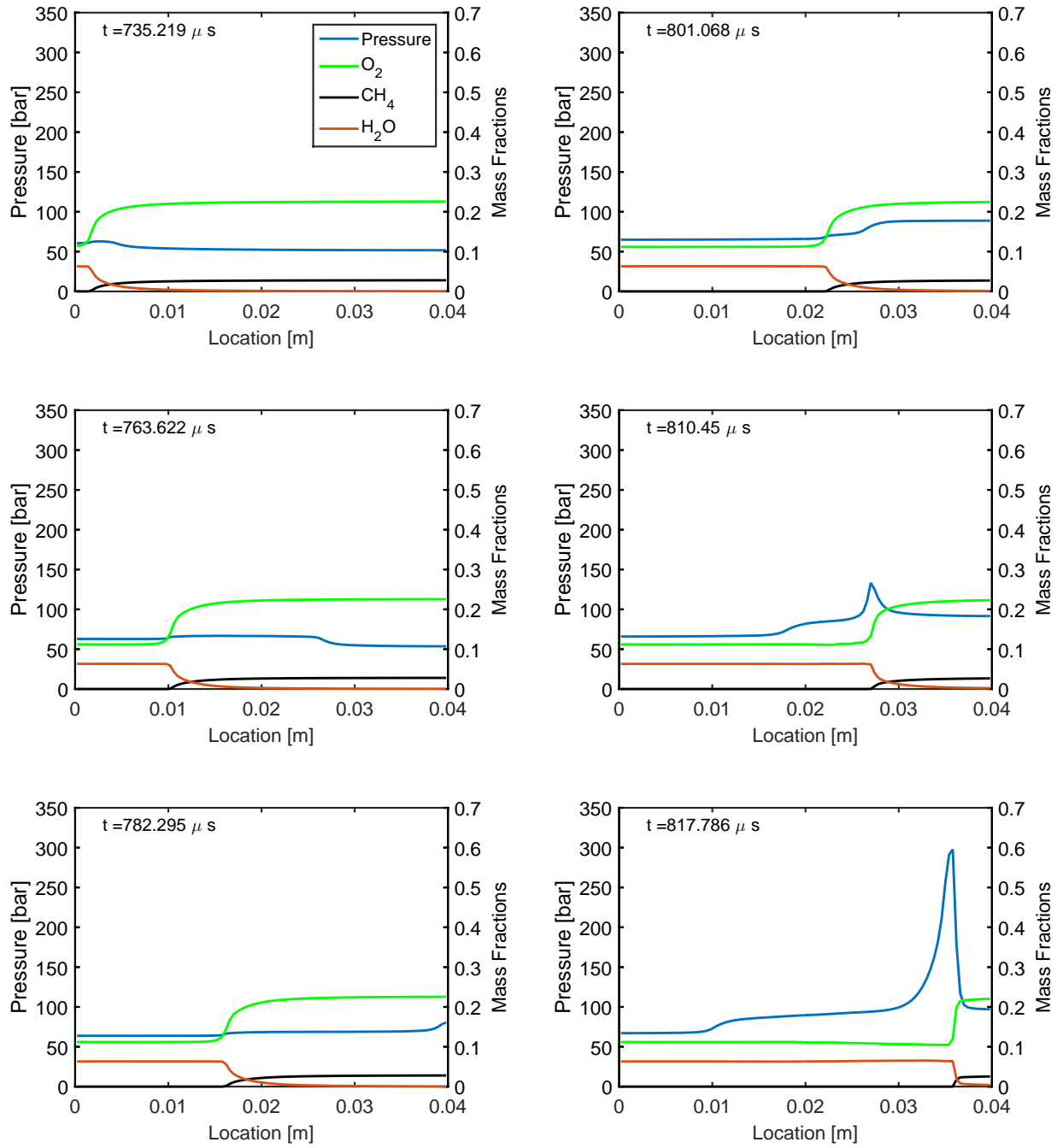
Figure 4.5: Methane/air mixture at an equivalence ratio of 0.5 with an initial temperature of 1200 K at the origin and a gradient of -1K/mm. The initial pressure is 50 bar.

The autoigniting front, initially de-coupled from the pressure wave, is propagating due to sequential autoignition of neighboring regions of air and fuel mixture. This autoigniting front produces a developing detonation when subjected to the reflected pressure wave. This is likely because the reflected pressure wave raised several adjacent regions of gases near their autoignition points to a higher temperature, prompting a larger and more simultaneous exothermic reaction among these adjacent regions than would have taken place in the absence of this energy input. This larger region undergoing a more simultaneous exothermic reaction produced a sufficiently strong dilatation to encounter gasdynamic impedance and produce a pressure spike coupled to a reaction wave. The dilatation expanding toward the right encountered un-reacted air and fuel, initiating a developing detonation, while as it expanded toward the left it proceeded as a pressure wave through combustion products.

This result is interesting because it demonstrates that even if the origin of combustion is someplace other than the location of a favorable temperature gradient for coupling, weaker acoustic waves from neighboring combustion events are capable of initiating the coupling process. It's also interesting and not entirely obvious that regardless of the direction of the incoming triggering wave pulse, the new coupled reaction wave travels in the direction toward the negative temperature gradient (and through the region of unburned air and fuel). This has ramifications for understanding these waves in practical HCCI engine situations, where the temperature gradient that produces a developing detonation might not be at the location of the hottest or first-to-ignite gases. In these cases gasdynamic coupling can still begin at a secondary location partway through the combustion process, being triggered by the waves emanating from any other region of the cylinder.

When the model was used to explore mixtures leaner than equivalence ratio 0.5, the coupling does not arise. There are still pressure waves emanating from autoigniting portions of the mixture, but they are low-amplitude and their appearance is not sharp, much like the first few panels of the equivalence ratio 0.5

case. The pressure rise is gradual throughout the domain, reaching the constant-volume pressure once all of the fuel has reacted.

When an air/fuel mixture is diluted with excess air, competing effects are likely at work with regard to gasdynamic coupling. Both oxygen and nitrogen will have a thermal moderating effect. The nitrogen is likely energetically unimportant in the chemical reaction sequence, while the presence of additional oxygen may play a role in making the mixture more prone to coupling. To separate these chemical and thermal moderating effects, dilution with an inert moderator is considered next.

4.3.2 Dilution with Nitrogen

The exhaust from stoichiometric combustion, a mixture of nitrogen, carbon dioxide, and water, is often used to dilute the air/fuel mixture in internal combustion engines to suppress autoignition. Exhaust gas is composed primarily of nitrogen, and is considered an inert moderating mixture. In the following example, the effect of dilution with pure nitrogen is considered.

In Figure 4.6 we see results from a stoichiometric mixture of methane and air with an additional 20 percent nitrogen by mole. Like the three fuel-lean cases in the previous section, there is a linear temperature gradient starting at 1200 K at the left side, decreasing linearly at 1 K/mm. The initial mixture pressure is 50 bar.

The behavior of the autoigniting mixture diluted with 20% nitrogen bears resemblance to the equivalence ratio 0.5 case. The initial coupling of pressure wave and reaction front does not take place, but the wave by the wall provides enough input energy to cause a developing detonation to form. It took only 20% nitrogen dilution to achieve behavior similar to 100% excess air (0.5 equivalence ratio). Oxygen and nitrogen, being diatomic, both have similar capacity to act as thermal moderators. For example, the exit temperature of a constant-pressure combustor whose input is a mixture of methane and air with 20 percent nitrogen dilution is very similar to the exit temperature of a reactor fed with an equivalence ratio 0.8 mixture. On the other hand, an equivalence ratio 0.5 mixture has a much lower
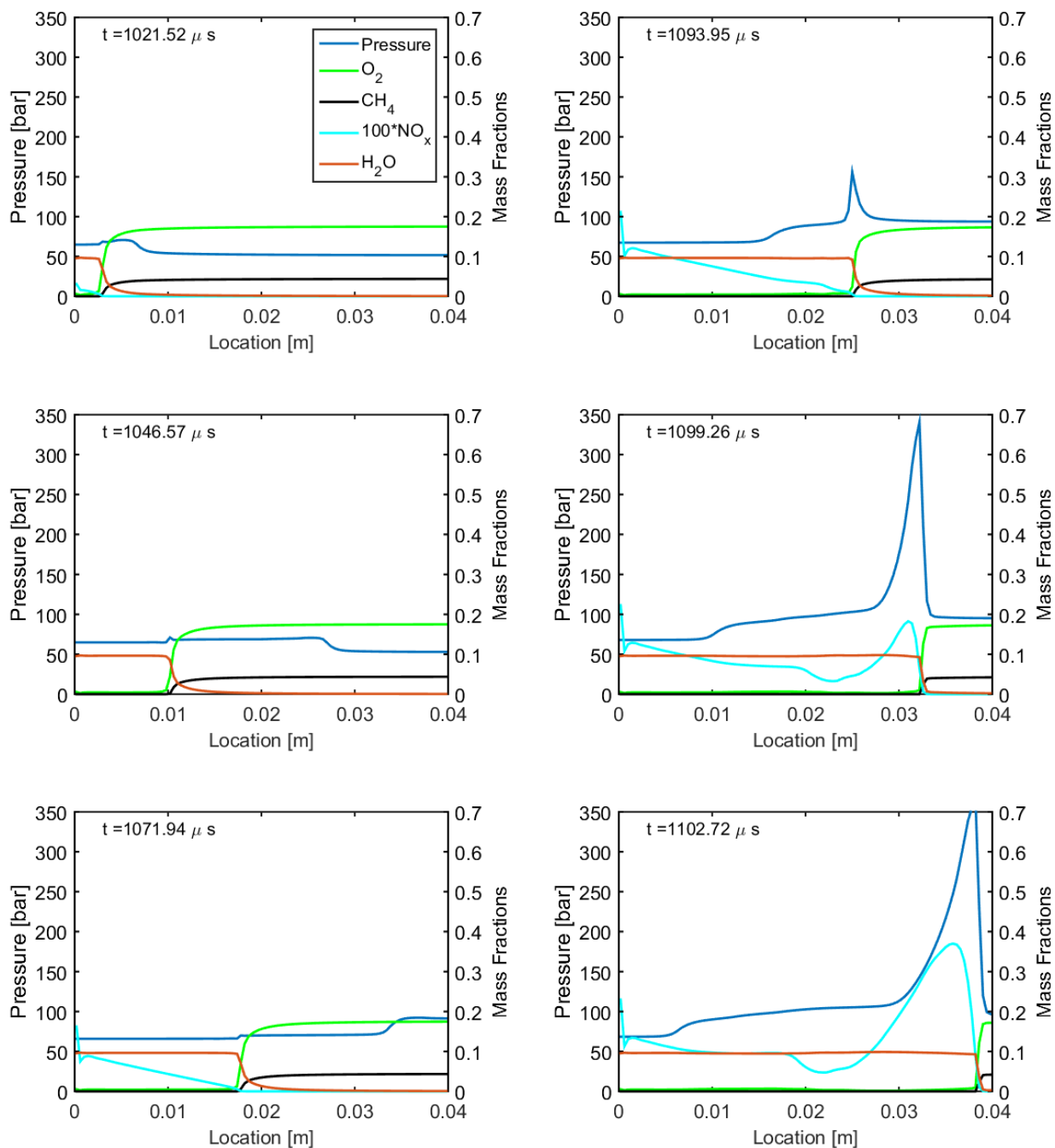
Figure 4.6: Stoichiometric methane/air diluted with 20 percent nitrogen by mole. The initial temperature is 1200 K at the origin, with a gradient of -1 K/mm. The initial pressure is 50 bar. The mass fraction of NO_x is plotted as well, to examine its role in gasdynamic coupling, as discussed in Section 4.3.4.

post-reactor temperature than either. However, the gasdynamic coupling behavior of the 0.5 equivalence ratio mixture is more similar to the 20 percent nitrogen dilution, while the equivalence ratio 0.8 mixture very readily couples. In more simplistic terms, the gasdynamic coupling behavior is much more sensitive to oxygen concentration than nitrogen concentration. This result indicates that there is more to moderating developing detonations than the thermal capacity of a moderating gas, and that the chemical participation of moderating species has a significant influence on the autoignition behavior.

4.3.3 Dilution with Argon

Even among inert moderating species, there are multiple effects to consider. The presence of an inert moderator will reduce the likelihood of an oxygen and fuel molecule colliding with each-other for hydrogen abstraction initiation reactions (since they'll sometimes collide with an inert molecule). The second is a thermal moderating effect, as discussed in the last section. The effectiveness of an inert moderator for this purpose will depend on its specific heat. To separate these two effects (reducing collision frequency of air/fuel vs. thermal capacity), dilution with argon is considered in comparison to nitrogen dilution. Argon is a monatomic inert gas. It has a lower specific heat, but it will similarly reduce collision frequency of air and fuel. In Figure 4.7 the results of dilution with 20 percent argon are shown.

The argon shows a slight delay in the initial coupling as compared to the non-diluted stoichiometric case, but it does not interrupt the coupling entirely. The reaction front catches up to the pressure wave, at which point the two waves coalesce to form a coherent pressure spike as seen before. This is a more pronounced, but similar, delayed coupling behavior to the equivalence ratio 0.7 case.

Argon dilution at 20% by mole behaves like an equivalence ratio of 0.7, while nitrogen dilution at 20% by mole behaves more like an equivalence ratio of 0.5. This indicates that the specific heat of the diluting species plays an important role in preventing gasdynamic coupling. Dilution with excess air reduces coupling, but it
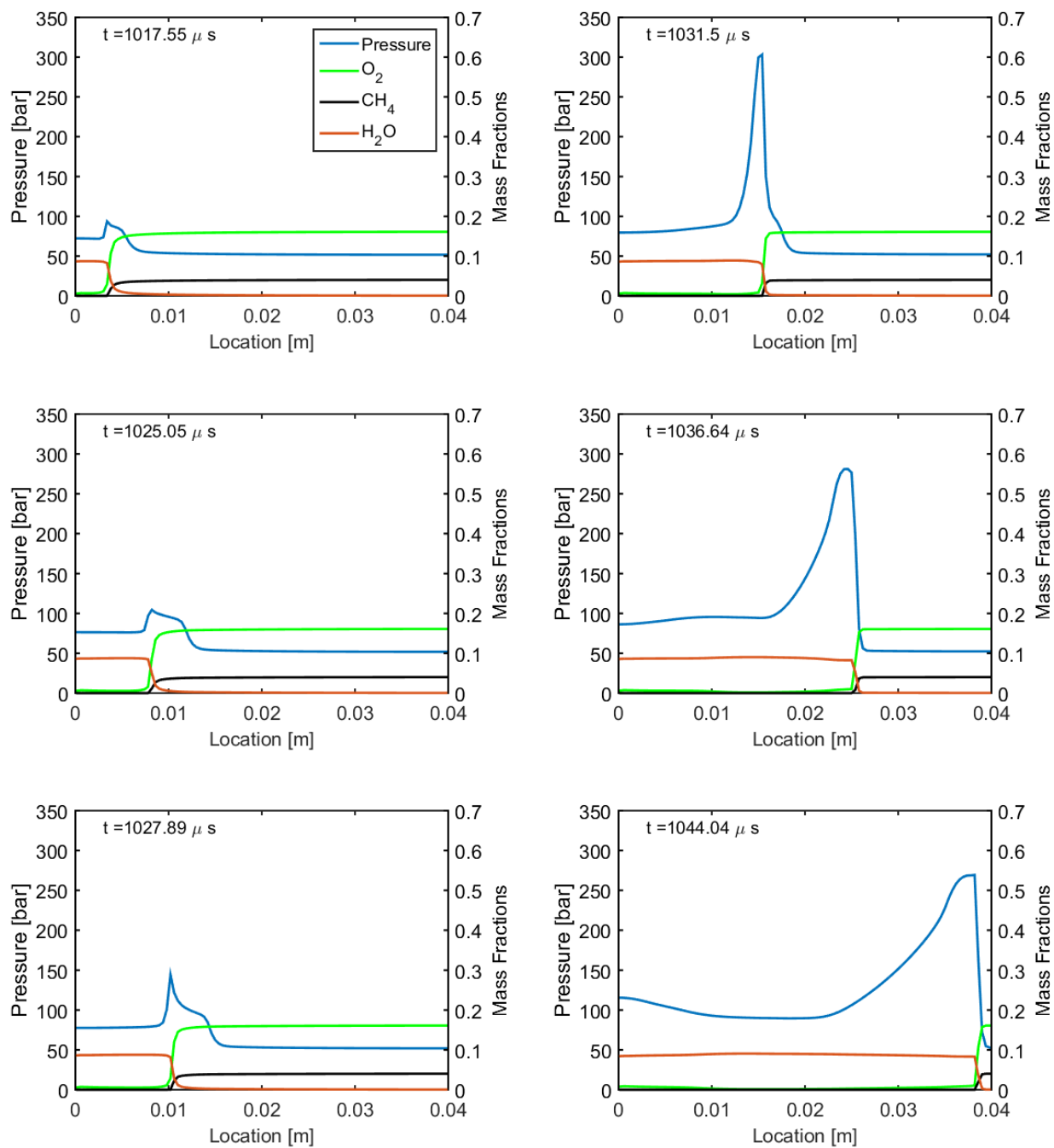
Figure 4.7: Stoichiometric methane/air diluted with 20 percent argon by mole. The initial temperature is 1200 K at the origin with a gradient of -1 K/mm. The initial pressure is 50 bar.

is not as effective as an inert gas like argon, which is not as effective as a higher heat capacity gas like nitrogen. Twenty percent excess air did very little to disrupt coupling, while twenty percent argon delayed coupling. Twenty percent dilution with nitrogen delayed coupling most effectively, but a reflected pressure wave still produced a developing detonation in the last portion of unburned air and fuel.

4.3.4 Effects of NO_x on Dilution

One of the major assumptions in expressing the nitrogen and argon dilution cases as a comparison of monatomic vs. diatomic moderators is the assumption that they are inert. However, the post-combustion temperature is sufficiently high to form NO, which can serve as a promoter in chemical reactions. To facilitate thinking about the role of NO in the coupling, its mass fraction is plotted in Figure 4.6 alongside the pressure and other species variables. The NO_x visibly increases with time in the hot post-combustion gases behind the wave (as evidenced by increasing NO_x with distance behind the reaction wave).

The role of NO_x in either reinforcing or preventing the gasdynamic coupling is unclear from the plots. However, there are a few effects that might be at work. In a stoichiometric air/fuel mixture, the NO_x formation reaction pathways compete with the fuel oxidation pathways for oxygen atoms. In this way, NO_x formation could be robbing a small amount of exothermicity from the reaction zone. The pressure wave is largely responsible for the propagation of the reaction front once the two are coupled, raising the gases to a high temperature and prompting initiation of the reaction. It is not clear whether the formation of NO_x behind the pressure wave initially competes for oxygen and works to prevent rapid dilatation leading to coupling, or whether it acts as a promoter in creating a more rapid dilatation.

Whether or not NO_x significantly encourages or discourages coupling, nitrogen proved to be the most effective of moderators examined. Recall that dilution reduces the power density of an engine, which is undesirable in the pursuit of highly efficient transportation systems. The levels of dilution with air, nitrogen, and argon that

are required to prevent ringing are high enough to have a significant impact on an engine's peak load. In all of these examples, the initial chemical composition has been uniform throughout the domain. In the following section, the effect of inhomogeneity in chemical composition is explored as a potential avenue to disrupt ringing with less of an adverse effect on the engine's load capacity.

4.4   Composition Inhomogeneity

Based on the injector geometry used during the water-injected experiments of Svrcek, it is probable that the water remained concentrated in the center of the cylinder.[4] This would have created a macroscopic inhomogeneity in chemical species, as well as in temperature (based on evaporative cooling). The effect of spatial variations in composition is explored in this section through cases where water is a non-uniformly-distributed species.

4.4.1   Water Injection Approximation

In Figure 4.8 results are plotted from initial conditions approximating central water injection. The mole fraction of water varies according to a sinusoidal profile and the temperature also varies through the domain to simulate regions with more water having experienced more evaporative cooling.[5] The temperature is also lower near the cylinder wall as it would be due to heat transfer. The concentration of water is greatest near the centerline (left side of plot) and lower at the outside edge of the combustion chamber (right side of plot). The overall water mass fraction is 10%.

Despite the presence of water, the plots in Figure 4.8 are similar to those in Figure 4.2. Coupling occurs after initial exothermicity at the warmest part of the

---

[4]He used a single-hole "pencil injector" located along the central cylinder axis to inject the water

[5]The temperature and water mole fraction profiles are not directly linked—they are both postulated as having the type of shape one would expect to see in a water-injected engine. The temperature profile does reflect the magnitude of temperature depression expected from the amount of water injected.
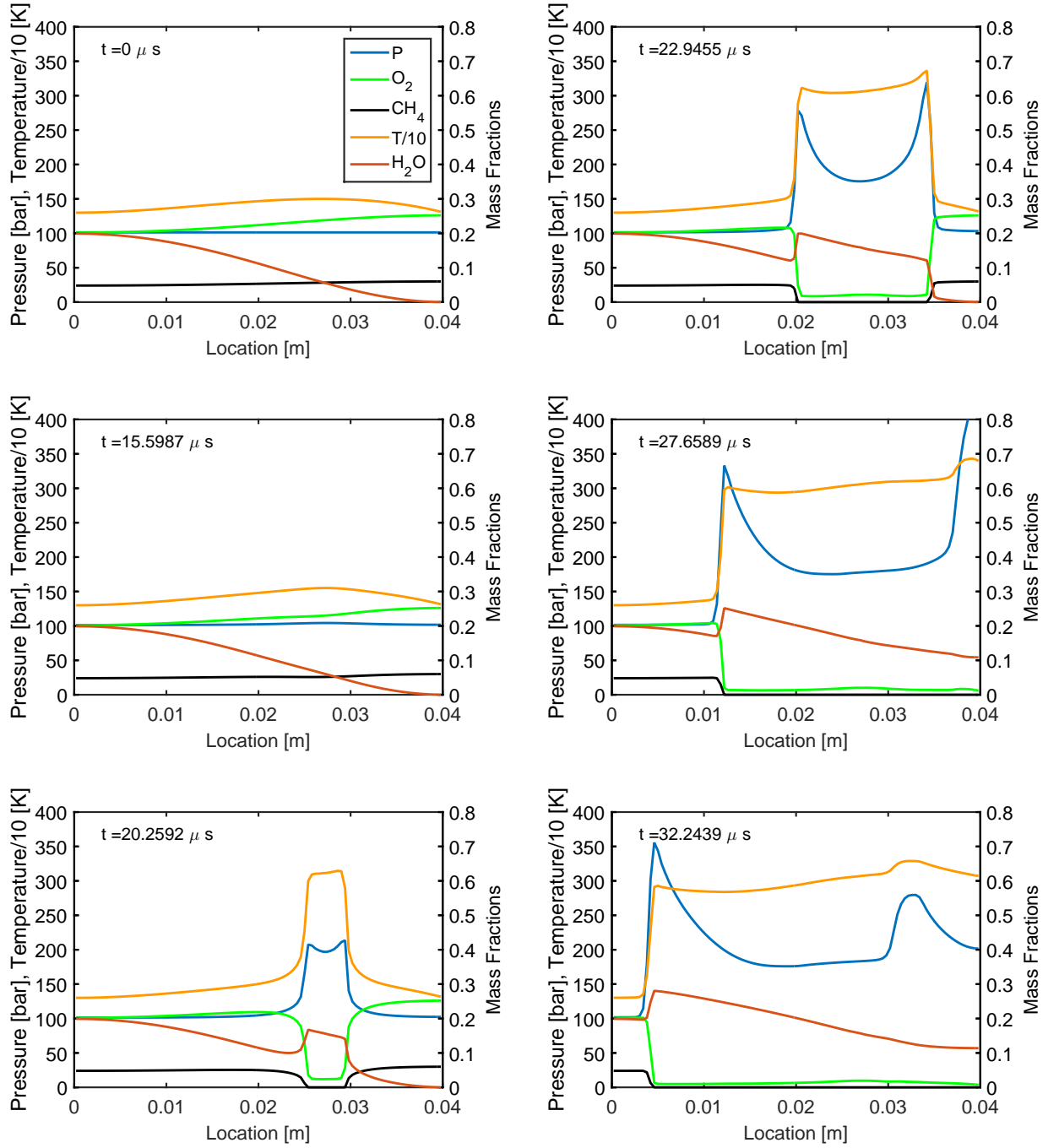
Figure 4.8: Methane/air mixture at 0.95 equivalence ratio with macroscopic inhomogeneity in temperature and water mole fraction. Initially, water comprises 10% of the mixture by mass and the initial pressure is 100 bar.

domain, and developing detonations travel outward in both directions. The water has surprisingly little effect on the coupling, given the experimental success observed by Svrcek using 8% water by mass. In order to understand further how inhomogeneity in composition might affect coupling, a case with a higher mass fraction of water injected is explored next.

Figure 4.9 displays the results of a case with increased water injection (34%) compared to the previous case. Here too, the autoignition begins at the point of highest temperature, and goes on to produce a developing detonation in both directions. However, as the wave travels leftward encountering an increasing water mole fraction, the reaction front begins to lag behind the pressure wave. Without the coupling to reinforce it, the shape of the pressure wave becomes more rounded.

The height of the left-propagating pressure pulse is not much higher than the constant-volume combustion pressure, which for this case is 200 bar. Despite the decoupling, however, 34% water does not seem to have as drastic an effect as might be expected based on the experimental data. A pressure transducer in the right "wall" of the plots would have registered sizeable ringing pressure waves.

Cases were modeled up to 91% percent water using similar sinusoidal distributions. The model predicted that far more water was required to prevent coupling than was seen in the experiment. Further investigation is needed to determine the experimental in-cylinder conditions that enabled minimally-dilute autoignition to proceed without ringing.

4.4.2   Wall of Water Example

The previous examples sought to replicate experimental conditions by approximating centralized water injection into the mixture. The gradually-varying water concentration did not have a strong impact on de-coupling the developing detonation and weakening the pressure wave. In this section, an extreme case of non-uniform dilution with a moderator is explored to show that even if coupling occurs, it is possible for a region with far more water than fuel or oxidizer to very
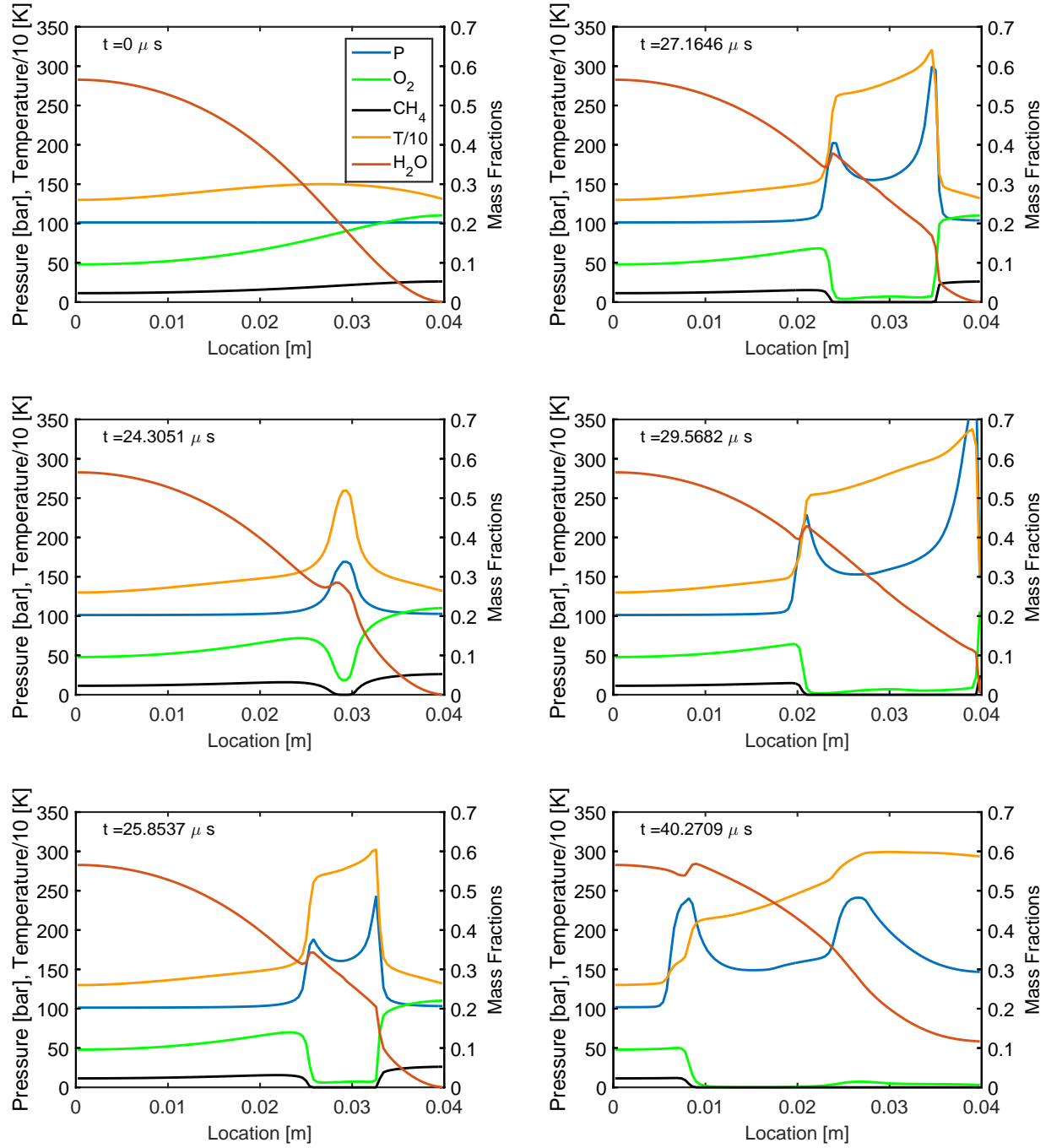
Figure 4.9: Methane/air mixture at 0.95 equivalence ratio with macroscopic inhomogeneity in temperature and water mole fraction. Water totals 34% by mass and the initial pressure is 100 bar.

rapidly diminish pressure waves.

The left side of the domain in Figure 4.10 is comprised of stoichiometric methane/air mixture with the same initial pressure and temperature gradient as the base case. The right is comprised of pure water. It is possible that the water injection performed by Svrcek remained so stratified that it displaced almost all air and fuel from the center of the combustion chamber. This case is intended to explore what happens when a developing detonation meets a large concentration of water. The reaction wave ceases, as the wave propagates into a region without air or fuel, and the pressure wave is attenuated. It could be just as useful in preventing engine damage to de-couple a developing detonation as to prevent it coupling in the first place.

The water certainly has a significant effect in this case, lowering the amplitude of the pressure wave and making it more rounded. It seems unlikely that a region of near-pure water in an engine would be sufficiently enough to fully attenuate the waves, since it takes almost as much space to dissipate the wave in the water as it took to form it in the air/fuel mixture. This case also represents an impractical amount of water dilution for achieving high load in an actual engine. However, Svrcek only injected 8 percent water by mass; It has been experimentally shown that water injection can disrupt ringing with far less water than the model indicates is required.

4.5   Modeling Conclusions

The numerical model does not predict the experimental result obtained by Svrcek, but it does provide a much clearer idea of what the contributions and competing effects are that lead to gasdynamic coupling. The intention of the model is to be instructive rather than predictive, and it has done that. The effects of different temperature gradients and different amounts of various diluting species were examined. Conclusions from the modeling results can be summed up as:
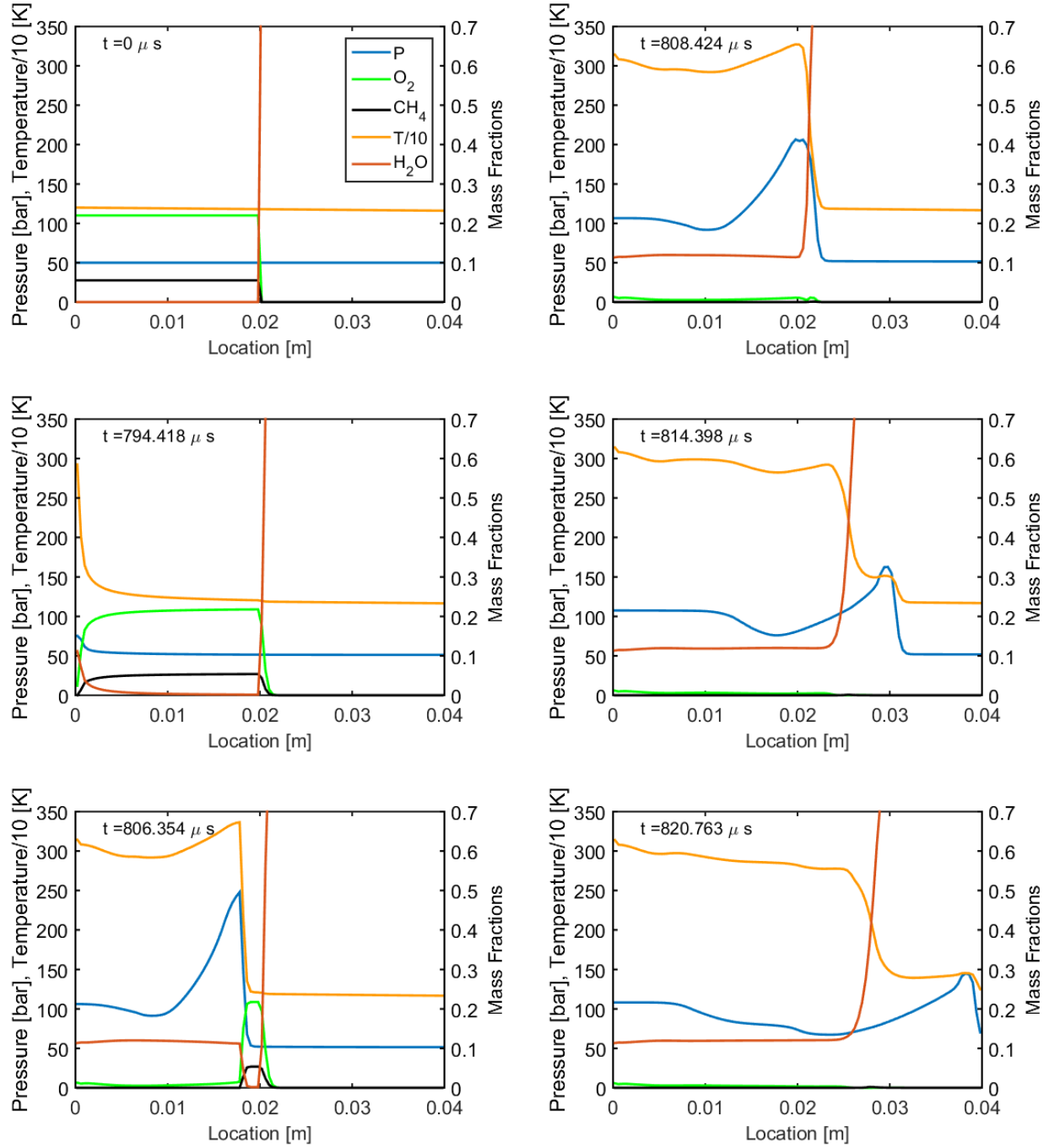
Figure 4.10: The left half of the domain is a stoichiometric methane/air mixture. The right half is pure water. The Initial pressure is 50 bar, and the initial temperature is 1200 K at the origin with a gradient of - 1 K/mm.

1. The steepest temperature gradients and shallowest temperature gradients lead to deflagration and thermal explosion modes, respectively, while a middle range of temperature gradients produces the coupling behavior of a developing detonation.

2. The range of temperature gradients leading to developing detonation is larger for mixtures with less dilution.

3. Dilution with excess air is less effective at preventing coupling than dilution with an inert moderator.

4. Among inert moderators, one having a higher specific heat is more effective at preventing coupling than one having a lower specific heat.

5. The numerical model predicts that much more water is required to disrupt ringing than was demonstrated experimentally.

The gasdynamic coupling behavior resulting from water injection is not completely understood in the simplified, 1D geometry studied here. It does not predict previously-obtained experimental results. However, the model provides an appreciation of the complexity of factors and the relative trends of these factors that contribute to the occurrence of developing detonations.

The questions remaining after modeling the gasdynamic coupling provide additional motivation for experimental investigation into this phenomenon. In an engine experiment, contributions from diffusion, turbulence, etc., can be captured. Cases such as centralized water injection can be re-created in an experimental environment amenable to observing the coupling and ensuing combustion behavior.

Chapter 5

Optical Access Design and Manufacture

This chapter describes the engineering design, manufacture, and assembly of a high-pressure optical-access engine suitable for studying high-load combustion events. It is through experimental investigation and imaging that the combustion dynamics of pressure wave formation and disruption can be best understood. A low-pressure, single-cylinder engine in the Advanced Energy Systems Laboratory at Stanford University has been re-designed to enable imaging of high-pressure phenomena. The engine in this high-pressure configuration suitable for combustion visualization is named Iris.

5.1   Engine Experiment Requirements

To begin, it is useful to consider the goals and requirements of an experiment to study pressure waves in engines. The most important of these is to gather useful information about the spatial and temporal progress of combustion. As stated previously, data from a single pressure transducer, or even multiple transducers, is insufficient to understand the gasdynamic coupling and ensuing pressure wave

behavior that is present in ringing combustion. Thus, an alternative (or rather a supplement) to the pressure transducer is needed. Non-invasive measurement techniques, such as high-speed imaging, can be used to study combustion events that take place away from the cylinder walls—such as developing detonations. Imaging is a powerful tool as it provides the spatial information that is needed to understand the developing detonation process.

There have been several studies of this phenomenon in optical access engines at low pressure (40-60 bar peak pressure) but high-pressure, in-cylinder images and experimental data are lacking [54, 55, 56]. It has not previously been possible to experimentally investigate how a large-scale inhomogeneity, such as the centralized water injection used by Svrcek, affects the progress of high-load premixed combustion.

In order to realize these experimental capabilities, certain attributes of a high-pressure optical access engine are desired:

1. the ability to operate at sufficiently high pressure to study the combustion events of interest—the design pressure goal is 250 bar,

2. the ability to see as much of the combustion chamber as possible, in the primary directions that combustion waves travel,

3. an experiment that behaves as much like a conventional engine as possible, to gain insight into the behavior of these events in non-optical, production engines, and

4. the ability to use "pass-through" imaging techniques, like Schlieren, shadowgraph, or interferometry, that allow for additional information, such as density gradients in the gas mixture, to be gathered in addition to capturing luminosity from the combustion process.

Other desirable experimental capabilities include:

5. integration of variable valve timing,

6. the ability to set an operating temperature of the cylinder head independently from the cylinder walls,

7. the ability to operate at high engine speed,

8. the ability to measure all of the quantities of interest for engine experiments, such as brake torque, intake air flow-rate, exhaust temperature, etc., and

9. integration of multiple pressure transducers into the combustion chamber design to so that wave arrivals in images can be corroborated with pressure data.

Finally, consideration was given to creating a high-pressure optical engine suitable for study of high-pressure combustion events beyond the scope of this thesis, including diesel combustion and stratified-charge SI combustion.

5.2 Types of Optical Engine Experiments

This section will briefly describe a few categories of combustion imaging experiments relevant to the current work, and the types of imaging afforded. This background information, as well as the pros and cons of various techniques, will help to explain choices made in the design of the current engine experiment.

Combustion bombs and rapid compression machines have long been used to allow combustion to be visualized and studied with optical techniques. These machines are useful for imaging the dynamics of reacting fuel sprays, flame propagation, etc. [57, 58]. The data obtained from these experiments are valuable for fundamental understanding of combustion processes, but the experimental setting usually does not resemble the combustion application.

Optical access in piston engines allows combustion phenomena to be studied in a setting similar to the intended application of those processes: flame propagation in an SI engine or diesel injection in a CI engine. Examples of optical access in piston

engines include endoscope access [59, 60], optical fibers [61, 56], and windows placed in various locations in the engine. Endoscopes and optical fibers both obtain visual information in the combustion chamber through small transparent ports installed in the engine, which can be designed to withstand high pressure. Endoscope access and optical fibers can be used in high-pressure engine applications to extract information such as the light emitted along a certain line in the cylinder, but they are limited in their ability to provide detailed spatial information about the progress of combustion throughout the cylinder.

To obtain more spatially-resolved information, larger windows must be integrated into the design of the engine. Incorporating larger windows comes with the inherent challenge of replacing a significant portion of the metal structure of engine with a transparent material. Transparent cylinder sleeves (typically cylindrical, but sometimes square-shaped[1]), allow abundant viewing access to the combustion chamber for fluid imaging and combustion experiments. However, they are limited to low-pressure experiments due to the strength of the transparent material and cylindrical shape. A variant of the transparent cylinder is "ring access", or a ring-shaped window at the top of the sleeve affording 360°visibility around the top edge of the combustion chamber. The rest of the cylinder sleeve is still made of metal, affording increased strength compared to entirely transparent sleeves. A variant of this is to place rectangular windows on either side of the combustion chamber at the top of the sleeve.

Ring access and side windows in the combustion chamber offer spatial information in the direction orthogonal to the cylinder axis, as depicted in Figure 5.1. It can be challenging to interpret images taken in this direction because of the curvature of the cylinder wall. Another configuration for imaging is positioning windows along the cylinder axis, also depicted in Figure 5.1. Imaging in either direction provides spatial information about pressure waves, but the axial symmetry of Svrcek's water injection data begs for imaging capability along the cylinder axis. Furthermore, imaging along

---

[1]For more information on how to seal a square-shaped piston, ask CFE :)
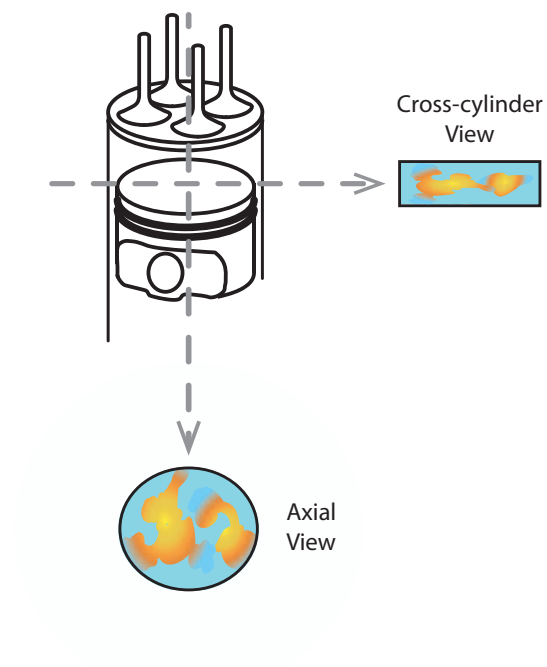
Figure 5.1: Directions to view combustion chamber

the axial direction allows a window to be placed in a flat surface of the combustion chamber, making image interpretation significantly simpler.

Two-stroke engines can be more easily modified for this type of on-axis imaging than four-stroke engines because the gas exchange process in a two-stroke engine doesn't require overhead valves. Thus, the cylinder head can be replaced with a transparent window material to offer a view of the entire bore. Successful studies of HCCI have been performed by Iijima in a two-stroke engine with full bore visualization up to a peak pressure of 50 bar [55] [62].

Optical fiber techniques and Schlieren photography were used in combination by Spicher et al. to study engine knock and HCCI combustion [56]. A specially-designed cylinder head was used, which had a single intake and exhaust valve on one side of the cylinder and a quartz window on the other side in the squish region of the piston. This type of cylinder head modification provides excellent access to one region of the combustion chamber. However, for the questions of the current study—concerning the interaction of pressure waves with large-scale inhomogeneity—it is necessary to view more of the cylinder than could be viewed by replacing a single valve.

The type of optical access employed in this experiment is referred to as Bowditch-style optical access.[2] A drawing of Bowditch-style optical access is shown in Figure 5.2. In a Bowditch-style engine an extended piston is used in place of the typical engine piston. The top of the Bowditch piston contains a window made of some transparent material (often quartz or sapphire) which provides optical access to the combustion chamber along the axis of the cylinder. A slot in the piston extension allows for a 45°mirror to be mounted in a fixed location, despite the movement of the piston. A high-speed camera can then be mounted outside of the engine, and focused on the reflection from the mirror to look up into the combustion chamber through the window. This configuration allows maximal optical area while preserving traditional overhead valves and slider-crank piston motion. It further allows for high-pressure studies to be undertaken if the Bowditch

---

[2]Named after Fred W. Bowditch, who designed the first engine of this type at General Motors Research Laboratories in the early 1960's [63].

Sapphire Window

Bowditch Piston

45° Imaging Mirror
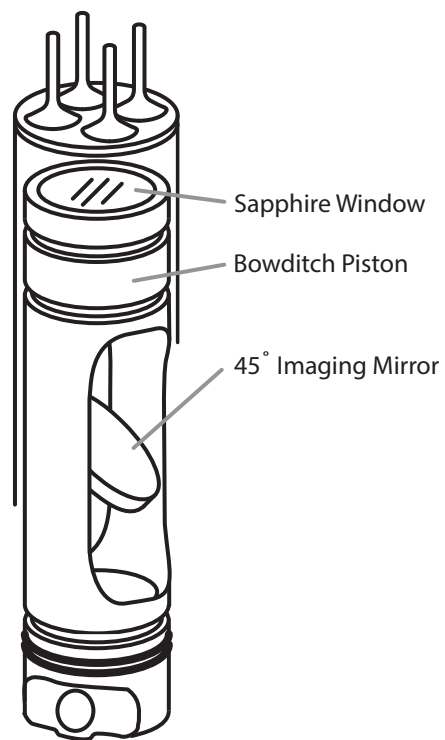
Figure 5.2: An illustration of Bowditch optical access as described in Sec 5.2

piston is sufficiently robust.

Bowditch-style optical access has been used to study HCCI by Dahl et al. [39]. The researchers used a single-cylinder AVL engine with a pent-roof head geometry and Bowditch piston containing a quartz window. They captured images of the HCCI ringing process, and even observed the expected pressure oscillation acoustic modes [54]. The ringing combustion they studied was at a 10.5:1 compression ratio and a load of 4.5 bar MEP—a light-load and modest compression ratio—well below the anticipated peak pressure of full-load ringing combustion.

5.2.1   Schlieren Imaging

Schlieren imaging is a technique used to visualize density gradients in fluid flows [64]. In obtaining a Schlieren image, incoming collimated light is passed through a region of interest, and variations in refractive index (which varies with density) cause some of the light to exit at a slightly deviated angle. By blocking a portion of the light with a knife edge at the focal point before the images are captured, some of this diverted light gets blocked. This creates a pattern of darker regions in the images corresponding to density gradients. Schlieren imaging is a very powerful tool for visualizing shock waves and areas of dilatation in gases during combustion of reactive mixtures. Incorporating this type of imaging in an optical engine allows pressure waves to be visualized.

Schlieren imaging can only be employed if there is an optical path for collimated light to travel through the engine. An optical path can be created with a single window if part of the combustion chamber has a mirrored surface to reflect light back through the window. Previous studies have been performed using mirrors for this purpose, either by replacing part of the cylinder head [56] or by mounting a mirror on the piston in cases with a transparent cylinder head [65, 66]. Traditional mirror materials such as glass or plastic would not survive the high pressures and temperatures associated with this type of experiment. For this reason, non-traditional mirror materials and manufacturing methods were pursued. In the

case of Svrcek, the combustion chamber mirror was made of highly-polished metal. It was from Svrcek's schlieren imaging experiments that the inspiration for the current engine came: A mirror polish is applied to the head surface inside the engine to overcome structural and thermal constraints of traditional mirror materials.

5.3 AVL Engine Test Bed

The starting point for this experimental development is a low-pressure optical access engine test bed purchased from AVL. It consists of the components listed in Table 5.1.

Table 5.1: AVL Engine Test Bed Components

AVL 577	Oil and Coolant Conditioning Unit
AVL 753C	Fuel Conditioning Unit
AVL 733S	Fuel Balance
AVL THA-100	Throttle Actuator
AVL 5411	Single Cylinder Engine Test Bed

The AVL 5411 Single Cylinder Test Bed is equipped with components for both Bowditch-style optical access and circumferential ring optical access (as well as conventional non-optical combustion experiments). Basic engine parameters are listed in Table 5.2. The dynamometer is a liquid-cooled, three-phase asynchronous motor, model AMK DW 13-170-4. A torque flange and speed sensor at the interface between the dynamometer and the engine flywheel measures the engine output. The engine test bed conditioning unit regulates engine oil and coolant temperatures to a user-defined set point. A fuel conditioning unit and fuel balance respectively set the fuel temperature and measure fuel mass flow rate for port fuel injection. An additional fuel pump was later added for direct injection of fuel at up to 200 bar.

The engine valves are actuated by an electro-hydraulic variable valve actuation system (EHVS) made by Team corporation. The EHVS allows a desired valve profile

Table 5.2: AVL Engine Experiment Parameters:

bore	82 mm
stroke	85 mm
speed	1000-3500 rpm
boost	1-4 bar, absolute

to be commanded from a dSPACE DS1103 PPC Controller Board computer and executed by hydraulic actuators equipped with linear variable differential transformer (LVDT) sensors for feedback on valve position. Dual encoders, Encoder Products Company model 716, and a Kistler Crank Angle Encoder Type 2614B, sense the crank angle degree of the engine and transmit it to both sensing and controlling computers.

Engine control commands are executed from both a dSPACE computer running a controller developed in Matlab's Simulink, and an additional computer running AVL Puma Open v1.4.1 software. Data are gathered and recorded by both the Puma software and AVL Indidcom 2011 Advanced Combustion Analysis Software. The Indicom system records crank-angle-resolved data at a rate of 10 samples per crank angle degree.

The engine's intake air can be supplied either via a naturally aspirated intake branch or using an artificial boosting system, as seen in Figure 5.3. The boost system allows the intake manifold pressure to be set and regulated up to 4 bar. Mass flow measurements for the air intake are obtained using a choked-flow orifice.

A Kistler 6061B water-cooled piezoelectric pressure transducer is used for in-cylinder pressure measurement. It has range of up to 250 bar peak pressure and a natural frequency of 90 kHz. The pressure signal is recorded at 10 samples per crank angle degree. The transducer is a dynamic pressure transducer (as opposed to an absolute pressure sensor), meaning the signal requires that a reference pressure be established. The reference pressure is determined in two ways: First, by using the value from an intake manifold pressure sensor (GP-50 model 211-C absolute pressure sensor) at the end of the intake stroke to reference the measurement, by assuming

Forced Induction Branch:

1000 psi tank — Pressure Regulator — Boost Plenum 1

Choked Flow Orifice

Naturally Aspirated Branch:

Air Filter — LFE — Hot Wire Anemometer — Boost Plenum 2 — Boost Vent — Throttle — Air Heater — Intake Plenum

Fuel Balance — Fuel Conditioning — Fuel Pump — DI Fuel Pump

Spark, DI injector, Pressure Transducer

EHVS

Exhaust Plenum

Lambda Sensor

PFI

Nitrogen Delivery Branch:

N2 Tank — Pressure Regulator — Choked Flow Orifice

Crank Angle to Encoder
Torque to Dynamometer

Figure 5.3: Schematic of the AVL single cylinder research engine with boost and nitrogen dilution capability.

the in-cylinder pressure and manifold pressure are the same at the moment of intake valve closing. Second, the reference pressure is checked by using the assumption of isentropic compression. With knowledge of the engine's geometric compression ratio and the value of specific heat of the in-cylinder gases, the absolute pressure can be determined. This capability is built into the Indicom engine recording software.

The compression ratio of the engine can be varied depending on piston design and also adjusted using shims. Overall, the engine test bed is a very flexible experimental platform for investigating a wide range of combustion strategies.
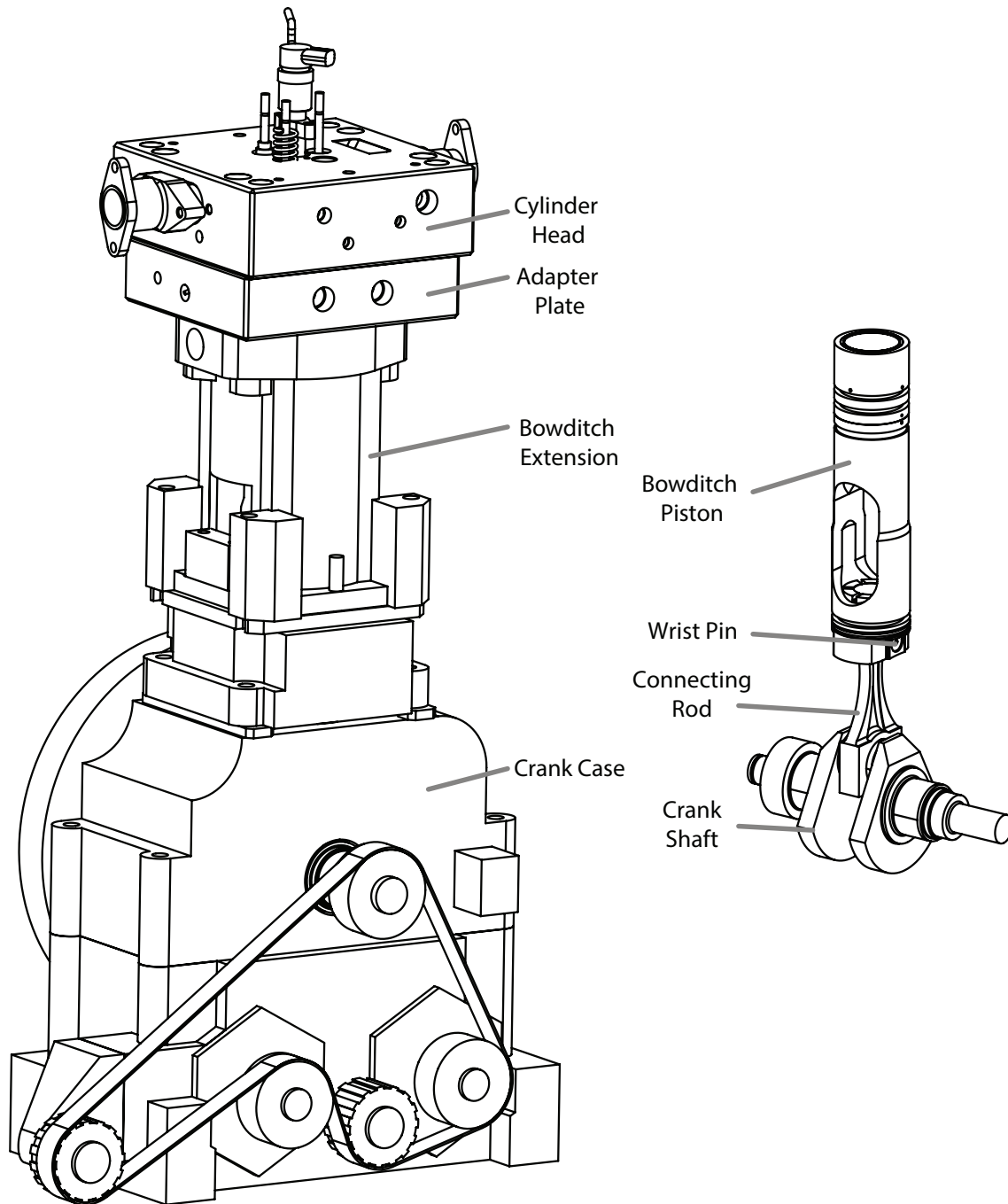
Figure 5.4: Major structural components of the optical access engine assembly.
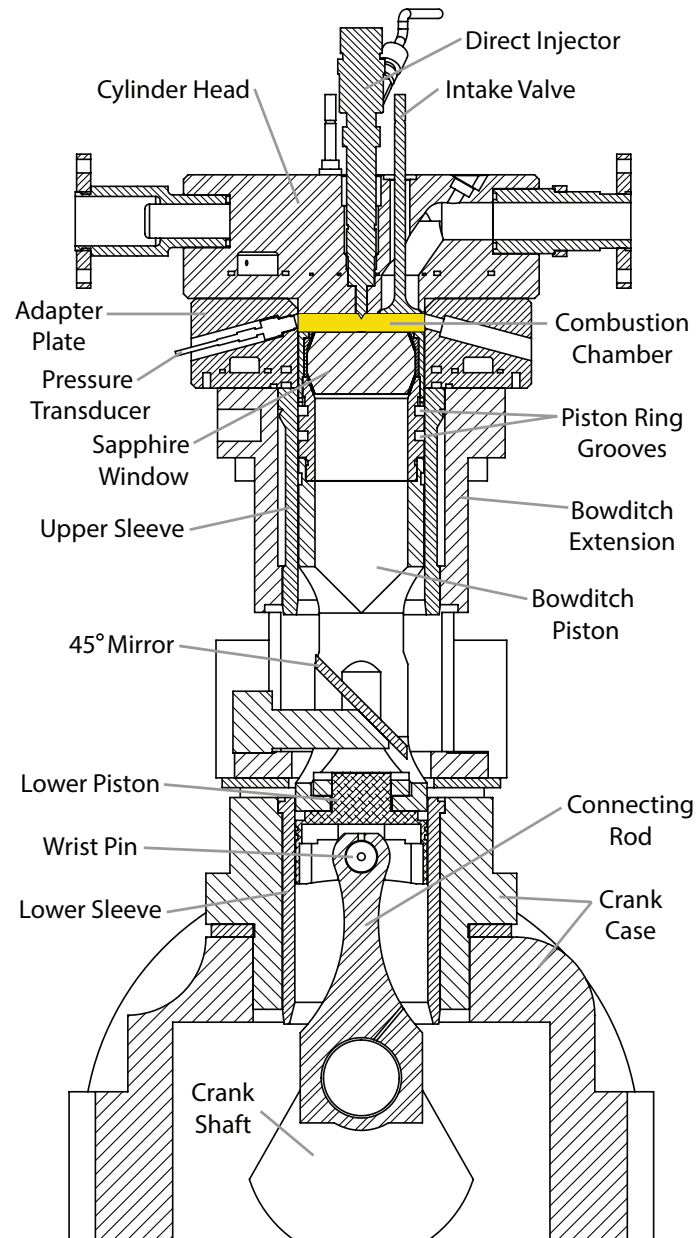
Figure 5.5: A cross section of the optical access engine assembly and the static pressure load that was applied to analyze the structure. Yellow indicates 250 bar loading in the combustion chamber.

5.4   Macro Stress Analysis

The single cylinder engine's original optical configuration, as purchased from AVL, is constrained for use in low-pressure combustion investigation. The most obvious constraint is the pressure limit on the ring window and the quartz Bowditch window, which are rated to a maximum pressure of 60 bar. A second, related constraint is the structural integrity of various other engine components under the stress exerted by the desired 250 bar peak pressure.

In addition to being one of the weakest points in the low-pressure optical engine, the ring access window is unnecessary for the type of imaging being undertaken here, which can be accomplished using a Bowditch piston and a mirror inside the combustion chamber. Eliminating ring access will limit the engine to "line of sight" imaging techniques and diagnostics (eliminating possibility for "perpendicular to line of sight" techniques such as PIV[3]), but this trade-off is necessary to make very high-pressure optical experiments possible.

The components were divided into two categories for stress analysis: static components and moving components. Major structural components of the engine can be seen in Figure 5.4. The major static components of the engine are the cylinder head, adapter plate, Bowditch extension, crank case, etc. The major moving components are the crank shaft, connecting rod, and piston and window assembly. On a cylinder bore of 82 mm the total resultant vertical force from 250 bar in-cylinder pressure is approximately 30,000 pounds of force. A schematic of pressure loading on the structure of the optical engine is shown in a cross section of the engine in Figure 5.5.

5.4.1   Static Components

After a first analysis of static components, it was determined that the static components which would fail under a cylinder pressure of 250 bar are:

---

[3]PIV stands for Particle Image Velocimetry, a fluid imaging technique allowing a velocity field to be determined by tracking motion of small particles entrained in the flow.

1. Bowditch Extension

2. Crank Case

3. Ring Window Enclosure

It was already determined that the ring window would be omitted from the high-pressure optical engine design, so in place of the ring window enclosure, an "adapter plate" was introduced in its place, as labeled in Figure 5.4. The design of this plate is further described in Section 5.7.

The crank case and Bowditch extension of the AVL engine are made of EN-JS1030 (GGG40 by DIN standards) ductile cast iron and thus require a recommended safety factor between 8-10 under cyclic impact loading [67]. Rather than re-design such large components out of thicker, stronger material, an alternative approach is to change the way the components are loaded. Ductile cast iron is an excellent load-bearing material under compression. For this reason, a set of bracing beams and threaded rods are introduced into the design to bear the vertical tensile stress caused by the in-cylinder pressure while keeping the cast iron components loaded in compression. A schematic of the new loading diagram can be seen in Figure 5.6.

The threaded rods are one-inch-diameter steel rods with rolled threads. They are anchored with high-strength steel nuts into the steel engine platform and onto the steel bracing beams. The brace beam nuts are torqued to a pre-load to impart a compressive force on all cast iron components that matches the tensile loading that would result from the maximum expected cylinder pressure. The value of the pre-load on each of the four threaded rods is equal to one-fourth of the resultant force from the expected peak cylinder pressure. To prepare the engine for experiments up to 250 bar, the threaded rods are tightened to 7500 pounds of force each to reach 30,000 pounds of compression total. In this way, the cast iron will bear load in compression, its preferred loading scenario, and the steel threaded rods, which perform well under tensile loading, will bear the load in tension. The steel rods and bracing beams were designed to a high safety factor so that in the event of excessive cylinder pressure
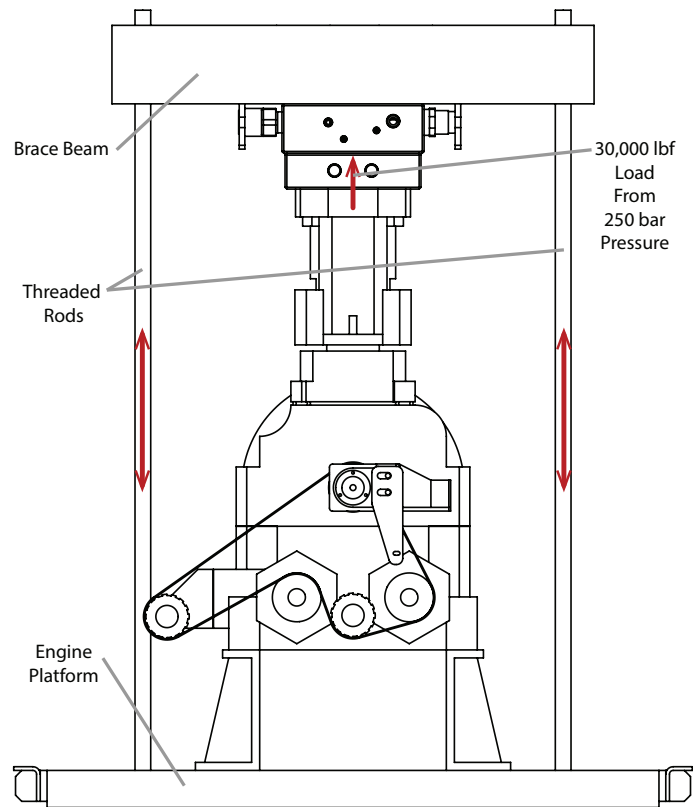
Figure 5.6: Brace beams and threaded rod bear pressure load in tension while ensuring that brittle components are loaded in compression.

beyond 250 bar, the cast iron components would experience a slight tensile loading, while the threaded rods would bear more tensile loading than anticipated. However, even under a cylinder pressure of 1000 bar (four times the maximum design pressure), the threaded rods and beams are designed to hold the structure without failure.

5.4.2 Moving Components

The high peak cylinder pressure will also have a significant impact on the moving components of the engine: the extended piston with window, the wrist-pin, connecting rod, crank shaft, etc. Each of these components was analyzed under the loading imparted by 250 bar in-cylinder pressure and it was determined that most required a revised design, both in dimension and in choice of materials.

The quartz window of the AVL engine has a pressure limit of 60 bar. Quartz is a commonly-used material in optical combustion experiments of all types, but it has insufficient strength for the most demanding applications. Sapphire (single-crystal Al_2O_3) is a much more attractive window material because it is optically transparent along its C-axis crystal orientation and has a very high rupture strength. Sapphire scores a nine on the Mohs scale, with Diamond being the only material harder than sapphire. Further, the coefficient of thermal expansion of most metals is closer to that of sapphire than to that of quartz, as seen in Table 5.3, making sealing between a window and the surrounding metal piston easier throughout the range of temperatures encountered in combustion experiments.

Table 5.3: Coefficients of Thermal Expansion in μm/(m°C): [68, 69]

Sapphire parallel to C-axis	6.05
Sapphire perpendicular to C-axis	7.08
Quartz	0.7-1.4
Titanium	8.6
Steel	12.0
Aluminum	22.2

5.4.3   Piston Rings and Crevices

An additional consideration in optical engines is the requirement of an oil-free combustion chamber. Engine oil and other lubricants can quickly foul mirror and window surfaces, hindering imaging. Thus it is necessary to design a way to operate the engine without such conventional lubricants. The most difficult aspect of avoiding oil near the combustion chamber is selecting piston rings, which usually rely on an oil film to slide and to seal the edges of the piston. Candidate materials for so-called "dry rings" must have a combination of a high strength, low friction coefficient, high wear-resistance, and resistance to damage from combustion gases.

The piston rings provided by AVL are formed from a bronze-Teflon material, with a reported operational lifetime of 20-40 hours motoring.[4] AVL recommends limiting firing cycles to 30 second intervals for ring survival and also thermal expansion concerns of the quartz window enclosure.[5].

An effective way to operate an optical access engine is to motor the engine at a constant speed, with intermittent bursts of firing cycles to acquire data and images. Dry piston rings that allow the engine to motor for an extended period of time before needing to be replaced will facilitate this experimental approach. If rings cannot survive motoring for very long, the engine will need to be disassembled often for piston rings to be replaced.

A consequence of the dry piston rings is an increase in the engine's crevice volume. The dry piston rings are situated further down the piston than typical piston rings, to allow combustion gases to thermalize to the temperature of the piston or wall before encountering the dry rings, preserving their lifetime and sealing ability. Crevice volume is usually minimized in engine design because crevices can quench flame propagation, and contribute to unburned hydrocarbon emissions.

---

[4]In this context, *motoring* the engine refers to engine operation in the absence of combustion while *firing* the engine refers to engine operation with combustion.

[5]Recall that thermal expansion considerations are more limiting for quartz windows compared to sapphire windows, as discussed in Section 5.4.2
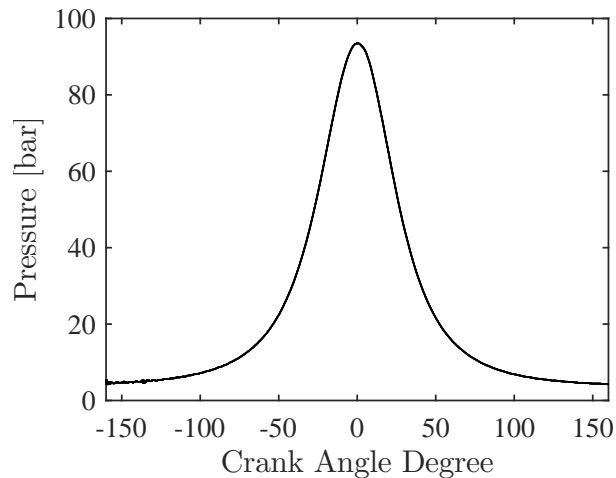
Figure 5.7: A boosted motored pressure trace gathered during initial testing as described in Sec 5.5

5.5 Initial Testing

Before proceeding with re-design of engine components, initial engine testing of the low-pressure AVL optical access setup was performed to assess dry piston ring performance and the effect of increased crevice volume. The engine was assembled with the piston rings provided by AVL and motored under various boosted conditions and engine speeds. It was important to experimentally assess the sealing ability and longevity of the piston rings being used to seal the combustion chamber to determine if alternative ring materials should be explored. It was also important to understand the practical implications of increased crevice volume on engine operation.

The engine was assembled in its optical configuration with the low-pressure AVL Bowditch piston and the pent-roof cylinder head that was previously used for other (non-optical) single-cylinder engine experiments. A first-generation "adapter plate" was used in place of the ring access window. To account for the decrease in geometric compression ratio resulting from the use of a flat piston with a pent-roof cylinder head, boost pressures up to 4 bar were imposed on the intake to test the rings at
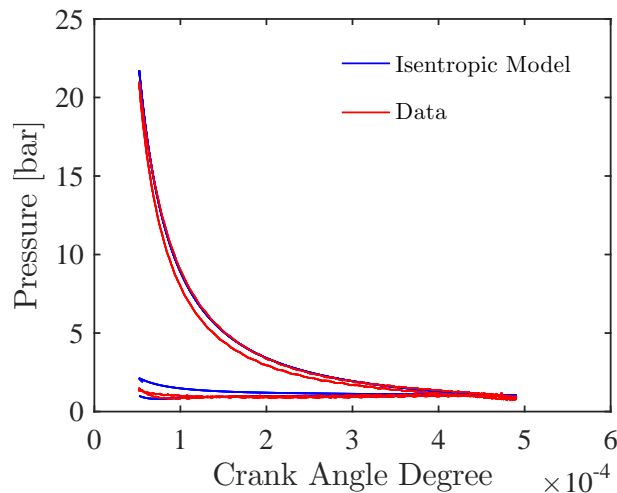
Figure 5.8: Comparison of isentropic compression and motored engine data as described in Sec 5.5

higher cylinder pressures. For these initial tests, an aluminum piston top, seen in Figure 5.10, was manufactured to the same dimensions as the AVL quartz piston top to allow higher test pressures than would be possible with the quartz window.

5.5.1   Dry Ring Performance

The effectiveness of the dry piston rings was first assessed by motoring the engine through the range of conditions expected in the final experiment. The boosted air intake was used to push the in-cylinder pressure as high as possible to test if the piston rings would leak or fail above a certain pressure. The peak pressure achieved in the engine in this configuration was 94 bar and the highest engine speed was 3000 rpm, as limited by the EHVS. A sample motored pressure trace can be seen in Figure 5.7. The rings were not tested up to the design pressure of 250 bar, and the effect of combustion gases was not assessed.

   The sealing ability of the piston rings was evaluated by comparing the peak experimental pressure to the theoretical isentropic peak pressure as calculated by a computational model. The rings sealed the combustion chamber such that a motored
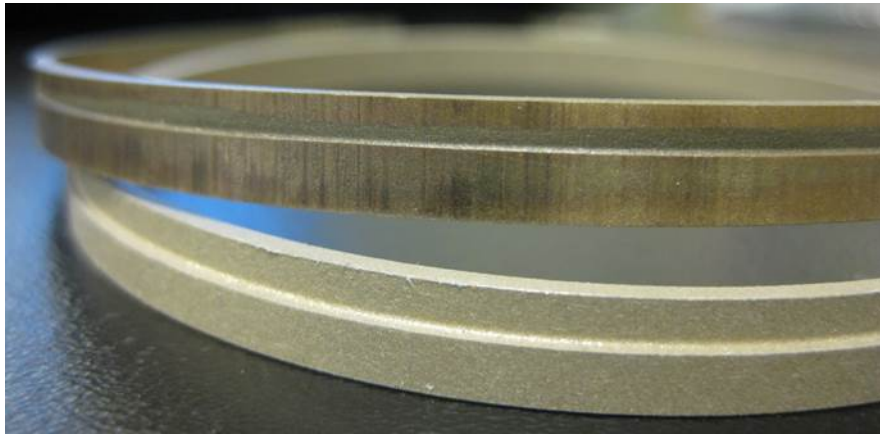
Figure 5.9: Photo showing dry piston rings before (lower) and after (above) 2 million revolutions of motored engine operation.

pressure trace reached 98% of the modeled isentropic peak pressure.[6] Experimental motoring data matched extremely well with modeled pressure as seen in Figure 5.8.

Table 5.4: Mass of Dry Piston Rings

Component	Mass [g]	Percent Lost
mean unused ring weight	10.1	—
upper used ring weight	9.4	6.9%
lower used ring weight	9.5	5.9%
unused guide ring weight	6.6	—
used guide ring weight	6.6	0.0%

The ring wear for the dry optical access rings was assessed by their continued ability to seal the in-cylinder pressure, and by weighing the rings before and after the motoring experiments. There was no significant loss of pressure sealing ability after motoring the engine through over 2 million revolutions.

Another way to approximate ring wear is by measuring the mass rings lost during operation. The mean weight of un-used optical access rings, as well as the final weight

---

[6]The computational model captured effects of air flow through the intake valves, and modeled cylinder pressure at the time of intake valve closing matched the experimental data. The cylinder head used in these experiments, being a pent-roof design, had large intake valve area and well-designed intake ports.

Figure 5.10: Photo showing AVL Bowditch piston with aluminum piston top in place of the quartz window top (shown on the left in the photo).

of worn-in optical access rings, is displayed in Table 5.4. The rings lost approximately 5-7% of their mass during these tests. A closeup photo of a used ring compared to an un-used one can be seen in Figure 5.9. The ring surface is slightly deformed into grooves in the direction of piston motion, but because the rings performed so well in sealing the pressure, the surface appearance is not indicative of ring performance.

5.5.2   Blowby Measurements

A further assessment of ring performance can be made by measuring the blowby, or the amount of in-cylinder gas that escapes past the rings each cycle. In this case, blowby was measured by sealing all exit points to the engine crank case except for a single exit point, which was directed through a rotameter to determine volumetric flowrate.

The blowby measurements were only an order of magnitude larger than the sensitivity of the rotameter, and as is expected with a dynamic flowing system (and a single-cylinder engine), the measurements were unsteady. However, the highest flowrate observed was 0.35 SLPM, indicating that the blowby is likely bounded by this value. This corresponds to 0.2% of cylinder volume blowing by each cycle, a very small fraction even by the standards of production engines.[7]

Based on the very high fraction of isentropic pressure reached, and the consistency with which it was reached throughout the ring wear experiments, it was concluded that the rings were capable of maintaining a seal throughout motoring conditions, even in cases of high boost. It remained to be seen how the rings perform under combustion conditions, but it was thought that the large crevice distance between the top of the piston and the top of the rings should provide ample surface area to thermalize the crevice gas to a temperature more closely matching that of the piston and cylinder wall.

---

[7]At an engine speed of 1200rpm and 100% volumetric flowrate, the air flow through the engine is 270 SLPM of air
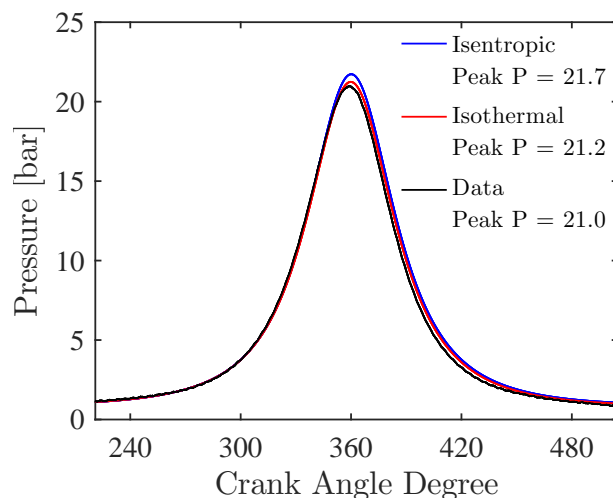
Figure 5.11: Comparison of isentropic model, isothermal crevice volume model, and actual data, as described in Sec 5.5.3

5.5.3 Effects of Increased Crevices

A second goal of this initial installation was to investigate the role of increased crevice volume on the compression and expansion of in-cylinder gases. Crevices can be thought of in two ways, which bound the real behavior of the engine. The first is to think of crevices as adiabatic—that is, no heat transfer occurs in the crevice volume and the density of the crevice gas is the same as that of the core gas in the cylinder. The second is to think about crevices as isothermal—that is, the proximity of the piston surface and cylinder wall ensure that maximal heat transfer occurs and the mass contained in crevices is at the same temperature as the cylinder wall and piston.[8] In reality neither of these extremes are true, but the bounds they place on the actual behavior provides valuable insight.

The largest crevice volume in the optical access engine experiment is the "upper ring land": the space below the top of the piston and above the topmost piston ring. Other crevices include the small gaps between metal components and combustion

---

[8]Based on the plan to operate the experiment with intermittent firing, it is assumed that the cylinder wall temperature and piston surface temperature are equal to the coolant temperature.
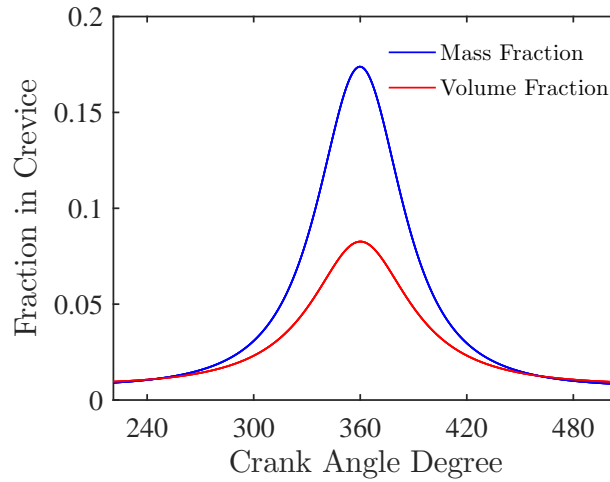
Figure 5.12: Percentage of cylinder mass and volume located in crevices as a function of crank angle degree

chamber seals, gaps around the edges of the spark plug and pressure transducers, etc. The shape of the crevice is a cylindrical shell 48 mm tall and 0.35 mm thick, with a total volume of 4 cubic centimeters. This corresponds to 8% of the clearance volume at TDC, as can be seen by the red line in Figure 5.12. The red line also reflects the fraction of mass in the cylinder that would reside in crevices in the adiabatic scenario, while the blue line is a "worst" case scenario (isothermal). In the isothermal case, 17% percent of the total mass is residing in the crevice volume at TDC. For this reason, in the optical engine experiment, the effective compression ratio of the optical engine[9] would be lower than the geometric compression ratio.[10] However, Figure 5.11 demonstrates that despite the large fraction of mass contained in crevices, there is only a small difference in peak pressure between the two modeled cases. In fact, the difference in peak pressure is only two percent when modeling the crevices as isothermal instead of adiabatic. Figure 5.11 further confirms the relatively small effect of crevices on peak pressure by plotting experimental data on top of the

---

[9]Effective compression ratio is calculated by ρ at TDC divided by ρ_0

[10]Geometric compression ratio is the ratio of cylinder volume at TDC divided by cylinder volume at BDC

two modeled pressure traces. The data match very closely, being only slightly below the model. The coolant temperature was set to 34°C in the experiment, to reflect a realistic "worst" case scenario, and in the model this was the temperature of gases in the crevices in the isothermal case. The data fall slightly below the isothermal modeled pressure trace, most likely due to blowby past the rings (not captured in the model), and heat transfer to the piston surface, which may have been even colder during motoring than the cylinder liner and head temperature as imposed by the coolant. Overall, the departure from isentropic behavior of both the isothermal model and the experimental data is minimal, suggesting that increased crevice volume from using dry piston rings does not drastically alter the engine behavior.

The initial testing on the low-pressure optical access engine alleviated two important concerns leading into the high-pressure engine design: dry ring performance and the effect of crevices. The dry piston rings maintained good performance throughout two million cycles, while the effect of increased crevice volume showed only a very small effect on the peak pressure of motored pressure traces in the engine.

5.6   Optical Access Cylinder Head

The high-pressure optical access experiment required a completely re-designed cylinder head. This section describes the design, its requirements, stress analysis, materials considerations, and associated challenges.

The most unique feature of the new cylinder head is a flat combustion chamber surface which is proud of the bottom surface such that it can easily be polished to a mirror finish, enabling imaging techniques such as Schlieren to be used in the engine. The cylinder bore of 82 mm and the constraint that the cylinder head surface be a flat mirror means that the available space for the engine's valves, sensors, and actuators is limited.

One major consequence of this limited cylinder head area is that the head has
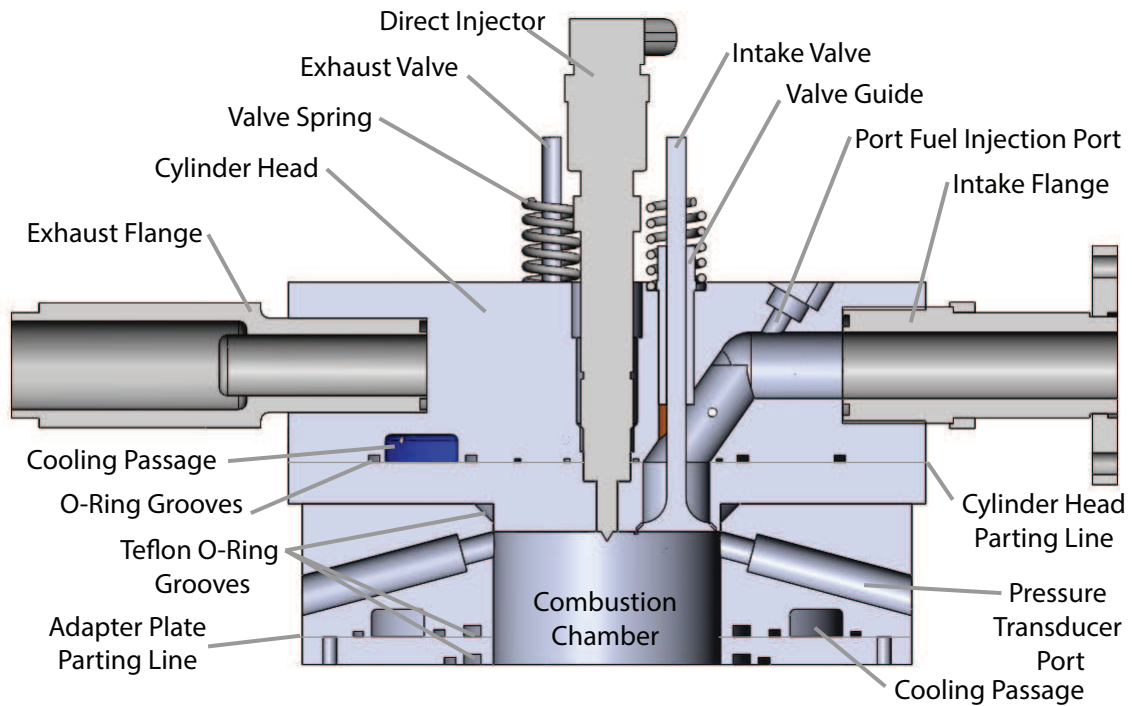
Figure 5.13: A close-up, cross-sectional view of the cylinder head and adapter plate.

only three valves. In order to produce breathing behavior most similar to a conventional engine, and knowing that the intake air supply can be artificially boosted, exhaust valve area was prioritized. Boosting air intake to achieve a desired volumetric efficiency through a smaller valve area is more attractive than interpreting pressure data in light of elevated residual pressure due to restricted flow through a single, small exhaust valve. For this reason, there are two exhaust valves but only a single intake valve. This configuration resulted in the best use of space in the cylinder head consistent with experimental goals.

As seen in Figure 5.13, the cylinder head has a single centrally-located injector port for high-pressure injections. The port is compatible with a Bosch HDEV 5 direct injection gasoline injector as well as several types of Diesel fuel injectors, including the Bosch CRI-2 solenoid injectors and Bosch CRI3-20 piezo injectors. This

centralized injector port will enable future high-pressure imaging studies of reacting Diesel plumes, direct-injected gasoline combustion, and other high-load combustion concepts. More relevant to the current work, this port will allow a moderator such as water, CO_2, or nitrogen to be injected into the center of the combustion chamber, creating a large-scale inhomogeneity to mitigate ringing. This inhomogeneity and the resulting combustion dynamics will be centrally located in the field of view of the Bowditch optical access.

The cylinder head also contains ports for an in-cylinder pressure transducer and a spark plug. It was desired that all required functionality for engine operation be contained in the cylinder head, rather than auxiliary components. The pressure transducer port accommodates a Kistler 6061B water-cooled piezoelectric pressure transducer and the spark plug port accommodates an NGK 8 mm racing spark plug. A surface-gap spark plug is ideal for this application because the low profile does not intrude into the combustion chamber, preserving experimental flexibility.

Throughout the design of the cylinder head, the structure was analyzed using SolidWorks finite element analysis (FEA) under the following static loading conditions:

1. 250 bar pressure on combustion chamber surface, and

2. 30,000 pound compressive force imparted by brace beams, once threaded rods are tightened down to pre-load the cast-iron components in compression.

The results of finite element calculations were used to iterate on the design, adjusting dimensions and port locations until a safety factor of 3 could be reached. Material selection for the cylinder head was determined by a combination of each candidate material's strength and ability to be polished to a mirror surface. The best material for the polishing vendor was 304 stainless steel. Dimensions of the cylinder head were adjusted appropriately such that it could be manufactured from this material and survive the demanding loading it would experience during high-pressure experiments.

The cylinder head was manufactured in two parts that are bolted together. This allows for cooling passages inside the head. It was also determined that the mirrored surface of the cylinder head—the part touching the combustion chamber—is likely to be damaged if there are failures of other components. For this reason, as much complexity as possible was built into the upper component, while the lower (mirrored) part could be simple and easily re-polished, with a duplicate kept on hand for quick rebuilds in case of damage.

Manufacturing a cylinder head that, together with its valves, creates a flat mirrored combustion chamber surface presents a formidable challenge. After polishing operations were completed on smaller, prototype cylinder head and valve components, it was determined that to create a single, planar, mirrored surface out of multiple components, they must be first assembled and then polished as a unit. For this reason, after the cylinder head and valves were initially manufactured, they were assembled with installed valve guides and ground valve seats. Then the bottom surface of the assembly was ground to create a single planar surface, and polished to a mirror finish as a single unit. A "polishing rig" was designed to hold the valves rigidly in place against their seats during both of these post-assembly machining processes, after which they could be secured by valve springs and keepers.

The outcome of polishing the assembly was very successful. A surface finish roughness measuring tens of Angstroms was achieved, creating a single, planar, Schlieren-quality mirrored surface capable of surviving a high temperature and pressure combustion environment. Attention was paid to grinding of valve seats to preserve optical area. A ring only 1.5 mm wide surrounds the perimeter of each of the three valves, meaning most of the cylinder head and valve surface is part of the mirror. No additional area is lost to the pressure transducer and spark plug beyond the area they themselves take up. Overall, a high percentage of available cylinder head area is usable for imaging in high pressure experiments. A view of the actual mirrored cylinder head surface inside the combustion chamber can be seen in

Figure 5.14.
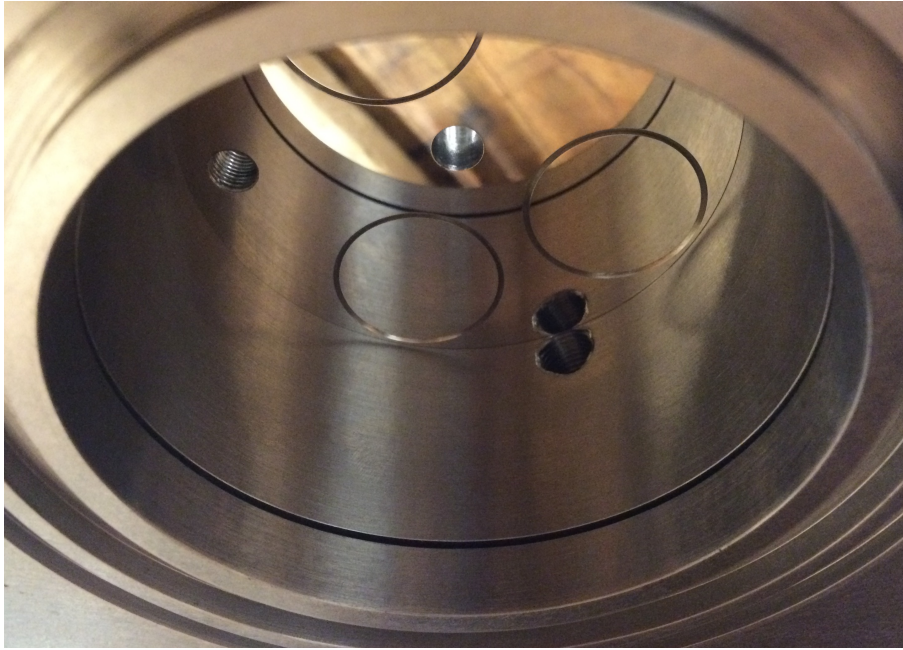
Figure 5.14: View inside the optical access combustion chamber showing mirrored surface of valves, central DI injector, surface-gap spark plug, pressure transducer, and side port for additional pressure transducer.

5.7   Optical Access Adapter Plate

This section describes the design and manufacturing of the component that serves as the combustion chamber side walls when the engine is assembled. It takes the place of the AVL-supplied ring-access component, which was inadequate due to its limited pressure range. It is located below the cylinder head and above the cast iron Bowditch extension, and is designed to be strong enough to withstand high in-cylinder pressure. Further, it must accommodate coolant flow to regulate cylinder wall temperature.

The adapter plate contains ports for two additional in-cylinder pressure transducers, as seen in Figure 5.13.   Multiple pressure transducers in the

combustion chamber allow information on wave speeds to be extracted, since a traveling pressure wave will arrive at each transducer at a different time. This can be used to corroborate image sequences from combustion events, and helps gain quantitative information about the thermodynamic state of the reacting gases via the sound speed.

The adapter plate was analyzed using SolidWorks finite element software under the following static loading considerations:

1. Hoop stress produced by 250 bar in-cylinder pressure.

2. Compressive stresses from 30,000 pound pre-loading of the entire assembly.

The results of the finite-element analysis were used to iterate on the design of the adapter plate, to determine dimensions such as wall thickness around the combustion chamber. The adapter plate is fabricated from 4340 normalized steel. This alloy has high tensile strength and toughness, making it an excellent candidate material for such a demanding high-pressure experiment.

The adapter plate, like the head, was manufactured in two pieces so that internal cooling passages could be integrated into the design. This introduced an additional seam in the combustion chamber, which must be sealed to withstand 250 bar pressure at high temperature. Teflon o-rings were used for this task due to their ability to withstand high pressures without extruding, as well as surviving high temperatures. There was an additional design trade-off between allowing space between combusting gases and o-rings to thermalize the gases being sealed, versus introducing additional crevice volume in the combustion chamber.

5.8 Bowditch Piston

The Bowditch piston assembly and labeled parts can be seen in an exploded view in Figure 5.15.
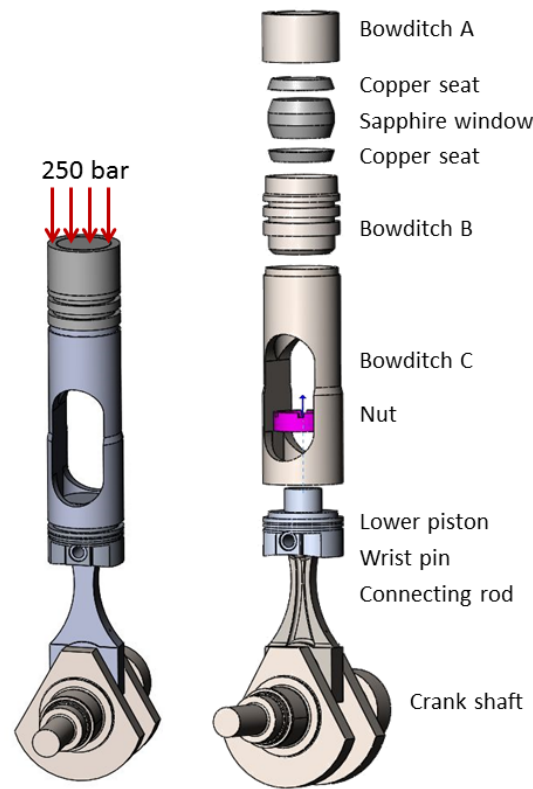
Figure 5.15: A view of assembled and exploded bowditch components plus the location and orientation of 250 bar loading

The sapphire window has a bi-conical design so that it can be seated into a pair of annealed copper seats and pre-loaded in compression to form a tight seal. The compression pre-load is imposed by torquing the surrounding threaded components together and also helps the sapphire material to bear the load of the combustion chamber pressure. Sapphire has a high modulus of rupture of 420 MPa, but like most brittle materials, it is best at bearing compressive loads. Pre-loading the window in compression prevents tensile loading on the lower surface of the window when it seals high pressures. Sapphire is an anisotropic material, and is situated with its C-axis aligned with the axis of the cylinder, allowing it to be optically transparent during

imaging and best able to bear the load of high cylinder pressure.

The Bowditch piston assembly was analyzed using SolidWorks FEA software under a number of loading scenarios during design iterations, since both pressure loads and inertial loads will be significant during operation. The loading scenarios and results are discussed in the following sections.

5.8.1 Bowditch Static Loading

The sapphire window and its enclosure were analyzed under 250 bar in-cylinder pressure loading. In analyzing these components it was determined that the material tensile strength of the window enclosure has a large influence on the available window viewing area that can be safely accommodated in the design. For this reason, Ti-6Al-4V titanium alloy was chosen to enclose the window. The enclosure is assembled with threads between each component, and locking pins are installed after assembly for added safety.

The lower portion of the Bowditch piston, the region with the slotted opening, is the most limiting component in the Bowditch assembly. Its geometry is more constrained than other components—its outer diameter must fit within the cylinder bore, while its inner diameter determines the maximum diameter of optical area visible in the engine.[11] It had to be sufficiently strong under the in-cylinder pressure load applied, but also have a slotted opening allowing the mirror mount to pass through. For this reason the Bowditch extension was made from 4340 normalized steel.

In addition to being analyzed under a static 250 bar (30,000 lbf) compressive load using the FEA package, the Bowditch extension section was also analyzed for buckling, based on its geometry. The wall thickness of this component had to be increased significantly from that of the original AVL component, from about 3 mm to 10 mm. The inner diameter of the Bowditch extension is 60 mm, the same as the

---

[11]The inner diameter of the lower portion of the Bowditch piston is the upper limit on the size of the 45°mirror, and thus the diameter of visible area.

diameter of the top and bottom surfaces of the sapphire window. A 58 mm-diameter angled mirror can be mounted in the center of the extension section, allowing the maximum diameter of the field of view to be 58 mm.[12] A drawing of the optically accessible area in the cylinder, based on the limitations presented by the strength of the Bowditch extension and mirror size, can be seen in Figure 5.16.
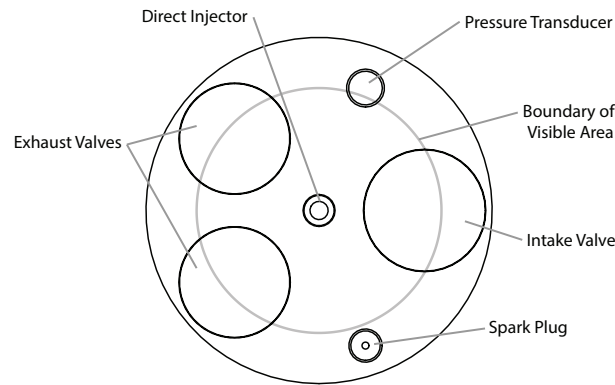
Figure 5.16: An illustration of the 58 mm diameter optical area drawn onto a view of the cylinder head and valves.

5.8.2   Bowditch Inertial Loading

Beyond pressure loading, the reciprocating components also experience an inertial load resulting from the piston motion and mass of components. A plot of piston position, velocity, acceleration, and force imparted on the connecting rod can be seen in Figure 5.17. The loading on each component is determined by the acceleration of the assembly and the total mass of components located *above* the component of interest. A list of component masses and the corresponding maximum force can be seen in Table 5.5.

---

[12]Vibrational analysis of the cantilevered mirror will follow, in Section 5.8.3

Table 5.5: AVL Engine Experiment Parameters:

Component	Mass [g]	Max Force [lbf]
Bowditch A	504	207
Bowditch B	920	387
Bowditch C	2756	926
Sapphire Window	554	–
Bowditch Nut	257	976
Lower Piston	404	1056
Wrist Pin	90	1074
Connecting Rod	1251	1318
Total Mass	6479	1318
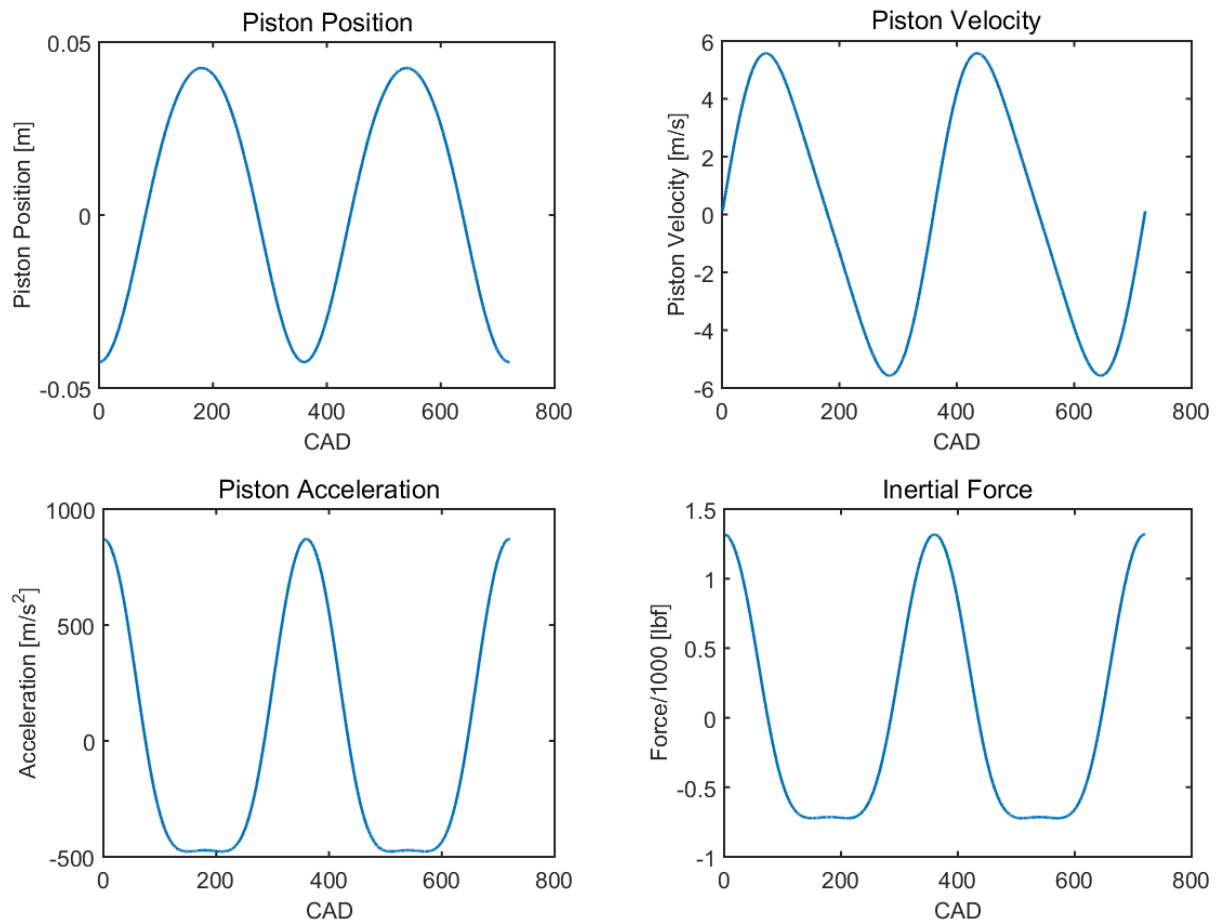
Figure 5.17: Piston position, velocity, and acceleration, as well as the inertial force on the connecting rod (which experiences the highest inertial loading) due to engine rotation at a speed of 1200rpm

To accommodate the new Bowditch extension, the Aluminum AVL lower piston was modified, and the wrist pin was replaced with a thick-walled heavy-duty wrist pin. The connecting rod was also redesigned to be robust enough for the high cylinder pressure and increased inertial loading from the significantly greater piston mass compared to that of a conventional engine. The new custom connecting rod is an H-section designed by CP Carrillo manufactured from *Carrilloy*, their own blend of 4330M steel alloy. It is intended for high-pressure applications and its dimensions match the wrist-pin diameter and crankshaft bearing size of the previous low-pressure AVL engine configuration.

The AVL optical crankshaft, made of 31CrMoV9, was found to be sufficient to survive the high-pressure application. Larger balance weights were attached to the two counter-rotating balance shafts in the crank-case to compensate for the significantly larger reciprocating mass.

5.8.3   Mirror Vibrational Analysis

The 45°mirror and mirror mount are not part of the moving components of the engine, but their analysis is included here because they are susceptible to vibrational loading resulting from the motion of the Bowditch piston. The mirror and its mount are attached to the Bowditch extension and cantilevered within the moving Bowditch piston slot. A drawing of the mirror and its mount can be seen in Figure 5.18. There is only 1 mm clearance between the outer radius of the mirror and the inner radius of the Bowditch piston, and a collision of these components would likely be catastrophic. For this reason, an analysis of the vibrational modes of the cantilevered beam and mirror assembly were undertaken using SolidWorks's FEA package. The beam holding the mirror was designed with as large a moment of inertia about the horizontal axis (indicated in the figure) as geometry of the moving Bowditch piston permitted. The moment of inertia of the cantilevered beam about the horizontal axis will determine natural vibrational modes of the mirror, where a larger moment of inertia results in higher frequencies. It is necessary for the natural frequency of

the structure to be significantly higher than the frequencies it is likely to encounter during engine operation, to avoid resonant vibrations.
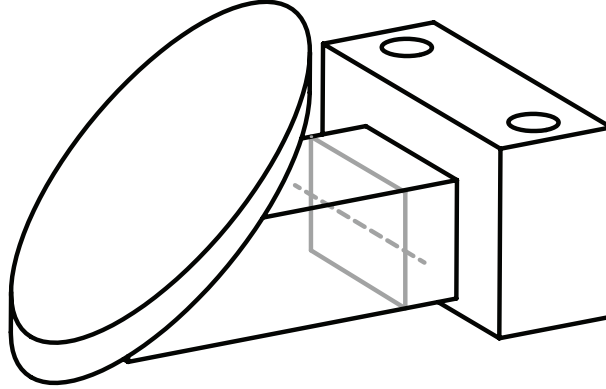
Figure 5.18: Mirror mount and 45°mirror. The cross section and horizontal axis about which vibrational modes were calculated is indicated in gray.

At 1200 rpm, the natural motion of the reciprocating piston produces a vibration at 20 Hz. Given the size and complexity of the engine structure, additional frequencies are undoubtedly present which may affect the mirror. The first five vibrational modes of the mirror mount, as calculated using the FEA analysis, can be seen in the table below. The lowest-frequency mode is well above the input vibration frequency of 20 Hz, providing confidence that the natural frequency modes of the mirror mount will not be excited. The most likely vibrations of the mirror will also be slow compared to the time-scale of combustion events and the frame rate of the high-speed camera, meaning that they will not impact imaging capability.

5.9 Assembled Optical Access Engine

This section describes how the high pressure optical access engine was manufactured and assembled.

To prevent oil contamination in the combustion chamber, special consideration

Table 5.6: Frequency Modes of Optical Engine Mirror Mount:

Mode	Frequency [Hz]
1	3000
2	5902
3	3483
4	4939
5	75875

was made for lubrication of valve stems with a minimal amount of thick lubricating grease rather than oil.

A front view of the assembled high-pressure optical access engine can be seen in Figure 5.19. A more detailed cross-sectional view of the cylinder head and Bowditch section can be seen in Figure 5.5. The EHVS sits atop the brace beams, allowing a small clearance area to access the spark plug, injector, and pressure transducer. The intake and exhaust systems are connected to the cylinder head, to allow delivery of boosted air and routing of exhaust, for either venting, recirculating, or emissions measurements.

To ensure a safe working and operating environment, a polycarbonate shield was constructed surrounding the engine on the sides most likely to encounter flying debris in the event of component failure. The shielding will withstand high-energy impact and protect personnel and equipment in the lab.

A photograph of the completed engine can be seen in Figure 5.20. Once completed, the various functions of the new engine were tested and demonstrated in motored and fired conditions. Some aspects of the design, such as balance, valve behavior with the EHVS, and sealing of the combustion chamber during firing, are most easily assessed by operating the engine. Results and operations during engine operation provide feedback for any necessary adjustment or re-design of components. Experimental results from demonstrations of the high-pressure optical access engine are discussed in Chapter 6.
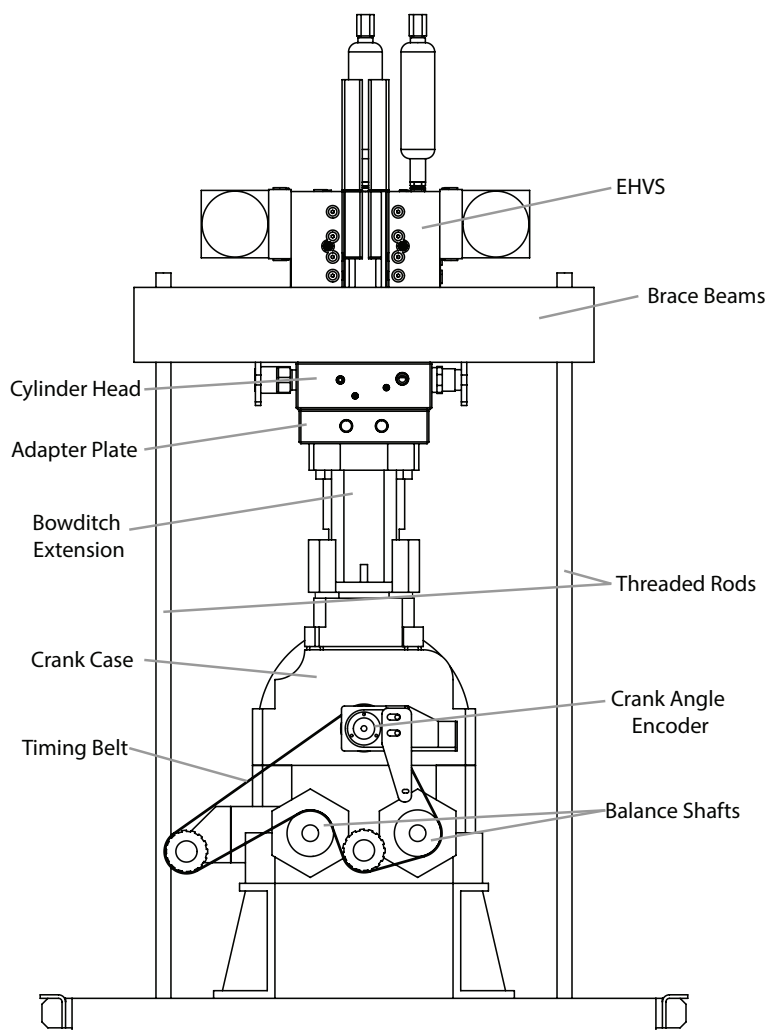
Figure 5.19: Front view drawing of final high-pressure optical engine assembly
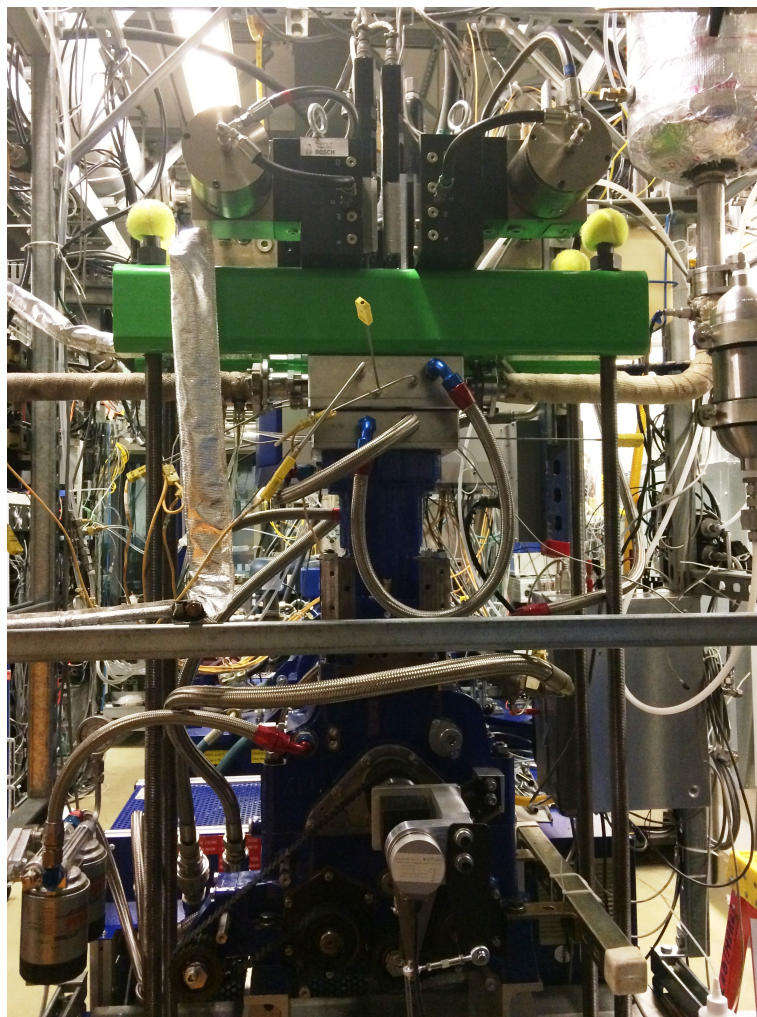
Figure 5.20: Front view photograph of completed high-pressure optical engine assembly

Chapter 6

Optical Access Engine Demonstration

This chapter describes the demonstration of the high pressure optical-access engine and results of initial experiments. A discussion of the experimental capability in reference to meeting various criteria for the experiment that were set out in Section 5.1 concludes this chapter.

6.1 Demonstration 1: Aluminum Window Blank

The high pressure optical access engine was assembled according to the design described in Chapter 5. For initial testing of new components, the sapphire was replaced with an aluminum blank of the same mass (to preserve the engine's balance). The high-pressure Bowditch piston with aluminum window blank can be seen in Figure 6.1

The goals of the aluminum "window" tests were to evaluate performance of the engine under motoring and firing conditions after integrating the new high-pressure components into the engine experiment. Sealing of the combustion chamber and window assembly, hydraulic valve actuation, thermal management of components,

127

Figure 6.1: High pressure Bowditch piston, assembled with aluminum window blank.

ring performance under combustion conditions, and balance and vibration were among the factors explored in experiments with the aluminum window blank installed.

The engine operated extremely well through a range of motored and fired operating points. Propane was port-injected and spark ignited for the firing cycles. Data from the engine operating in spark-ignited combustion are plotted in Figure 6.2, along with a motored modeled pressure trace. The purpose of comparison with the modeled pressure trace is to compare the optical engine performance to what would be expected from a conventional engine. Matching the compression stroke of the motored model means that the compression of air and fuel in the Iris engine are nearly isentropic. This means that any losses associated with heat transfer, crevices, or dry piston ring leakage do not substantially affect performance. The model and data diverge at the point where combustion begins, as is expected, because the model does not include combustion in this case. The difference in pumping loops is exaggerated by the log scale of the plot and has far
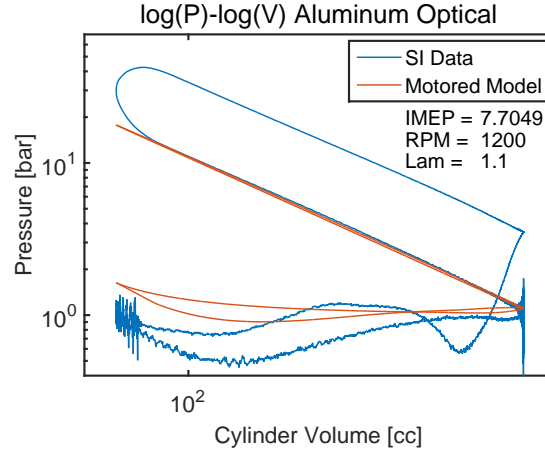
Figure 6.2: Plot of SI combustion in the aluminum Iris engine configuration. The combustion data are compared to a motored engine model of isentropic compression and expansion. Intake manifold pressure for model and experiment is 1.2 bar. The oscillations in the signal during the pumping loop are a result of valves opening and closing.

less impact on engine operation than the compression and expansion stroke behavior.

The compression ratio of the engine in this installation was low, around 7:1[1], which made it difficult to transition from SI combustion to HCCI. The engine was operated in SACI (spark-assisted compression ignition) combustion mode with the intake air boosted to 2.3 bar and heated to 100°C, while trying to transition the engine into HCCI mode. SACI combustion is very similar to HCCI combustion, with the addition of an early spark to ignite a portion of the mixture and prompt autoignition in the bulk of the charge. The engine continued to seal after experiencing cylinder pressures in excess of 100 bar. Many of the pressure traces exhibited pressure waves such as those being studied in the current work. Two different SACI cycles are plotted in Figure 6.3. Overall, combustion operation was consistent with what might be expected from a low-compression-ratio engine being pushed to operate

---

[1]The compression ratio is determined by thickness of two sets of shims when the engine is assembled.
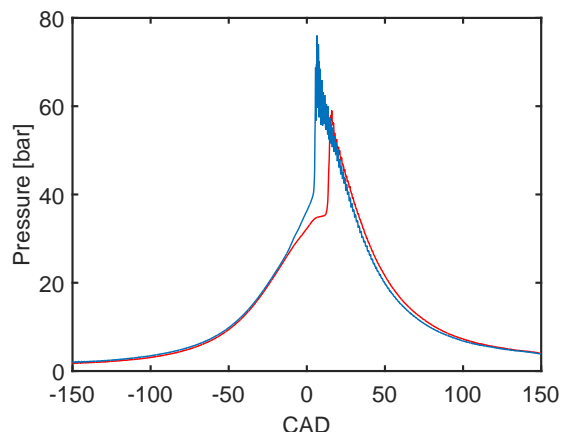
Figure 6.3: Plot of two different SACI combustion cycles from the same experimental operating point. As is often the case with SACI, the combustion exhibited large fluctuations in IMEP and peak pressure from cycle to cycle. The average IMEP was 7.4 bar and the equivalence ratio was 0.91.

under aggressive combustion conditions. The engine structure, seals, and piston rings performed well despite experiencing high pressures and a high pressure rise rate.

An additional challenge with the transition to HCCI combustion arose from the abbreviated duration of firing between breaks for the engine to motor and cool down, since the Bowditch piston lacks conventional oil cooling and lubrication. Thermal expansion effects were another practical aspect of the design to be evaluated during these tests. With a reduced shim size and a higher compression ratio, the transition to HCCI is likely to be substantially easier despite the abbreviated duration of firing.

After about 10 hours of operation, a reduction in motored pressure ratio, combined with a rattling sound upon startup of the engine, indicated that some components were no longer performing as intended. Upon investigation it was found that the aluminum window blank had become loose, moving up and down by about 1 mm within its enclosure. This required disassembly and re-evaluation of the window blank sealing strategy, discussed further in Section 6.1.2.

6.1.1   Dry Ring Combustion Performance

A notable finding upon disassembly of the engine was the state of the dry piston rings, as pictured in Figure 6.4. To evaluate the combustion performance of the rings, gradually longer periods of combustion operation at increasingly aggressive operating points was undertaken to find the limits of their performance. The cumulative effect of this extensive firing operation had caused more than half of the material of the upper piston ring to be consumed. The lower ring remained intact but visibly more worn after firing than after motoring. The deterioration of the upper ring largely explains the reduced pressure ratio observed partway through the experiments, since the volume between the two piston rings, as well as the void left behind by the consumed portions of the upper ring, added to the clearance volume of the engine and lowered the effective compression ratio. The mass lost by both rings is reported in Table 6.1.

Table 6.1: Mass of Rings After Demonstration 1

Component	Mass [g]	Percent Lost
mean unused ring weight	10.1g	—
upper used ring weight	3.2g	68%
lower used ring weight	9.2g	8.9%

A promising result of the piston rings deteriorating to the extent they did, is that their deterioration was not permanently damaging to other engine components. The engine did not seize, and no other sudden events occurred to indicate the upper ring had failed. The ring deterioration was signaled by a slightly lower pressure ratio, easily detected on the motoring pressure trace. Knowing that the failure mode for the rings in future experiments is likely to be similarly benign reduces concerns over ring lifetime or damage to the sapphire window during combustion conditions.

The process of the rings vaporizing and burning also deposited a varnish-like coating on the walls of the combustion chamber. The varnish on the cylinder head's mirrored surface can be seen in the second panel of Figure 6.5. Going forward, optical engine experiments will not include combustion sequences as long as was conducted

Figure 6.4: Left top: A comparison of lower piston ring, a new piston ring, and the top piston ring. Left bottom: Components of the Bowditch piston during engine dis-assembly following combustion with aluminum window blank. Right: The exhaust side of the Bowditch piston during dis-assembly. The upper piston ring was consumed mostly on the exhaust side.

during these tests, and thus fouling of optical surfaces with condensed ring material will be minimized. The duration of continuous firing during this demonstration was on the order of several minutes, much longer than the experiments planned once the sapphire window is installed. Strategies like skip-firing, or firing in bursts of cycles sufficient to get stabilized data (with periods of motoring to cool down in between firing cycles), will extend the lifetime of the dry piston rings and prevent varnish accumulation.

6.1.2 Aluminum Blank Sealing

The aluminum window blank had space to move up and down within its enclosure when the engine was disassembled. After studying the components to determine the root cause, it was concluded that the window enclosure had not been sufficiently pre-loaded during assembly. Interference among titanium components prevented the torque applied during assembly from compressing the window into copper seats to obtain the required fit.

6.1.3 Mirror Cleaning

The varnish deposited by the piston rings was difficult to remove from the mirrored surface, as cleaning with conventional solvents such as acetone or alcohols was not sufficient to dissolve the deposits. Silver polish, however, removed the varnish well and preserved a mirror finish that is sufficient for Schlieren imaging experiments. A comparison of mirror surfaces can be seen in Figure 6.5, where the third panel is the cleaned mirror surface.

6.1.4 Bowditch Torquing Procedure

The loose window blank required additional analysis and experimentation with respect to the structure of the Bowditch window enclosure and the type of pre-load desired. A pre-load of 100 bar on the seating surfaces was desired to seal the

Figure 6.5: Left: Polished mirror as manufactured. Center: Mirror and combustion chamber surface with dry ring residue after combustion. Right: Re-conditioned mirror.

planned 250 bar peak cylinder pressure. The entire assembly can be modeled as a set of springs, allowing the vertical pre-load imposed from torquing the titanium window enclosure together to be calculated. Each component has an effective spring constant—based on its Young's modulus, its thickness, and its cross-sectional area. The calculated torque requirement to apply 100 bar to the seating surfaces ranges between 2000 and 9000 Nm, depending on thermal expansion. Applying such a high torque pre-load requires a specialized procedure.

To grip the Bowditch components at such a high torque, a pair of hexagonal collets were designed that could clamp down on the components to exert a frictional force. The inner diameter of each collet matches the outer diameter of Bowditch components, while the hexagonal outer shape of each collet fits into conventional torque sockets and wrenches. A torque multiplier, the Proto J6232, which has a 1:18.5 torque ratio and can apply up to 3200 ft-lb (4339 Nm) was employed.

To provide a reaction force for the torque multiplier, a torquing base was designed from steel plate. The purpose of the torquing base is to grip one of the hexagonal collets while transmitting torque to the reaction arm of the torque multiplier. A drawing of the torquing setup can be seen in Figure 6.6.
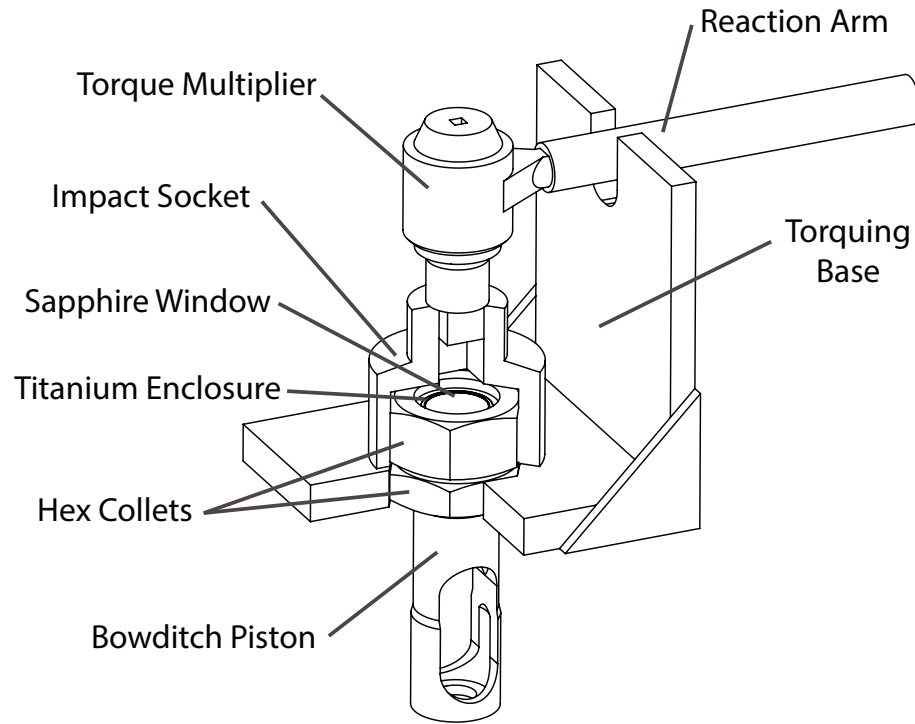
Figure 6.6: Torquing setup for window pre-load using torque multiplier. The cutaway in the impact socket and torque base show the hexagonal collets.

Using the torquing assembly, the titanium window blank was installed and pre-loaded to a torque of 2775 Nm. The torque base setup includes significant friction between the impact socket and torque base surface, so it is estimated that the actual preload on the window enclosure is between 2000 and 2775 Nm.

6.2 Demonstration 2: Titanium Window Blank I

After the cylinder head mirror surface was reconditioned and the torquing procedure tested, the engine was assembled in its high-pressure optical configuration a second time, but this time with a titanium window blank. Titanium was chosen for the window blank material of the second installation to eliminate the effects of thermal expansion contributing to seating issues around the window.

Engine tests in this configuration were focused on evaluating ring longevity under planned experimental conditions (firing in short bursts) as well as determining if window seating issues from the aluminum window blank installation were solved by the improved torquing procedure.

The 45°mirror and its mount were also installed for these tests. A photograph of the mirror within the Bowditch piston slot can be seen in Figure 6.7.
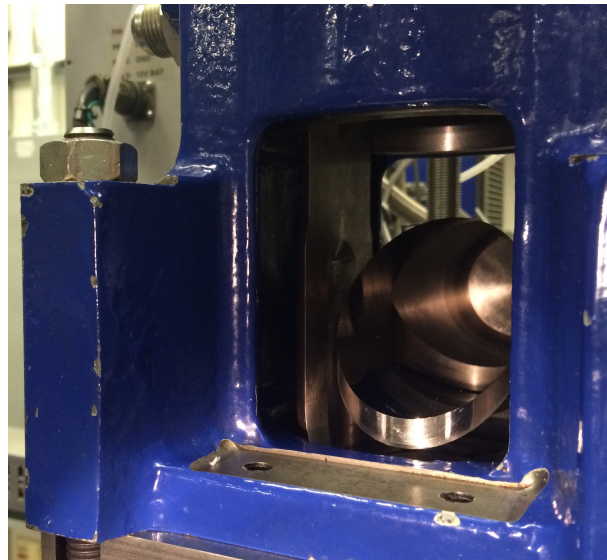
Figure 6.7: The 45°mirror mounted within the Bowditch slot during experiments with the titanium window blank.

Initial tests with the titanium window blank were successful, both for motored operation and for spark-ignited combustion of propane. The engine sealed very well, and was sounded quieter than it had with the aluminum blank. This is attributed to the modifications made in the window blank installation procedure. However, the titanium window blank tests revealed a previously undetected problem with the exhaust valves. After about 15 minutes of engine operation, both exhaust valves stopped sealing.

6.2.1 Valve Seat Distortion

Upon disassembly, it was determined that the valve seat surfaces, which were ground into the mirrored surface of the cylinder head, had become distorted and were no longer conical. The head gasket o-ring had also extruded between the head and adapter plate in two places, corresponding to the locations of narrowest wall thickness on the edge of the proud cylinder head surface, as seen in Figure 6.8. The gap along the region of smallest wall thickness between the raised mirror surface of the cylinder head and the inner diameter of the adapter plate can be seen in Figure 6.9.

Figure 6.8: Teflon head gasket o-ring extruded along edge of proud mirror surface of the cylinder head, near the exhaust valve.

The likely cause of the valve seat distortion is stress resulting from thermal expansion during the extensive firing of the aluminum window blank tests. The proud mirror surface just fits into the bore of the adapter plate at room temperature. During combustion experiments, the temperature of the cylinder head may have increased more in the exhaust valve region because of flow through the ports, causing thermal expansion in the head which was resisted near the exhaust valve seats by the surrounding structure of the adapter plate. The weakest
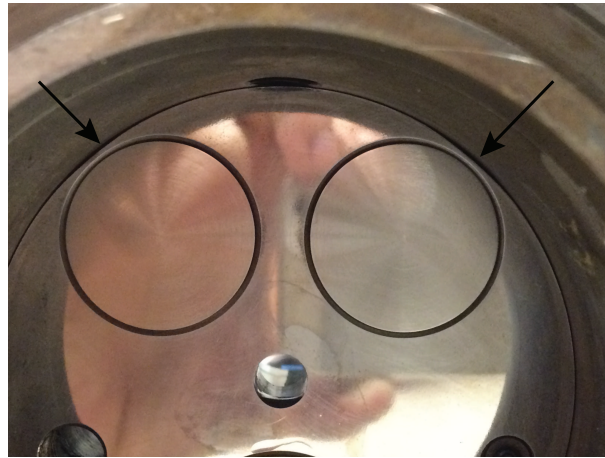
Figure 6.9: The gap between the cylinder head mirror surface and the adapter plate is largest at the point where the wall thickness between exhaust port and cylinder wall is smallest.

location in the exhaust region of the cylinder head is the location with the smallest wall thickness between the edge of the exhaust valves and the cylinder wall. It seems likely that thermal expansion caused the distorted valve seats because the similarity between the two exhaust valves is striking, and both valves stopped sealing at almost the same time.

To fix the valve seats and regain a seal around the exhaust valves, a new set of exhaust valves was lapped into the valve seats to correct the distortion. In the future, the less aggressive firing of experiments will limit thermal expansion. Modifications to the cylinder head, such as the proud mirror surface having a slightly smaller diameter than its current one, could allow for more clearance between adapter plate bore and cylinder head to prevent yielding from thermal expansion.

6.3   Demonstration 3: Titanium Window Blank II

Once the exhaust valve seats were re-lapped, the engine was assembled to continue evaluating the changes made after the aluminum blank tests. Motoring and SI firing

data were taken, with the engine at 1200 rpm and at a slightly lean equivalence ratio. Valve timing was adjusted for improved volumetric efficiency compared to earlier experimental demonstrations. A pressure-volume plot as well as a log(P)-log(V) plot showing both motoring and firing cycles from this configuration can be seen in Figure 6.10
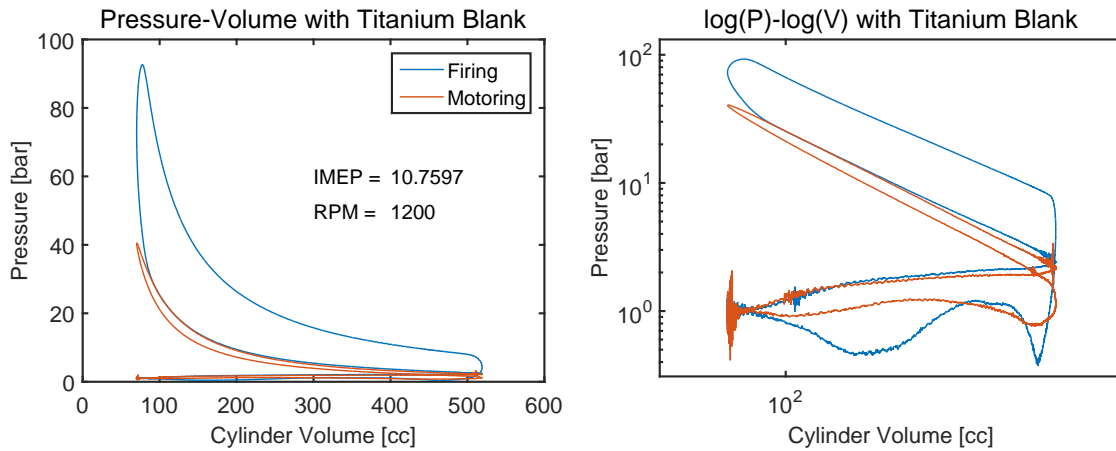
Figure 6.10: Motored and fired pressure traces from the optical engine with titanium window blank installed. The engine speed is 1200 rpm, the intake pressure is boosted to 2.05 bar, and the SI combustion is of propane at around .85 equivalence ratio.

The firing was done in bursts of around 150 cycles, with a minute or more of motored operation between firing bursts. The coolant temperature was regulated to 50°C. After gathering data and disassembling the engine, the piston rings were examined and weighed. The rings looked intact besides a few small eroded spots along the top edge of the upper ring. The mass lost from the rings was small, as seen in Table 6.2. This confirms that firing for short periods of time allows the rings to remain intact. Based on the success of engine operation with the titanium window blank, it was concluded that the sapphire window could be installed to enable optical access.

Table 6.2: Mass of Rings After Demonstration 3

Component	Mass [g]	Percent Lost
mean unused ring weight	10.1	—
upper used ring weight	9.7	4.0%
lower used ring weight	9.6	5.0%
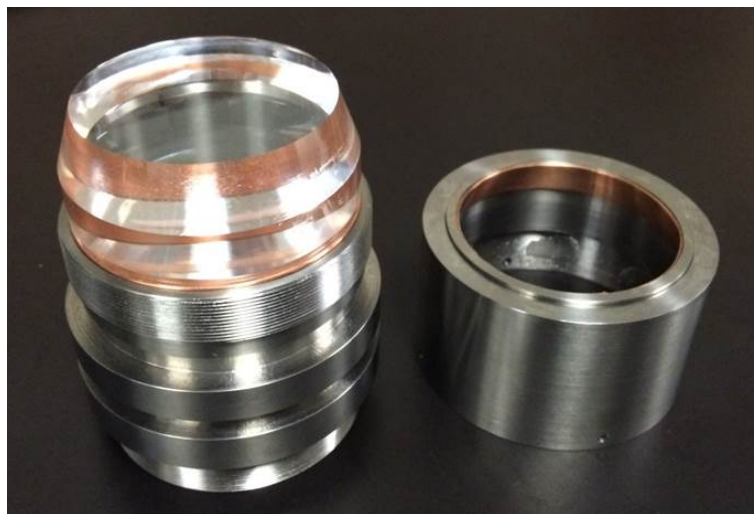
Figure 6.11: Photograph of sapphire window resting on its copper seat in Bowditch enclosure.

6.4   Demonstration 4: Sapphire Window

Finally, to demonstrate high-pressure imaging capability in the engine, the sapphire window was installed. It was preloaded in the Bowditch piston enclosure using the same torquing procedure used on the titanium window blank. Photographs of the sapphire window resting in the titanium enclosure, as well as a view of the combustion chamber off of the 45°mirror and through the sapphire window, can be seen in Figure 6.11 and Figure 6.12.

The engine assembled with the sapphire window was tested under both naturally-aspirated and boosted, spark-ignited conditions. High-speed video was captured using a Phantom V7.3 camera, made by Vision Research. Pressure-volume and

Figure 6.12: View of combustion chamber through sapphire window, reflected off of the 45°mirror.

log(P)-log(V) plots from a representative naturally-aspirated and boosted operating points can be seen in Figure 6.14 and Figure 6.16, respectively. A series of in-cylinder images from both load points corresponding to the plotted pressure data can be seen in Figure 6.13 and Figure 6.15, while engine operation parameters for both sets of data presented are listed in Table 6.3.

In each panel of images, the flame front progresses outward from the spark location (upper right) to consume the air/fuel mixture. The premixed nature of port-fuel-injected combustion results in mostly blue light. Small amounts of grease and lubricant present in the combustion chamber, as well as small fragments of dry ring material are most likely responsible for the bright sparks and greenish tinges, respectively. The copper content in both the ring material and the high-temperature anti-seize used during assembly of the sapphire enclosure produce green flames during the beginning of the expansion stroke, when gases emerge from the crevice volume surrounding the Bowditch piston.
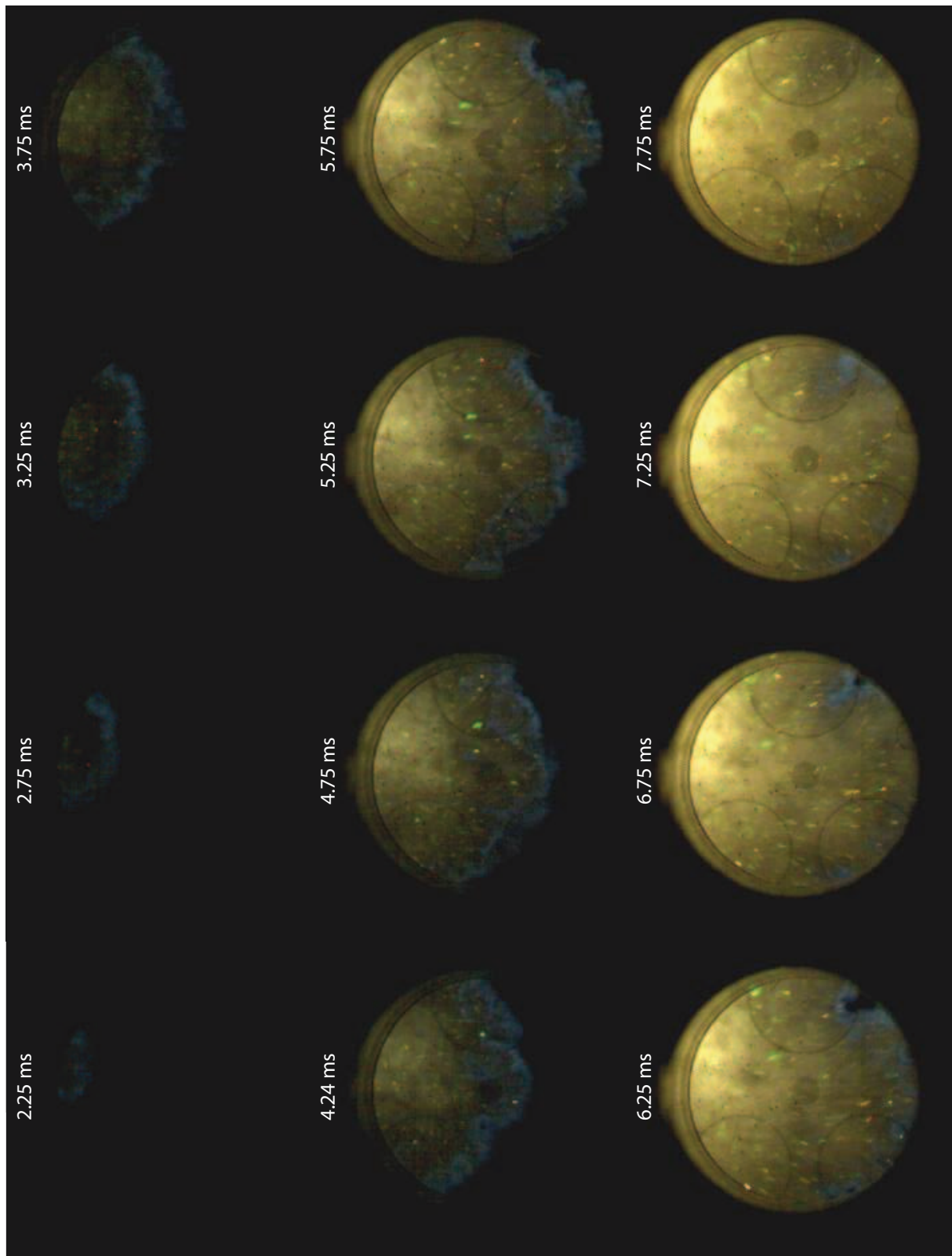
Figure 6.13: Images of naturally-aspirated spark-ignited combustion of propane. Times listed above each panel indicate the time after the spark.
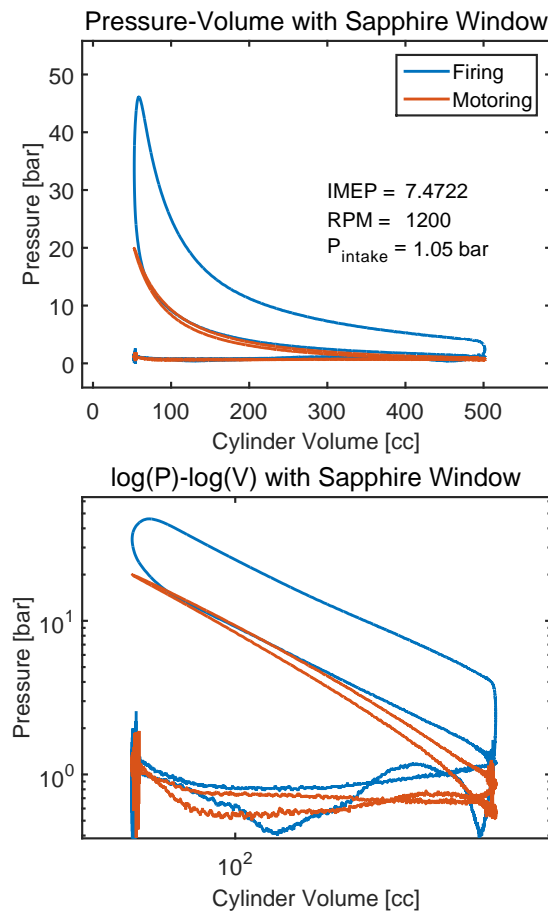
Figure 6.14: PV and log(P)-log(V) plots of spark-ignited propane combustion with intake pressure of 1.05 bar.
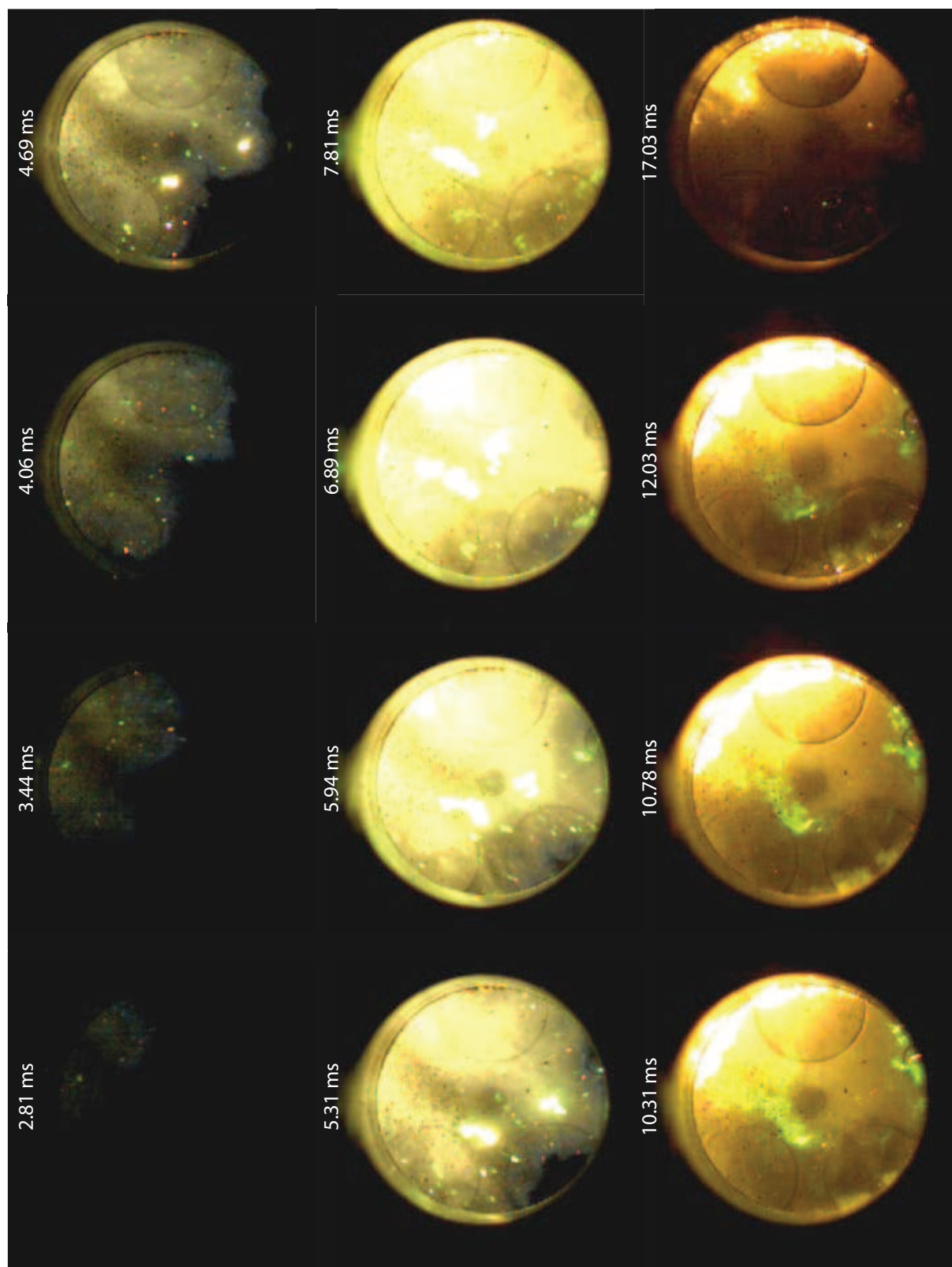
Figure 6.15: Images of boosted spark-ignited combustion of propane. Times listed above each panel indicate the time after the spark.
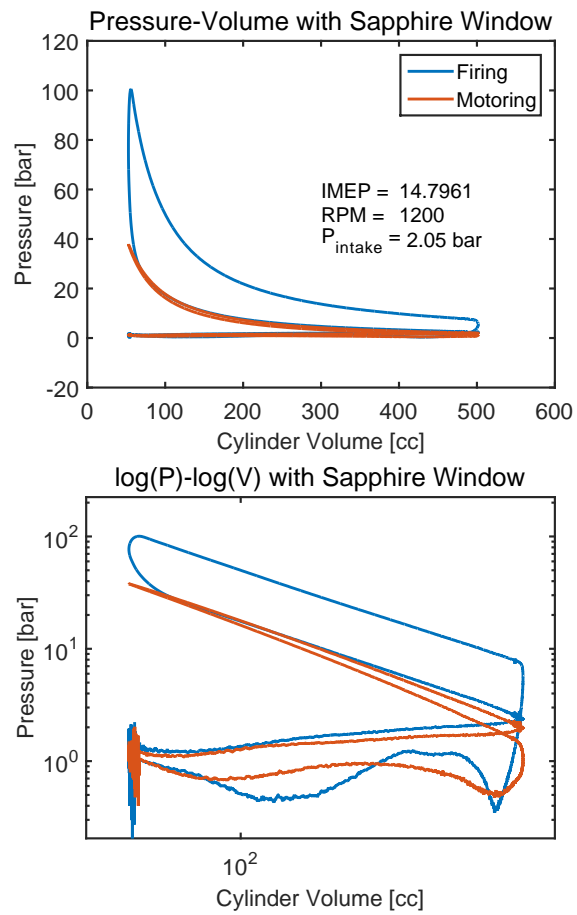
Figure 6.16: PV and log(P)-log(V) plots of spark-ignited propane combustion with intake pressure of 2.05 bar.

Table 6.3: Optical Engine Experimental Parameters:

Parameter	(Naturally Aspirated)	(Boosted)
bore	82 mm	82 mm
stroke	85 mm	85 mm
engine speed	1200 rpm	1200 rpm
intake pressure	1.05 bar	2.05 bar
IMEP	7.47 bar	14.80 bar
fuel	propane	propane
ignition	SI	SI
exposure time	240 μs	150 μs
frame rate	4000 fps	6400 fps

6.5　Discussion of Optical Results

To conclude the discussion of the optical access engine demonstration, the original goals of the experimental design are revisited. Table 6.4 contains abbreviated summaries of the goals set forth in Section 5.1, along with brief comments on the experimental outcome of each goal.

Table 6.4: Summary of Optical Engine Goals and Experimental Capability

High-pressure capability of 250 bar	All components designed for 250 bar with a safety factor of at least 2. Maximum pressure in initial tests exceeded 100 bar.
Image as much of combustion chamber as possible	A 58 mm diameter circular area is visible in the center of the 82 mm cylinder bore.
Behavior similar to a conventional engine	Realistic exhaust valve area, careful consideration of crevice volume, well-sealing piston rings, etc., contribute to conventional engine-like behavior. Comparison to engine models and isentropic peak pressure confirm the behavior.
"Pass-through" imaging capability	Flat, mirrored cylinder head surface and sapphire window in Bowditch piston allow for Schlieren, etc., in the engine. The mirrored surface was manufactured successfully on the head/valve assembly.
Variable valve timing	The EHVS system enables variable valve timing in the optical engine.
Independent cylinder head cooling	The cooling passages for cylinder head and adapter plate are independent of each-other and the rest of the engine.
High engine speed capability	The optical engine was motored up to 3000 rpm during initial testing, as limited by the EHVS.
Measure typical quantities of interest for engine experiments	There is no notable loss of experimental measurement capability in the optical access engine compared to the single-cylinder research engine in non-optical configuration.
Multiple pressure transducers	The combustion chamber has ports for three pressure transducers, one in the cylinder head and two in the adapter plate.
Useful for future research	The cylinder head accommodates several models of Diesel and gasoline direct-injection injectors, making future experimental investigation possible including diesel injection of oxygenated fuels, natural gas, etc.

Chapter 7

Conclusions and Future Work

This chapter synthesizes conclusions from the previous chapters and provides insight for the continuation of the work presented in this thesis.

7.1 Conclusions Concerning Ringing in HCCI Combustion

Ringing in HCCI engines arises from a gasdynamically-impeded combustion event producing a coupled pressure wave and reaction front. These coupled pressure waves, or developing detonations, can produce pressures well in excess of the constant-volume pressure that would otherwise be seen in the absence of coupling. The coupling behavior can be affected by the temperature gradient at the origin of autoignition. Steep temperature gradients produce deflagrations, while shallow gradients produce homogeneous explosions. Medium temperature gradients can result in gasdynamic coupling and produce a developing detonation. The range of temperature gradients that produce a developing detonation broadens with increasing mixture strength and an increasingly rapid conversion from chemical bond energy to sensible energy during autoignition.

Based on previous experimental data, the gasdynamic coupling can be disrupted

in combustion of a stoichiometric methane/air mixture by using water injection. Insight into the gasdynamic coupling and its disruption in this experiment requires experimental or modeling capability beyond the pressure-time data captured by in-cylinder pressure transducers.

7.2   Modeling Conclusions

Using a 1D reacting compressible flow model, the developing detonation and thermal explosion modes were demonstrated. From the numerical model, factors contributing to the gasdynamic coupling were examined, including the effects of dilution, and inhomogeneity of both temperature and chemical species. Among inert moderators, gases having a high specific heat such as nitrogen serve to prevent or delay gasdynamic coupling more than a gases having a low specific heat such as argon. Dilution with excess air is less effective at disrupting coupling than dilution with inert moderators, including argon. The gasdynamic coupling behavior observed in the model results included more complex behavior than was expected based on initial temperature gradient alone: Some mixtures exhibited a delayed coupling effect, while other mixtures that did not initially couple formed developing detonations when pressure waves reflected off walls.

The numerical model also predicts that much more water is required to disrupt coupling than previous experiments have suggested. This result, combined with the more complicated delayed coupling effect, provided the motivation for experimental investigation of developing detonations in an IC engine environment. Using insight gained from the model regarding the effects of moderators and temperature gradients, experiments can be targeted, and experimental results interpreted, to gain an enhanced understanding of these events beyond what could be gained using a model or experiment alone.

7.3 Future Modeling Work

The numerical model can be used to evaluate additional factors in gasdynamic coupling beyond those presented in this thesis. Dilution with other moderators such as exhaust gas, or a tri-atomic moderator such as CO_2, could provide further insight into the role of diluents on coupling. Inhomogeneities in temperature that are closer in size to the integral length scale, rather than the macroscopic ones explored in this work, might shed additional insight into the progress of developing detonations in engine environments. Further, a more thorough evaluation of certain chemical effects, such as the role of NO_x, could be done by suppressing the formation of certain chemical species in the model.

Calculating and plotting other relevant quantities that vary in space with temperature and species inhomogeneity, such as ignition delay time, could provide additional insight. For example, a linear gradient in ignition delay time rather than in temperature, or a sweep of induction times from low-to-high by artificially suppressing or enhancing kinetic rates, could provide further insight beyond the model cases computed thus far.

Since the model is intended as a compliment to experimentation, extension to two or three dimensions may not necessarily be beneficial, unless images from experimental investigation reveal that two or three dimensions are required to capture an aspect of the coupling that was not previously captured.

7.4 Experimental Conclusions

An optical access engine was constructed that is capable of capturing high-speed video of combustion phenomena at pressures up to 250 bar. Several components were designed to make this experimental capability possible: a cylinder head with a mirror-polished surface to enable Schlieren imaging, a robust Bowditch piston with a sapphire window, and an adapter plate containing two in-cylinder pressure transducers. Additional modifications to the existing AVL single-cylinder engine

included the addition of a bracing structure to load cast iron components in compression, a modified variable-valve actuation system, larger balance weights, and a stronger connecting rod and wrist pin.

The engine experiment was tested, and its capability demonstrated, under both motoring and boosted SI combustion conditions. Performance of dry piston rings and the sealing procedure for the sapphire window were evaluated in tests using metal window blanks prior to installing a sapphire window. The engine experiment demonstrated excellent capability to produce realistic IC engine behavior with few limitations despite requirements such as a flat cylinder head and an oil-free combustion chamber. A revised assembly procedure was designed for the Bowditch piston, to apply torque of over 2000 Nm to pre-load the copper window seals. By firing in short bursts of 100-150 cycles, thermal expansion and ring damage effects, which manifested in initial experiments, were mitigated. High-speed video was captured of propane SI combustion, up to pressures of around 100 bar, exceeding the typical pressure limit of optical access engines.

7.5   Future Experimentation

Schlieren imaging was not implemented in the work described in this thesis due to the lack of a laser light source. Thus, it is left to future experimenters to carry out studies of ringing and high-load HCCI with the aid of Schlieren imaging in the optical engine. A number of experiments can be undertaken using the optical engine based on modeling results, such as dilution with excess air, dilution with nitrogen, and centralized injection of a moderator such as water or CO_2.

The optical access engine will enable numerous future studies of high-pressure combustion events such as SI engine knock, full-load Diesel combustion, high-pressure gas injections of natural gas or syn-gas, and further studies of ringing and high-load premixed combustion. In other words, most engine research experiment requiring optical access can be performed in this experiment.

Bibliography

[1] IEA. *World Energy Outlook 2014.* http://dx.doi.org/10.1787/weo-2014-en.

[2] UNAIDS. *AIDS Information.* http://www.aidsinfo.unaids.org, 2015.

[3] EPA. *Inventory of US Greenhouse Gas Emissions and Sinks: 1990-2013.* EPA 430-R-15-004, 2015.

[4] OECD. Publishing and International Energy Agency. *Energy Technology Perspectives 2015.* Organisation for Economic Co-operation and Development, 2012.

[5] Matt N Svrcek and Chris F Edwards. Homogeneous charge compression ignition with nondilute stoichiometric methane–air at extreme compression ratios. *International Journal of Engine Research*, 2013.

[6] John B Heywood. *Internal combustion engine fundamentals*, volume 930. Mcgraw-hill New York, 1988.

[7] Richard Stone. *Introduction to internal combustion engines.* Palgrave Macmillan, 2012.

[8] Ronald A. Reese II. *High Efficiency IC Engines With an Emphasis on SI Engines.* Presentation at 2009 SAE Powertrains, Fuels and Lubricants Meeting, 2009.

[9] Bernard Johnson and Chris Edwards. Exploring the pathway to high efficiency ic engines through exergy analysis of heat transfer reduction. *SAE International Journal of Engines*, 6(2013-01-0278):150–166, 2013.

[10] Samveg Saxena and Iván D Bedoya. Fundamental phenomena affecting low temperature combustion and hcci engines, high load limits and strategies for extending these limits. *Progress in Energy and Combustion Science*, 39(5):457–488, 2013.

[11] Yi Yang, John E Dec, Nicolas Dronniou, and Magnus Sjöberg. Tailoring hcci heat-release rates with partial fuel stratification: Comparison of two-stage and single-stage-ignition fuels. *Proceedings of the Combustion Institute*, 33(2):3047–3055, 2011.

[12] Magnus Christensen and Bengt Johansson. Influence of mixture quality on homogeneous charge compression ignition. *SAE Transactions, Journal of Fuels and Lubricants*, 107, 1998.

[13] Xiaojian Yang and Guoming Zhu. Si and hcci combustion mode transition control of an hcci capable si engine. *Control Systems Technology, IEEE Transactions on*, 21(5):1558–1569, 2013.

[14] Nissan Racing. *Image of knock-damaged piston.* $http : //www.nissanroadracing.com/showthread.php?t = 1243\&page = 2$. Accessed: 2015-10-19.

[15] John Fitton and Roy Nates. Knock erosion in spark-ignition engines. 1996.

[16] Thomas E Reinhart. Diesel combustion mode switching-a substantial nvh challenge. Technical report, SAE Technical Paper, 2009.

[17] Morgan M Andreae, Wai K Cheng, Thomas Kenney, and Jialin Yang. On hcci engine knock. Technical report, SAE Technical Paper, 2007.

[18] Zhijun Peng, Hua Zhao, Tom Ma, and Nicos Ladommatos. Characteristics of homogeneous charge compression ignition (hcci) combustion and emissions of n-heptane. *Combustion science and technology*, 177(11):2113–2150, 2005.

[19] P Brijesh, A Chowdhury, and S Sreedhara. Effect of ultra-cooled egr and retarded injection timing on low temperature combustion in ci engines. Technical report, SAE Technical Paper, 2013.

[20] Nicolas Dronniou and John E Dec. Investigating the development of thermal stratification from the near-wall regions to the bulk-gas in an hcci engine with planar imaging thermometry. Technical report, SAE Technical Paper, 2012.

[21] Jerald A Caton. Exergy destruction during the combustion process as functions of operating and design parameters for a spark-ignition engine. *International Journal of Energy Research*, 36(3):368–384, 2012.

[22] Xudong Zhen, Yang Wang, Shuaiqing Xu, Yongsheng Zhu, Chengjun Tao, Tao Xu, and Mingzhi Song. The engine knock analysis–an overview. *Applied Energy*, 92:628–636, 2012.

[23] C Dahnz and U Spicher. Irregular combustion in supercharged spark ignition engines–pre-ignition and other phenomena. *International Journal of Engine Research*, 11(6):485–498, 2010.

[24] Norbert Peters, Bruno Kerschgens, and Gnther Paczko. Super-knock prediction using a refined theory of turbulence. *SAE Int. J. Engines*, 6:953–967, 04 2013.

[25] Gautam T Kalghatgi and Derek Bradley. Pre-ignition and super-knockin turbo-charged spark-ignition engines. *International Journal of Engine Research*, 13(4):399–414, 2012.

[26] David A Rothamer, Jordan A Snyder, Ronald K Hanson, Richard R Steeper, and Russell P Fitzgerald. Simultaneous imaging of exhaust gas residuals and

temperature during hcci combustion. *Proceedings of the Combustion Institute*, 32(2):2869–2876, 2009.

[27] C. G. W. Sheppard, S. Tolegano, and R. Woolley. On the nature of autoignition leading to knock in hcci engines. *Society of Automotive Engineers*, 2002.

[28] Ya B Zel'Dovich, VB Librovich, GM Makhviladze, and GI Sivashinskil. On the onset of detonation in a nonuniformly heated gas. *Journal of Applied Mechanics and Technical Physics*, 11(2):264–270, 1970.

[29] Ya B Zeldovich. Regime classification of an exothermic reaction with nonuniform initial conditions. *Combustion and Flame*, 39(2):211–214, 1980.

[30] PA Urtiew and AK Oppenheim. Experimental observations of the transition to detonation in an explosive gas. In *Proceedings of the Royal Society of London A: Mathematical, Physical and Engineering Sciences*, volume 295, pages 13–28. The Royal Society, 1966.

[31] John HS Lee. Initiation of gaseous detonation. *Annual Review of Physical Chemistry*, 28(1):75–104, 1977.

[32] V.B. Librovich, G.M. Makhviladze, G.I. Sivashinskii, and I.A.B. Zeldovich. On the development of detonation in a non- uniformly preheated gas(gas dynamic conditions resulting in reacting gases detonation waves at high initial temperatures, simulating internal combustion engine knock). *Astronautica Acta*, 15:313–321, 1969.

[33] Ya B Zeldovich. Theory of combustion and detonation of gases [in russian], akad. *Nauk of the USSR, Moscow–Leningrad*, 1944.

[34] Chris Morley, Derek Bradley, and XJ Gu. Amplified pressure waves during autoignition: Relevance to cai engines. 2002.

[35] Magnus Sjberg and John E. Dec. Smoothing hcci heat-release rates using partial fuel stratification with two-stage ignition fuels. In *SAE Technical Paper*. SAE International, 04 2006.

[36] Yi Yang, John E. Dec, Nicolas Dronniou, and Magnus Sjberg. Tailoring {HCCI} heat-release rates with partial fuel stratification: Comparison of two-stage and single-stage-ignition fuels. *Proceedings of the Combustion Institute*, 33(2):3047 − 3055, 2011.

[37] John E. Dec and Magnus Sjberg. Isolating the effects of fuel chemistry on combustion phasing in an hcci engine and the potential of fuel stratification for ignition control. In *SAE Technical Paper*. SAE International, 03 2004.

[38] Daniel Dahl, Mats Andersson, Andreas Berntsson, Ingemar Denbratt, and Lucien Koopmans. Reducing pressure fluctuations at high loads by means of charge stratification in hcci combustion with negative valve overlap. In *SAE Technical Paper*. SAE International, 06 2009.

[39] Daniel Dahl, Mats Andersson, and Ingemar Denbratt. The role of charge stratification for reducing ringing in gasoline engine homogeneous charge compression ignition combustion investigated by optical imaging. *International Journal of Engine Research*, 2013.

[40] Andreas Vressner, Andreas Lundin, Magnus Christensen, Per Tunestål, and Bengt Johansson. Pressure oscillations during rapid hcci combustion. Technical report, SAE Technical Paper, 2003.

[41] Andrew E Lutz, Robert J Kee, James A Miller, Harray A Dwyer, and Antoni K Oppenheim. Dynamic effects of autoignition centers for hydrogen and c 1, 2-hydrocarbon fuels. In *Symposium (International) on Combustion*, volume 22, pages 1683–1693. Elsevier, 1989.

[42] G König, RR Maly, D Bradley, AKC Lau, and CGW Sheppard. Role of exothermic centres on knock initiation and knock damage. Technical report, SAE Technical Paper, 1990.

[43] MA Liberman, AD Kiverin, and MF Ivanov. On detonation initiation by a temperature gradient for a detailed chemical reaction models. *Physics Letters A*, 375(17):1803–1808, 2011.

[44] Ming Jia, Maozhao Xie, and Zhijun Peng. Prediction of the operating range for a hcci engine based on a multi-zone model. Technical report, SAE Technical Paper, 2008.

[45] Salvador M Aceves, Daniel L Flowers, Charles K Westbrook, J Ray Smith, William Pitz, Robert Dibble, Magnus Christensen, and Bengt Johansson. A multi-zone model for prediction of hcci combustion and emissions. Technical report, SAE Technical paper, 2000.

[46] Scott B Fiveland and Dennis N Assanis. Development of a two-zone hcci combustion model accounting for boundary layer effects. Technical report, SAE Technical paper, 2001.

[47] Eleuterio F Toro. *Riemann solvers and numerical methods for fluid dynamics: a practical introduction*. Springer Science & Business Media, 2009.

[48] Malcolm W Chase. Janaf thermochemical tables. *JANAF thermochemical tables, by Chase, MW Washington, DC: American Chemical Society; New York: American Institute of Physics for the National Bureau of Standards, c1986.. United States. National Bureau of Standards.*, 1, 1986.

[49] Dave Goodwin, Nicholas Malaya, Harry Moffat, and Raymond Speth. Cantera: An object-oriented software toolkit for chemical kinetics, thermodynamics, and transport processes. *Caltech, Pasadena, CA*, 2009.

[50] Ronald P Fedkiw. *A survey of chemically reacting, compressible ows.* PhD thesis, University of California Los Angeles, 1997.

[51] Gregory P Smith, David M Golden, Michael Frenklach, Nigel W Moriarty, Boris Eiteneer, Mikhail Goldenberg, C Thomas Bowman, Ronald K Hanson, Soonho Song, William C Gardiner Jr, et al. Gri-mech 3.0. Technical report, 1999.

[52] Scott D Cohen and Alan C Hindmarsh. Cvode, a stiff/nonstiff ode solver in c. *Computers in physics*, 10(2):138–143, 1996.

[53] Gary A Sod. A survey of several finite difference methods for systems of nonlinear hyperbolic conservation laws. *Journal of Computational Physics*, 27(1):1 – 31, 1978.

[54] Daniel Dahl, Mats Andersson, and Ingemar Denbratt. The origin of pressure waves in high load hcci combustion: A high-speed video analysis. *Combustion Science and Technology*, 183(11):1266–1281, 2011.

[55] Akira Iijima, Mitsuaki Tanabe, Koji Yoshida, Hideo Shoji, Naoya Itoh, Akira Terashima, and Tomoya Tojo. Visualization and spectroscopic measurement of knocking combustion accompanied by cylinder pressure oscillations in an hcci engine. Technical report, SAE Technical Paper, 2013.

[56] U Spicher, H Kröger, and J Ganser. Detection of knocking combustion using simultaneously high-speed schlieren cinematography and multi optical fiber technique. Technical report, SAE Technical Paper, 1991.

[57] CF Edwards, Dennis L Siebers, and Dennis H Hoskin. A study of the autoignition process of a diesel spray via high speed visualization. Technical report, SAE Technical Paper, 1992.

[58] Lyle M Pickett, Sanghoon Kook, and Timothy C Williams. Visualization of diesel spray penetration, cool-flame, ignition, high-temperature combustion, and

soot formation using high-speed imaging. *SAE International Journal of Engines*, 2(2009-01-0658):439–459, 2009.

[59] David P. Sczomak, Allan Zhao, Michael Simon, and Yangbing Zeng. High speed endoscope imaging to supplement cfd analysis and combustion testing for sidi engine startup development. In *SAE Technical Paper*. SAE International, 04 2010.

[60] Marco Bakenhus and Rolf D Reitz. Two-color combustion visualization of single and split injections in a single-cylinder heavy-duty di diesel engine using an endoscope-based imaging system. Technical report, SAE Technical Paper, 1999.

[61] Ulrich Spicher, Gunter Schmitz, and Hans-Peter Kollmeier. Application of a new optical fiber technique for flame propagation diagnostics in ic engines. Technical report, SAE Technical Paper, 1988.

[62] Akira Iijima, Naoya Ito, Takashi Shimada, Masanori Yamada, and Hideo Shoji. A study of hcci knocking accompanied by pressure oscillations based on visualization of the entire bore area. *SAE International Journal of Engines*, 7(2014-01-2664):1863–1874, 2014.

[63] Fred W. Bowditch. A new tool for combustion research a quartz piston engine. In *SAE Technical Paper*. SAE International, 01 1961.

[64] Gary S Settles. *Schlieren and shadowgraph techniques: visualizing phenomena in transparent media*. Springer Science & Business Media, 2012.

[65] Matt N Svrcek, SL Miller, and Christopher F Edwards. Diesel spray behavior at compression ratios up to 100: 1. *Atomization and Sprays*, 20(5), 2010.

[66] Matthew N Svrcek and Christopher F Edwards. Emissions from an extreme-compression, free-piston engine with diesel-style combustion. *International Journal of Engine Research*, 13(3):238–252, 2012.

[67] Joseph R Davis et al. *ASM specialty handbook: cast irons.* ASM international, 1996.

[68] Engineering Toolbox. *Coefficients of Thermal Expansion.* $http$: $//www.engineeringtoolbox.com/linear-expansion-coefficients-d_95.html$, 2015.

[69] Valley Design Corporation. *Coefficients of Thermal Expansion.* $http$: $//www.valleydesign.com/sappprop.htm$, 2015.